

# **FABRICATION OF YTTRIA-STABILISED-ZIRCONIA COATINGS USING ELECTROPHORETIC DEPOSITION**

**A thesis submitted to the University of Manchester for the degree of PhD in the  
Faculty of Engineering and Physical Sciences**

**2008**

**CHANGZHENG JI  
SCHOOL OF MATERIALS**

ProQuest Number: 13805309

All rights reserved

INFORMATION TO ALL USERS

The quality of this reproduction is dependent upon the quality of the copy submitted.

In the unlikely event that the author did not send a complete manuscript and there are missing pages, these will be noted. Also, if material had to be removed, a note will indicate the deletion.



ProQuest 13805309

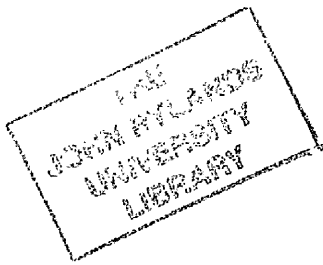
Published by ProQuest LLC (2018). Copyright of the Dissertation is held by the Author.

All rights reserved.

This work is protected against unauthorized copying under Title 17, United States Code  
Microform Edition © ProQuest LLC.

ProQuest LLC.  
789 East Eisenhower Parkway  
P.O. Box 1346  
Ann Arbor, MI 48106 – 1346

EUDGO



~~Th31624~~

✓

## List of Contents

<b>List of Contents .....</b>	<b>2</b>
<b>Figure List.....</b>	<b>6</b>
<b>Table List.....</b>	<b>12</b>
<b>Abstract .....</b>	<b>13</b>
<b>Declaration.....</b>	<b>15</b>
<b>Copyright Statement.....</b>	<b>16</b>
<b>Publication List .....</b>	<b>17</b>
<b>Acknowledgements .....</b>	<b>18</b>
<b>Chapter 1 Introduction .....</b>	<b>19</b>
§1.1 Introductory remarks .....	19
§1.2 Aim of this project.....	22
§1.3 Thesis outline.....	22
<b>Chapter 2 Literature Review .....</b>	<b>24</b>
§2.1 Colloidal processing of ceramics .....	24
§2.1.1 Interparticle energies .....	25
§2.1.1.1 VdW attractive energy .....	25
§2.1.1.2 Electrostatic interaction energy .....	27
§2.1.1.3 Steric repulsion energy.....	30
§2.1.1.4 Structural energy .....	31
§2.1.1.5 DLVO theory .....	31
§2.1.2 Suspension rheology .....	33
§2.1.3 Colloidal consolidation.....	35
§2.1.4 Drying process .....	36
§2.1.4.1 Drying stages.....	36
§2.1.4.2 Constrained drying and crack formation .....	38
§2.2 Principle of electrophoretic deposition .....	40
§2.2.1 Electrophoretic mobility.....	41



## List of Contents

---

§2.2.2 EPD kinetics.....	42
§2.2.3 Deposit formation mechanisms.....	47
§2.2.4 Aggregation of deposited particles during EPD.....	49
§2.2.5 Remarks on EPD of advanced materials .....	50
<b>§2.3 Sintering of colloidal ceramic coatings .....</b>	<b>51</b>
§2.3.1 Mechanisms of sintering .....	51
§2.3.2 Sintering stages .....	54
§2.3.3 Sintering kinetics .....	55
§2.3.3.1 Sintering shrinkage.....	55
§2.3.3.2 Effect of particle packing on sintering kinetics.....	55
§2.3.4 Constrained sintering of ceramic coatings .....	57
<b>§2.4 Summary.....</b>	<b>60</b>
<b>Chapter 3 Experimental Procedure and Characterisation Methods.....</b>	<b>62</b>
<b>§3.1 Preparation of suspensions .....</b>	<b>62</b>
§3.1.1 Raw materials and preparation procedure.....	62
§3.1.2 Centrifuge treatment.....	62
§3.1.3 Attrition milling treatment.....	63
<b>§3.2 Characterisation of particles and suspensions.....</b>	<b>63</b>
§3.2.1 Particle size, shape and surface morphology determination .....	63
§3.2.2 Agglomerate sizes determination.....	63
§3.2.3 Zeta potential measurement .....	64
§3.2.4 Other characterisations .....	64
<b>§3.3 Fabrication of EPD green coatings.....</b>	<b>64</b>
<b>§3.4 Characterisation of EPD deposits.....</b>	<b>66</b>
§3.4.1 Characterisation of wet coatings.....	66
§3.4.2 Characterisation of green coatings.....	67
<b>§3.5 Sintering of EPD deposits .....</b>	<b>67</b>
<b>§3.6 Characterisation of sintered EPD deposits.....</b>	<b>68</b>
§3.6.1 Measurement of densities of sintered deposits .....	68
§3.6.2 Characterisation of microstructures.....	69
§3.6.3 Mechanical hardness.....	69

<b>Chapter 4 Particle Packing Mechanism during EPD .....</b>	<b>70</b>
<b>§4.1 Introduction.....</b>	<b>70</b>
<b>§4.2 Results .....</b>	<b>71</b>
§4.2.1 Characterisation on suspensions .....	71
§4.2.2 Deposition kinetics .....	74
§4.2.3 Wet packing density.....	76
§4.2.4 Electric field densification .....	78
<b>§4.3 Discussion .....</b>	<b>80</b>
§4.3.1 Suspension properties.....	80
§4.3.2 Deposition kinetics .....	81
§4.3.3 Particle packing during EPD.....	83
<b>§4.4 Summary.....</b>	<b>86</b>
<b>Chapter 5 Microstructural Development in EPD Coatings .....</b>	<b>87</b>
<b>§5.1 Introduction.....</b>	<b>87</b>
<b>§5.2 Results .....</b>	<b>88</b>
§5.2.1 Characterisation of suspensions.....	88
§5.2.1.1 Agglomerate size distributions of particles .....	88
§5.2.1.2 Particle shape and surface morphology .....	92
§5.2.1.3 Zeta potential and electrical conductivity of suspension.....	95
§5.2.1.4 Centrifuge separation of particles .....	96
§5.2.2 EPD of particles with different sizes .....	100
§5.2.2.1 Formation of EPD coatings .....	100
§5.2.2.2 Microstructure .....	102
§5.2.2.3 Microhardness of free sintered EPD deposit.....	104
§5.2.3 EPD of centrifuge separated particles .....	107
§5.2.4 EPD of mixtures of different sized particles .....	109
<b>§5.3 Discussion .....</b>	<b>114</b>
§5.3.1 Ionic depletion during the electric field densification.....	114
§5.3.2 Particle packing during EPD.....	117
§5.3.3 Microstructure of free sintered EPD deposit.....	119
<b>§5.4 Summary.....</b>	<b>121</b>

---

<b>Chapter 6 Sintering of EPD Coatings on Metallic Substrates.....</b>	<b>123</b>
<b>§6.1 Introduction.....</b>	<b>123</b>
<b>§6.2 Results .....</b>	<b>124</b>
§6.2.1 Effects of sintering temperature.....	124
§6.2.1.1 Free sintering shrinkage.....	124
§6.2.1.2 Sintered coating density.....	127
§6.2.1.3 Microhardness .....	129
§6.2.1.4 Microstructures.....	131
§6.2.2 Effects of particle size .....	133
§6.2.2.1 Coating density.....	134
§6.2.2.2 Microstructures.....	135
§6.2.2.3 Microhardness .....	138
§6.2.3 Effects of the electric field densification.....	140
§6.2.3.1 Microstructures.....	140
§6.2.3.2 Microhardness .....	144
§6.2.4 Effects of coating thickness.....	146
§6.2.4.1 Microstructures.....	146
§6.2.4.2 Microhardness .....	147
<b>§6.3 Discussion .....</b>	<b>149</b>
§6.3.1 Sintering mechanisms determination and sintering kinetics.....	149
§6.3.2 Microhardness.....	152
§6.3.3 Electric field densification .....	154
<b>§6.4 Summary.....</b>	<b>155</b>
<b>Chapter 7 Conclusions .....</b>	<b>156</b>
<b>Chapter 8 Suggestions for Future Work .....</b>	<b>158</b>
<b>References: .....</b>	<b>160</b>

## Figure List

### Chapter 2:

**Figure 2.1** Schematic illustration of the interaction potential energy and relevant length scales for (a) electrostatic, (b) steric, and (c) structural contributions, where  $\kappa^{-1}$  is the effective double-layer thickness,  $\delta$  the adsorbed layer thickness, and  $\sigma$  the characteristic size of species resulting in ordering within the interparticle gap.

**Figure 2.2** Schematic of the electrical double layer model for particle charging in a polar liquid and Gouy-Chapman profile of the electrical potential.

**Figure 2.3** Potential energy of interaction between two particles with electrical double layers (the secondary minimum is not expected when  $\kappa a < 1$ ).

**Figure 2.4** Schematic illustration of the characteristic stress evolution during drying of colloidal coatings on a rigid substrate.

**Figure 2.5** Schematic drawing of EPD cell showing the process.

**Figure 2.6** Evolution of the voltage in an electrophoretic deposition cell: The applied voltage is consumed by a voltage drop at each electrode and by an ohmic voltage drop over the suspension and the deposit.

**Figure 2.7** Schematic illustration of a possible influence of the growing deposit on the concentration of the reactant for the electrode reaction as a function of the distance from the electrode.

**Figure 2.8** Schematic diagram for the resistance of the EPD cell.

**Figure 2.9** Schematic representation of the deposition mechanism due to electrical double layer distortion and thinning.

**Figure 2.10** Schematic illustration of the electro-osmotic flow around a spherical charged particle.

## Figure List

---

**Figure 2.11** Schematic drawing of sintering of particle compacts with only changes in pore shape, and with both changes in pore shape and shrinkage.

## Chapter 3:

**Figure 3.1** Schematic diagram of the electrophoretic deposition apparatus.

## Chapter 4:

**Figure 4.1** Schematic drawing of the electro-osmotic flow around a positively charged particle.

**Figure 4.2** SEM images of the submicrometre YSZ particles.

**Figure 4.3** Agglomerate size distributions as a function of electrical conductivities of suspensions.

**Figure 4.4** Electrical conductivity and  $\zeta$ -potential as a function of iodine content (the particle concentration of the suspension is lower than  $2.5 \times 10^{-2} \text{ kg/m}^3$ ).

**Figure 4.5** Suspension electrical conductivity as a function of particle concentration.

**Figure 4.6** Both deposit weight and deposition rate/efficiency as a function of (a) deposition time, (b) electrical conductivity of suspensions, (c) applied voltage and (d) particle concentration in the suspension.

**Figure 4.7** Wet packing density i.e. volume occupation of particles in a wet coating as a function of (a) deposition time, (b) electrical conductivity of suspensions, (c) applied voltage and (d) particle concentration in the suspension.

**Figure 4.8** Effect of the electric field densification process on the wet packing density: (a) densification time; (b) electrical conductivity of solvent; (c) densification voltage. (For all densification processes, a deposit was first prepared by EPD using the following parameters, particle concentration= $50 \text{ kg/m}^3$ , applied voltage= $60 \text{ V}$ , deposition time= $240 \text{ s}$ ,  $\text{I}_2$  content= $0 \text{ kg/m}^3$ ).

## Figure List

---

**Figure 4.9** Effect of the electric field densification process on the wet packing density of coatings which were prepared (a) with different deposition times, and (b) under different applied voltages.

## Chapter 5:

**Figure 5.1** Agglomerate size distributions of particles (a) and (b) P0, (c) and (d) P2, (e) and (f) P5 and (g) and (h) P10 after different pre-treatments, i.e., mechanical stirred for 15 minutes, ultrasonication treated at 22.5kHz for 5 minutes, or settled for up to 60 minutes.

**Figure 5.2** SEM images of raw particles (a) P0, (b) P2, (c) P5 and (d) P10.

**Figure 5.3** Properties of P0, P2, P5 and P10 suspensions (a) zeta potential of particles and (b) electrical conductivity of suspensions.

**Figure 5.4** Agglomerate size distributions of centrifuge treated particles (a) and (b) P2 after 2000RPM centrifuge treated, (c) and (d) P5 after 2000RPM centrifuge treated and (e) and (f) P5 after 800RPM centrifuge treated.

**Figure 5.5** SEM images of 800RPM centrifuge treated P5 particles (a) P5- and (b) P5+.

**Figure 5.6** Measured properties of EPD coatings fabricated from various raw particles with different sizes (a) deposit weight, (b) wet packing density, (c) thickness of wet coating, and (d) coating thickness shrinkage during drying.

**Figure 5.7** EPD coatings fabricated with different particle sizes, (a) green density and (b) freely sintered density at 1250°C for 2 hours.

**Figure 5.8** SEM images of fracture surface of sintered coatings (a) P0 without densification, (b) P0 with densification, (c) P5 without densification, (d) P5 with densification.

**Figure 5.9** Microhardness of freely sintered EPD coatings fabricated with different sized particles.

**Figure 5.10** EPD of centrifuge treated P5 particles (a) deposit weight, (b) wet densities, (c) green densities and (d) hardness of 1250°C 2 hours sintered coatings.

## Figure List

---

**Figure 5.11** SEM images of fracture surfaces of sintered coatings at 1250°C for 2 hours fabricated with centrifuge treated particles: P5- (a) without and (b) with densification; and P5+ (c) without and (d) with densification.

**Figure 5.12** EPD of mixtures of P5+ and P0 particles at various compositions (a) deposit weight, (b) wet density, (c) green density and (d) microhardness of 1250°C 2 hours freely sintered coatings.

**Figure 5.13** SEM images taken from fracture surfaces of sintered coatings fabricated from mixture of P5+ and 25% of P0 (a) without the electric field densification and (b) with the electric field densification.

**Figure 5.14** Pore size distributions of freely sintered P5+ and P0 mixed sized coatings (25% P0) (a) accumulated volume intruded as a function of pore sizes and (b) volume intruded as a function of pore sizes.

**Figure 5.15** Current densities during electric field densification as a function of (a) densification time and (b) as a function of  $t^{-1/2}$ .

**Figure 5.16** Schematic illustration of the rearrangement of particles within wet EPD coatings during the electric field densification.

**Figure 5.17** Schematic illustration of green packing of EPD coatings without and with the electric field densification.

## Chapter 6:

**Figure 6.1** Optical microscope images used to measure the sintering shrinkage of EPD coatings, (a) green coating and (b) sintered coating.

**Figure 6.2** Free sintering (a) linear and (b) in-plane area shrinkages of EPD coatings with P0 and P5 as a function of isothermal temperature.

**Figure 6.3** Effect of sintering time on the linear shrinkage (a) of EPD coatings with P0 and P5 and (b) the shrinkage rate change with temperature.

## Figure List

---

**Figure 6.4** Sintered densities of EPD coatings fabricated with P0 and P5 as a function of sintering temperature (solid dots- freely sintered for 2 hours, hollow dots- constrained sintered for 2 hours, half hollow dots- freely sintered for 40 hours).

**Figure 6.5** Microhardness of freely and constrained sintered coatings fabricated with P0 and P5 particles as a function of sintering temperature (solid dots-freely sintered for 2 hours, hollow dots-constrained sintered for 2 hours, half hollow dots-freely sintered for 40 hours).

**Figure 6.6** SEM images of fracture surfaces of P0 coatings freely sintered 2 hours at (a) 1000°C, (b) 1100°C, (c) 1150°C, (d) 1200°C, (e) 1250°C and (f) 1300°C.

**Figure 6.7** SEM images of fracture surfaces of P0 coatings freely sintered 40 hours at (a) 1100°C and (b) 1150°C.

**Figure 6.8** SEM images of fracture surfaces of P5 coatings freely sintered 2 hours at (a) 1000°C, (b) 1150°C and (c) 1250°C.

**Figure 6.9** Densities of EPD coatings (green, freely sintered and constrained sintered) fabricated with P0, P2, P5 and P10 particles.

**Figure 6.10** SEM images from top surfaces of sintered (1250°C for 2 hours) EPD coatings fabricated with different sized particles, comparison of constrained sintered coatings (a), (c), (e) and (g), and freely sintered coatings (b), (d), (f) and (h).

**Figure 6.11** Pore size distributions of constrained and freely sintered EPD coatings: (a) P0 and (c) P5 are accumulated pore volumes as a function of pore size; (b) P0 and (d) P5 are pore volume intruded as a function of pore size.

**Figure 6.12** Schematic illustration for the unexpected pores detected during the mercury intrusion density measurement.

**Figure 6.13** Mechanical hardness of constraint sintered EPD coatings with different sized particles, and comparison to freely standing sintered coatings.



## Figure List

---

**Figure 6.14** SEM images of micro-indent ( $\approx 0.98\text{N}$  load) on top surfaces of constraint sintered EPD coatings fabricated from various particles.

**Figure 6.15** SEM images taken from top surfaces of constraint sintered P0 ((a) and (b)) and P5 ((c) and (d)) EPD coatings without and with electric field densification.

**Figure 6.16** Pore size distributions of constraint sintered EPD coatings with and without densification: (a) P0 and (c) P5 are accumulated pore volumes as a function of pore size; (b) P0 and (d) P5 are pore volume intruded as a function of pore size.

**Figure 6.17** Microhardness of constrained sintered EPD coatings fabricated from different sized particles with the electric field densification.

**Figure 6.18** SEM images from top surfaces of constrained sintered P0 coatings with various thicknesses (a)  $13\mu\text{m}$ , (b)  $18\mu\text{m}$  and (c)  $25\mu\text{m}$  at  $1250^\circ\text{C}$  for 2 hours.

**Figure 6.19** Microhardness of constrained sintered P0 and P5 coatings as a function of sintered coating thickness.

**Figure 6.20** Linear fit of (a) logarithm shrinkage-logarithm time of P0 coatings sintering at  $1100^\circ\text{C}$ , and Arrhenius plots of (b) logarithm shrinkage- $1/T(\text{K})$  of both P0 and P5 coatings.

**Figure 6.21** Schematic representation of the contact area between two sintered particles.

## Table List

### Chapter 2:

**Table 2.1** Representative colloidal-forming routes classified by consolidation mechanisms.

**Table 2.2** Mechanisms for mass transport during sintering.

**Table 2.3** Microstructural changes observed in the initial, intermediate and final stages during sintering of ceramic compacts.

### Chapter 5:

**Table 5.1** BET surface area and statistically quantified agglomerate-size results of raw particles.

**Table 5.2** Statistic quantified data of centrifuge treated particles.

### Chapter 6:

**Table 6.1** Densities of free and constrained sintered coatings via different methods.

**Table 6.2** Initial stage sintering parameters for Equation 6.5.

## Abstract

Yttria-stabilized-zirconia (YSZ) coatings have been fabricated on metallic (Fecralloy) substrates using a colloidal processing technique, namely electrophoretic deposition (EPD). The deposition of YSZ particles has been examined as a function of EPD conditions and suspension properties. The particle packing density, i.e., volume occupation of particles in a wet deposit, depends on deposition time, applied voltage, and the electrical conductivity and solid concentration of the suspension. In addition, the packing density of particles in a wet deposit further increased when the deposit was immersed in a pure solvent with application of a constant electric field. The packing mechanism of YSZ particles in the wet deposit was discussed based on the electro-osmotic flow in the wet deposit during EPD.

Four batches of different sized YSZ particles have been used to prepare suspensions for EPD. Agglomerate size distributions of those particles in acetylacetone suspensions have been examined. The particle packing density of wet EPD coating is determined by the agglomerate size. The green density of air dried EPD coating has been measured, and it was found that particles with a broad size distribution led to a high green density. EPD coatings fabricated from suspensions with same agglomerate size distributions have similar green densities (within  $\pm 2\%$ ), even though they have significantly different wet densities ( $>10\%$  difference). The hardness of free sintered (without substrate constraint,  $1250^{\circ}\text{C}$  for 2 hours) EPD coatings are controlled by the agglomerate size distribution of particles. Small particles provide EPD coatings with high hardness after the sintering. For EPD coatings with the mixed sized particles suspension, higher composition of small particles in the coating leads to higher hardness for sintered coatings. In addition, positions of small particles in an EPD coating with mixed sized particles can be rearranged by the electric field densification of the as-deposit EPD coating in a pure solvent with application of an electric field, and after the electric field densification small particles were found to be attached to the surfaces of large particles in the coating. The attachment of small particles to large particles leads to higher hardness of the coating after sintering. However, if the coating was fabricated from almost mono-sized submicron particles, the electric field

## Abstract

---

densification induced a lower hardness of the sintered coating due to particle agglomerations induced by the electrical field.

The sintering shrinkage of YSZ EPD deposit has been examined as a function of the sintering temperature and the isothermal treating time. The mechanism of mass transfer during sintering of YSZ compacts might be controlled by grain-boundary diffusion, and the activation energy for the diffusion of ionic species in YSZ compacts was calculated to be  $\sim 600\text{kJ/mol}$ . The EPD coatings were sintered on FeCrAlloy substrate. The substrate constraint resulted in a more porous microstructure compared with the free sintered coating. The constraint effect on sintering is more significant for coatings fabricated from small particles than those from large particles. The sintered coating has a more porous structure near the substrate. The specific particle packing condition induced by the electric field densification, i.e. small particles attached to the surfaces of large particles, leads a higher hardness of the sintered coating, though the effect was less significant than that in free sintered coatings.

## Declaration

---

### **Declaration**

No portion of the work referred to in this thesis has been submitted in support of an application for another degree or qualification of this or any other university or other institute of learning.

## **Copyright Statement**

- i. The author of this thesis (including any appendices and/or schedules to this thesis) owns any copyright in it (the "Copyright") and he has given The University of Manchester the right to use such Copyright for any administrative, promotional, educational and/or teaching purposes.
- ii. Copies of this thesis, either in full or in extracts, may be made only in accordance with the regulations of the John Rylands University Library of Manchester. Details of these regulations may be obtained from the Librarian. This page must form part of any such copies made.
- iii. The ownership of any patents, designs, trade marks and any and all other intellectual property rights except for the Copyright (the "Intellectual Property Rights") and any reproductions of copyright works, for example graphs and tables ("Reproductions"), which may be described in this thesis, may not be owned by the author and may be owned by third parties. Such Intellectual Property Rights and Reproductions cannot and must not be made available for use without the prior written permission of the owner(s) of the relevant Intellectual Property Rights and/or Reproductions.
- iv. Further information on the conditions under which disclosure, publication and exploitation of this thesis, the Copyright and any Intellectual Property Rights and/or Reproductions described in it may take place is available from the Head of School of Materials.

## Publication List

1. **Changzheng Ji**, Weihua Lan and Ping Xiao, "Fabrication of Yttria-Stabilized-Zirconia Coatings Using Electrophoretic Deposition: Packing Mechanism during Deposition", *Journal of the American Ceramic Society*, 91 (4) 1102-1110, 2008
2. **Changzheng Ji** and Ping Xiao, "Fabrication of Yttria-Stabilized-Zirconia Coatings Using Electrophoretic Deposition: Effects of Particle Size Distribution on Microstructure of EPD Coatings", In preparation for submission to *Journal of the American Ceramic Society*

## **Acknowledgements**

I would like to express my deepest gratitude to my supervisor, Prof. Ping Xiao, for his encouragement, guidance throughout my PhD studies, and providing financial support for my PhD study.

Special thanks to Dr. Ian Shapiro for his kind help on proofreading of this thesis.

I am grateful to all the technical staff and secretaries in the Manchester Materials Science Centre, for their support and help in various ways. Thanks are due to Michael Faulkner, Andy Wallwork, Andrew Forrest, Ken Walker, and Judith Shackleton for their friendly attitude and professional instruction in using SEM, Poremaster, Mastersizer, Micro-indentation, Optical microscope, XRD and other instruments.

I would like to thank my colleagues, Dr. Xin Wang, Dr. Xin Michael Wang, Dr. Xiaojuan Lv, Dr. Xingyuan Guo, Dr. Weihua Lan, Dr. Xiaofeng Zhao, Dr. Eddie Lopez-honorato, Dr. Lifeng Deng, Yan Zhao, Jun Tan, Hui Xu, Akio Shinmi, and Fan Yang for the support and those happy leisure time we spent together.

Last but not least, I would like to express my grateful thanks to my wife Yan Cao and my parents for their persistent support, encouragement and love.



## Chapter 1 Introduction

### §1.1 Introductory remarks

Ceramic coatings on metallic substrates have many practical applications, e.g., for the purposes of thermal protection <sup>[1-3]</sup>, wear and chemical resistance <sup>[4]</sup>, etc. Plasma spraying, chemical vapour deposition and physical vapour deposition are mainly used in current industrial practices, of which both the science and the technology have been improved considerably <sup>[5, 6]</sup>. However, they all have limitations on handling axially symmetric and complex-shaped substrates, and all those methods require expensive equipments, which makes them impractical for low-cost applications. Colloidal processing coating techniques, such as slurry/dip coating <sup>[7-9]</sup> and electrophoretic deposition (EPD) <sup>[10-12]</sup>, provide the potential to fabricate a new generation of ceramic coatings due to their advantages of less restriction in substrate shapes, controlled chemical composition and microstructure, simple equipment requirements and low costs. As a colloidal coating-fabrication method, EPD has attracted increasing attention both academically and practically for its outstanding potential abilities to tailor the microstructure and the thickness of ceramic coatings on complex-shaped substrates <sup>[10-12]</sup>. To date, many useful applications of the EPD technique have been reported, including advanced thin/thick films <sup>[13-15]</sup>, functionally graded/layered coatings <sup>[16-18]</sup>, nanostructured coatings <sup>[19, 20]</sup>, and 2-D and 3-D ordered, structured and micro-patterned coatings<sup>[21, 22]</sup>. The application-driven developments have led to a better understanding of the EPD process with positive implications in expanding its technological relevance. In particular in the area of coating and thin/thick film technology, EPD is seen as one of the enabling techniques capable of having a significant impact in the near future due to the simple equipment required, high versatility, low cost and rapid production time <sup>[10-12]</sup>.

In EPD, colloidal, charged particles deposit from a stable suspension onto an oppositely charged electrode (substrate) upon the application of a DC electric field, and the wet deposit then undergoes drying and sintering to form the EPD coating. The suspensions for EPD are prepared by dispersing particles in a liquid media, of which the dispersion and stability can be achieved or enhanced by adjusting interparticle forces <sup>[23, 24]</sup>. The deposit

weight and thickness can be controlled by EPD conditions, i.e. the properties of suspensions (particle concentration, viscosity, and electrical conductivity), deposition time and applied voltage <sup>[10]</sup>. The microstructures of EPD coatings can be manipulated by choosing particles with appropriate chemical compositions, crystal structures, surface morphologies, particle shapes and agglomerate sizes <sup>[10]</sup>. In the past, the microstructures of EPD coatings were mostly examined after drying or sintering <sup>[25, 26]</sup>. Although there were also many observations on clustering of deposited particles in the vicinity of the electrode in a DC electric field <sup>[27-30]</sup>, few studies were carried on the link between those electric field induced aggregations and the particle packing in the wet deposit and the microstructures (coating density and pore structure) of dried and sintered coatings. It is essential, not only for basic understanding of the EPD process but also for practically utilizing this promising coating technique, to clarify the relationship between EPD parameters and the particle packing densities of both wet and dry/sintered coatings.

One of the most attractive features of EPD for fabricating advanced ceramic coatings is the directly controlled microstructure from manipulating properties of raw particles, i.e. the chemical composition, the crystal structure, the surface condition, and particle/agglomerate size <sup>[10, 24]</sup>. It is commonly accepted that ceramic compacts with high green density and uniform small pore sizes can benefit the subsequent sintering process <sup>[31-33]</sup>. Both experimental <sup>[34-36]</sup> and modelling <sup>[37, 38]</sup> results on the effect of particle size on the compact density has suggested that mixed sized (bimodal or trimodal mixtures) particles provide higher green densities than uniform sized particles do. McGeary <sup>[38]</sup> modelled the particle packing of the bimodal sized mixture and revealed that the maximum density is achieved when the size ratio (large to small) is greater than 7. The studies on the particle packing efficiency for achieving high density have led to extensive uses of mixed sized particles in practically ceramic processing <sup>[39]</sup>. A controllable green density is also desired for EPD coatings, so it is a good attempt to employ mixed sized particles to fabricate high green density EPD coatings. However, only a few studies have been reported on the particle size effect on the EPD process by examining the suspension stability <sup>[40]</sup>, the electrophoretic mobility <sup>[41]</sup>, and the crack formation <sup>[42]</sup>. It is very important to clarify the packing behaviours of different sized particles during EPD before applying mixed sized particles to obtain high density EPD coatings.

For application, in most cases protecting metallic substrates, the green coating needs to be sintered on a rigid substrate to gain the necessary consolidation. In this case of constrained sintering, the in-plane shrinkage is inhibited and all densification takes place in the thickness direction <sup>[43-45]</sup>. An in-plane biaxial tensile stress applied by the substrate develops in the ceramic coating during sintering due to the different shrinkage rates of the ceramic coating and the rigid substrate <sup>[46]</sup>. These tensile stresses, which reduce the sintering potential for the densification of the ceramic coating, thereby resulting in a low sintered density, can be released by cracking, delamination or viscous deformation <sup>[46, 47]</sup>. It is commonly accepted that smaller particles sinter more easily due to their higher surface curvatures <sup>[31, 48]</sup>. However, for the EPD process, it is still a big challenge to achieve high particle packing density with mono-sized small particles due to limited packing density for fine particles, i.e. for nano-particles or submicron-particles <sup>[49]</sup>. As a consequence, the low particle packing density of the EPD coating may induce severe volume shrinkage during both drying <sup>[7-9, 50, 51]</sup> and sintering <sup>[52-54]</sup> processes, and which in turn cause very high tendencies of cracking in the coating due to the substrate constraint effect. Applying the achievements of bimodal particle packing <sup>[34-38]</sup> to the EPD coating, a higher particle packing density is expected by using both small and large particles to fabricate the coating. However, large particles are resistant to sintering, so a balance between the particle packing density and the sinterability of EPD coatings is expected to set up by manipulating different sized particles in the EPD process.

Zirconia is one of the most researched ceramics and has excellent thermal-mechanical properties, i.e. high hardness and elastic modulus, high thermal expansion coefficient, and low thermal conductivity. In practical applications, 8mol% YO<sub>1.5</sub> stabilized zirconia (8YSZ) has been widely used for thermal barrier coatings (TBCs) <sup>[3]</sup>.

### **§1.2 Aim of this project**

The Ceramic Coatings Group at the Manchester Materials Science Centre (MMSC) has a solid background in both fabrication and characterisation of TBCs. In an attempt to develop ceramic coatings with controllable microstructure for the next generation TBCs, a suspension-based deposition technique, i.e. EPD, was suggested. During the colloidal EPD

processing, raw particles pass between four main states to form the final product, namely well dispersed suspension, wet consolidated deposit, dry green packing, and highly densified sintered coating. Each step is crucial in determining the microstructure of the final coating. As there are high purity 8YSZ raw particles available commercially, this project concentrates on the processing route starting from the preparation of stable suspensions and the formation of wet EPD coatings.

In this study, 8YSZ raw particles were dispersed in acetylacetone to form stable suspensions, and EPD was carried out in the suspensions. The EPD conditions, i.e. particle concentration in the suspension, electrical conductivity of the suspension, deposition time, and applied voltage, were studied by linking them to the deposit weight, the deposition efficiency and the particle packing density of wet coatings. The particle packing mechanisms during EPD were also proposed by means of the electric field induced electro-osmotic flow within the deposited wet coating. Then different sized particles were deposited by EPD, and the size effects on coating densities (wet, green and sintered) were examined. The sintering behaviour of the EPD compacts, i.e. sintering shrinkage and microstructural development, were also examined, and the substrate constraint effect was highlighted by comparing the microstructures of free sintered and constrained sintered coatings.

### **§1.3 Thesis outline**

Chapter 2 is a literature review, in which the colloidal processing of ceramics, principles of the EPD technique, and the sintering of ceramic coatings are reviewed.

Chapter 3 summarises the experimental procedure and the characterisation methods. The source materials and equipment involved in this study are also introduced.

Chapter 4 is mainly focused on the effects of EPD conditions, i.e. deposition time, particle concentration in the suspension, electrical conductivity of the suspension, and applied voltage, on the particle packing density (wet coating). An electric field densification process, applying an electric voltage on an as-deposited wet EPD coating in pure solvent, was introduced to help understand the particle packing mechanism during EPD.

## Chapter 1-Introduction

---

Chapter 5 is concerned with the evolution of particle packing from wet deposit to the dry and free sintered forms of EPD coating. The particle size effects on the coating densities and microstructures were systematically investigated. EPD coatings with mixed sized particles were also fabricated, and the positions of small particles in the coating were found important in determining the mechanical hardness of free sintered coatings.

Chapter 6 presents the results on the sintering of EPD coatings. The EPD coatings were isothermally sintered over a temperature range from 1000°C to 1300°C, and the sintering densification was examined to study the microstructural development of EPD coatings during sintering. The microstructure of EPD coatings sintered under constraint by the metallic substrates was contrasted with those of free sintered coatings, and the effects of substrate constraint were highlighted.

Chapter 7 describes conclusions obtained from the results.

Chapter 8 gives suggestions for further researches.

## Chapter 2 Literature Review

### §2.1 Colloidal processing of ceramics

Though ceramics have been processed by colloidal routes for several millennia, the term “colloidal” was first introduced by Graham <sup>[55]</sup> in 1861 to distinguish different types of matter (i.e., crystalloids and colloids), but later it became apparent that colloids are not separate types of matter but matter (i.e. liquids or solids) in a particular state of subdivision in which effects connected with the surface are pre-eminent. Particle sizes in colloidal systems generally range from 1nm-10µm and a distinguishing feature of all colloidal systems is that the dispersing medium is continuous. Colloidal systems can be dispersed in either a gas (aerosol) or a liquid (sol/emulsion) <sup>[31]</sup>.

For ceramic processing, liquid dispersing mediums are widely employed for preparation of the colloidal suspension. Colloidal processing offers the potential to reliably produce ceramic bulks, coatings and thin films through careful control of the suspension properties and its evolution during fabrication <sup>[32, 33, 56, 57]</sup>. The suspension stability plays an important role in controlling the quality of a product. A stable suspension with well-dispersed particles will provide a dense and homogeneous compact, whereas, an unstable suspension will result in agglomeration of particles, resulting in inhomogeneous packing of the particles which will induce differential sintering and lead to defects in the final product <sup>[58]</sup>.

Solid particles generally have a higher density than the liquids that might be used to suspend them, so they are inclined to sink. Brownian motion, however, will keep particles suspended if they are sufficiently small. To understand the stability of suspensions it is also necessary to consider the forces that act between particles, which can be either attractive or repulsive depending on a variety of conditions. In simple terms, if the forces are repulsive then particles remain separated and can stay suspended for long periods of time. On the other hand, attractive forces between particles cause small particles to stick together and form agglomerates which may become large enough and heavy enough to fall out of suspension and form a sediment <sup>[59]</sup>.

### §2.1.1 Interparticle energies

The colloidal stability is governed by the total interparticle potential energy,  $V_{total}$ , which can be expressed by [32, 60].

$$V_{total} = V_{vdW} + V_{elect} + V_{steric} + V_{structural} \quad \text{Equation 2.1}$$

where  $V_{vdW}$  is the attractive potential energy due to the long-range van der Waals (vdW) forces between particles,  $V_{elect}$  the repulsive potential energy resulting from electrostatic interactions between charged particle surfaces,  $V_{steric}$  the repulsive potential energy resulting from steric interactions between adsorbed species on particle surfaces, and  $V_{structural}$  the potential energy resulting from the presence of non-adsorbed solvent molecules between particles.

In a colloidal system, when two particles collide due to random thermal (Brownian) motion they will stick or rebound, depending on their interaction energy. Therefore, this interaction energy determines the sticking efficiency or the colloidal stability. Two types of colloidal stability can be achieved by introducing repulsive forces between particles to counteract the attractive vdW forces. One is electrostatic stabilization resulting from the impingement of two diffuse double layers as two colloidal particles collide. The other is steric stabilization resulting from the impingement of structural molecules (i.e., polymer or surfactant) adsorbed on the particle surface as two particles collide [31].

#### §2.1.1.1 VdW attractive energy

Hamaker [61] in 1937 showed the potential energy of attraction between two spherical interacting particles, with radii  $a_1$  and  $a_2$ , of the same material separated by a distance  $l$  (the minimum surface distance),  $V_{vdW}$  is given by:

$$V_{vdW} = -\frac{A}{6} \left[ \frac{2a_1a_2}{l^2 + 2a_1l + 2a_2l} + \frac{2a_1a_2}{l^2 + 2a_1l + 2a_2l + 4a_1a_2} + \ln\left(\frac{l^2 + 2a_1l + 2a_2l}{l^2 + 2a_1l + 2a_2l + 4a_1a_2}\right) \right] \quad \text{Equation 2.2}$$

where  $A$  is the Hamaker constant which is defined as:

$$A = \pi^2 n^2 C_l \quad \text{Equation 2.3}$$

where  $\pi$  is the circular constant,  $n$  is the number of atoms per unit volume and  $C_I$  is the London constant taken to be

$$C_I = \frac{3}{4} h \nu_0 \alpha_j \quad \text{Equation 2.4}$$

where  $\alpha_j$  is the polarizability and  $h \nu_0$  is approximately the ionization energy of the material,  $h$  is the Planck constant <sup>[31]</sup>.

The long-range attractive vdW forces between particles need to be mitigated during the colloidal processing to achieve the desired suspension stability. Therefore some types of interparticle repulsion, such as electrostatic, steric, or depletion forces (structure energy in Equation 2.1), must be introduced to overcome the vdW forces, as shown in Figure 2.1.

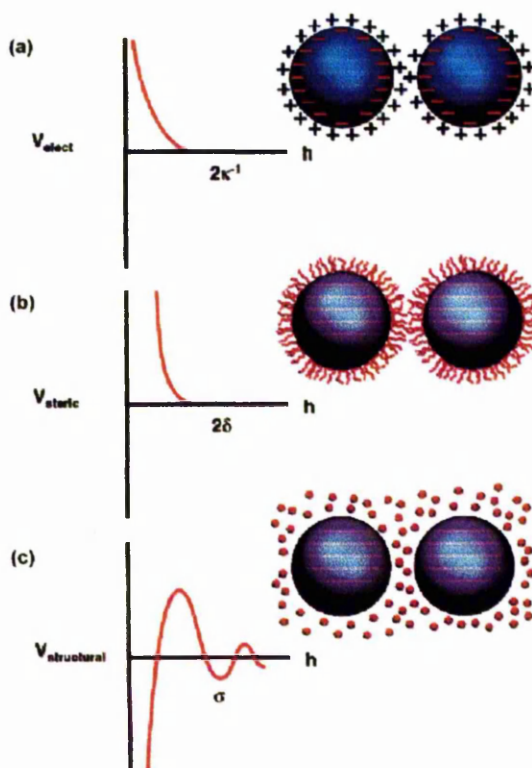
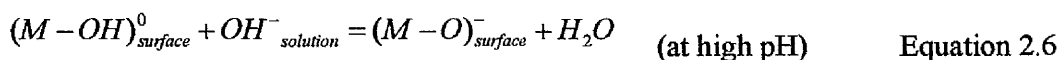
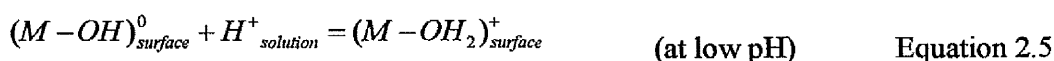


**Figure 2.1** Schematic illustration of the interaction potential energy and relevant length scales for (a) electrostatic, (b) steric, and (c) structural contributions, where  $\kappa^{-1}$  is the effective double-layer thickness,  $\delta$  the adsorbed layer thickness, and  $\sigma$  the characteristic size of species resulting in ordering within the interparticle gap <sup>[32]</sup>



### §2.1.1.2 Electrostatic interaction energy

Ceramic particles are of relatively low solubility so surface chemistry tends to control their charging behaviour. The surface of a particle may become charged by 1) the desorption of ions at the surface of the particle, a typical example of charging by desorption is the liberation of alkali from the surface of a clay mineral such as kaolinite; 2) a chemical reaction between the surface and the liquid medium changing the composition of the surface, e.g. for most oxides with a hydrated surface the chemical reactions on the surface are shown as Equations 2.5 and 2.6; and 3) the preferential adsorption of specific additive or impurity ions from the chemical solution adjacent to the particle, such as carbon black can become negatively charged by adsorption of anionic surfactants <sup>[62, 63]</sup>.



Ions or polar molecules in the solution surrounding the particle may respond to the charged surface. Coulombic forces will repel like-charged ions but attract polar molecules and oppositely charged ions, known as counterions, into a region near the surface increasing their concentration relative to that in the bulk. Although the overall charge neutrality must remain, a difference in electrical potential between the surface and the bulk solution can be affected as shown in Figure 2.2. The potential gradient will not be sharp, because thermal vibration of molecules of the solution may cause the diffusion of some counterions. A model (widely known as diffuse electrical double-layer model) <sup>[64-66]</sup> has been set up to describe the potential gradient in the diffuse layer (Figure 2.2) based on a uniformly charged surface, an adjacent solution with uniform dielectric constant  $\epsilon_r$ , and point charges.

This model describes a charged particle with a relatively immobile adsorbed layer of counterions, called the Stern layer, and a concentration gradient of counterions in a diffuse layer which attains steady-state configuration.

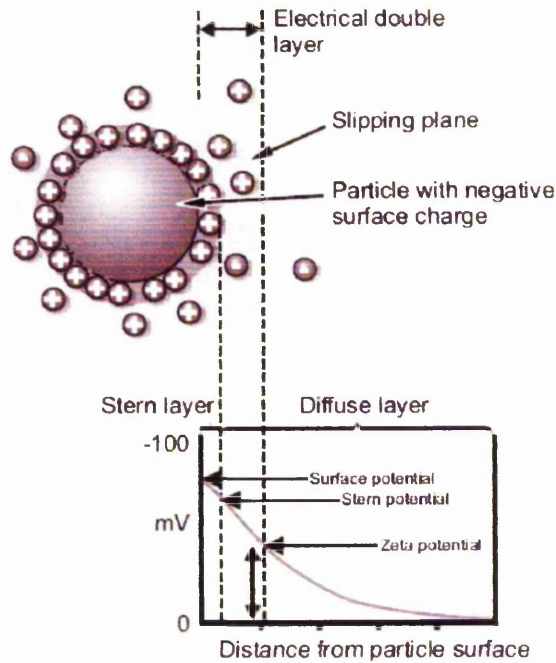


**Figure 2.2 Schematic of the electrical double layer model for particle charging in a polar liquid and Gouy-Chapman profile of the electrical potential <sup>[48]</sup>**

Assuming that the distribution of charge is described by the Boltzmann equation, the concentration of counterions  $N_i$  in the diffuse layer relative to the concentration in the bulk solution  $N_{i0}$  is:

$$\frac{N_i}{N_{i0}} = \exp\left(-\frac{U_i}{k_B T}\right) \quad \text{Equation 2.7}$$

where  $k_B$  is the Boltzmann constant,  $T$  is the absolute temperature and the potential energy of the ion  $U_i$  is a function of the valence of the ion  $Z_i$  and the electrical potential  $\psi$  at that position:

$$U_i = Z_i(e\psi) \quad \text{Equation 2.8}$$

where  $e$  is the electron charge. For the case of a surface potential  $\leq 100\text{mV}$ :

$$\psi = \psi_0 \exp(-x\kappa) \quad \text{Equation 2.9}$$

## Chapter 2-Literature Review

where  $\psi_0$  is the surface potential of the particle,  $x$  is the distance from the Stern layer, and  $\kappa$  is defined as:

$$\kappa = \left( \frac{\epsilon_r \epsilon_0 k_B T}{e^2 \sum N_i Z_i^2} \right)^{-\frac{1}{2}} \quad \text{Equation 2.10}$$

where  $\epsilon_r$  and  $\epsilon_0$  are respectively the relative dielectric constant of the solvent and the dielectric permittivity of the vacuum, and  $\kappa^{-1}$  represents the thickness of the double layer. It is difficult to provide an exact analytical expression for the electrostatic potential energy, so that proper approximations were made to utilize the parallel plate electrostatic interaction energy,  $V_{\text{elect}}^P(l)$ , as an approximation for the interaction energy between two spheres,  $V_{\text{elect}}^S(l)$ . The approximation is given by [67]:

$$V_{\text{elect}}^S(l) = \int_0^\infty 2\pi l V_{\text{elect}}^P(l) dl \quad \text{Equation 2.11}$$

This approximation is good when the curvature of the surface is small compared to the double layer thickness (i.e.,  $\kappa a > 5$ ). Using this result, the interaction energy between two unequally sized spheres ( $a_1$  and  $a_2$ ) is given by [68]:

$$V_{\text{elect}}^S(l) = \frac{\epsilon_r \epsilon_0 a_1 a_2 (\psi_{01}^2 + \psi_{02}^2)}{4(a_1 + a_2)} \left\{ \frac{2\psi_{01}\psi_{02}}{\psi_{01}^2 + \psi_{02}^2} \ln \left[ \frac{1 + \exp(-\kappa l)}{1 - \exp(-\kappa l)} \right] + \ln[1 - \exp(-2\kappa l)] \right\} \quad \text{Equation 2.12}$$

where  $\psi_{01}$  and  $\psi_{02}$  are the surface potentials on the two spheres. Equation 2.12 can be reduced to:

$$V_{\text{elect}}^S(l) = \frac{1}{2} \epsilon_r \epsilon_0 a \psi_0^2 \ln[1 + \exp(-\kappa l)] \quad \text{Equation 2.13}$$

when the spheres are the same size, with equal surface potentials.

On the other hand, for particles that have large surface curvature or the double layer around each particle is extensive (i.e.,  $\kappa a < 5$ ), the equation can be written as:

$$V_{\text{elect}}^S(l) = 2\pi \epsilon_r \epsilon_0 a \psi_0^2 \exp(-\kappa l) \quad \text{Equation 2.14}$$

In view of the importance of electro-kinetic phenomenon in colloid and surface chemistry, charged particles in a suspension will respond to an imposed potential difference, i.e. an applied electric field, and the particle velocity is called the electrophoretic velocity. In a similar manner, the ionic solution adjacent to the wall of a capillary with an electrical double layer will be motivated to flow if a potential difference is imposed, and this is called electro-osmotic flow. During the flow, a hydrodynamic plane of slippage must occur somewhere in the double layer (as shown in Figure 2.2). Therefore a slipping plane is defined as where liquid is forced to move relative to the particle, at which the potential is referred to as the zeta potential,  $\zeta$ . The  $\zeta$ -potential can be measured by different methods<sup>[69, 70]</sup>, and is generally used to study the colloidal stability. The higher the  $\zeta$ -potential, the better the dispersion is<sup>[71]</sup>. Investigations of the  $\zeta$ -potential of particles have been a major topic in the colloidal field, which is influenced by particle source<sup>[72]</sup>, electrolyte concentration<sup>[73]</sup>, particle concentration<sup>[74, 75]</sup>, pH value<sup>[76]</sup> and hydration state<sup>[77]</sup>, etc. Besides the  $\zeta$ -potential, the point of zero charge (PZC)<sup>[78]</sup> and the isoelectric point (IEP) are another two important parameters for the characterization of colloidal stability. The PZC corresponds to the condition at which the surface charge of particles is zero, while the IEP corresponds to  $\zeta = 0$ .

### §2.1.1.3 Steric repulsion energy

When the surface potential is small or the double layer thickness is thin, and the electrostatic repulsion is not sufficient to stabilize the colloidal suspension, another form of stabilization is needed - steric stabilization, which can be achieved by polymer adsorption to the particle surface in both polar and nonpolar solvents. In general, the steric interaction is dependent on the thickness of the adsorbed layer, the chemical nature of the adsorbed molecules and the chemical nature of the solvent. To be effective, the adsorbed polymer layer should meet the following requirements: 1) thick enough to shield the attractive vdW forces; 2) complete coverage of the particle surface, if not flocculation may form<sup>[79]</sup>; 3) firmly adsorbed to the particle surface to prevent being pushed away during particle collisions; and 4) a good condition in the solvent, i.e., no chemical reactions between solvent and the polymers.

Steric interactions occur when particles approach one another at a separation distance less than twice the adsorbed layer thickness ( $l < 2\delta$ ). The interpenetration and compression of the adsorbed layers dominate the interaction energy,  $V_{steric}$ , which were given by [32, 80-82].

$$V_{steric} = \frac{32\pi a k_B T \bar{\phi}_2^a (0.5 - \chi)}{5v\delta^4} \left(\delta - \frac{l}{2}\right)^6 \quad \text{Equation 2.15}$$

for  $\delta < l < 2\delta$ , where  $\bar{\phi}_2^a$  is the average volume fraction of adsorbent in the layer,  $\chi$  is the Flory-Huggins interaction parameter, a measure of solvent quality, and takes a value of 0.45-0.49 [83], and  $v$  is the molar volume of the solvent. At smaller interparticle separations (i.e.,  $l < \delta$ ), the polymer density is assumed to be uniform, the steric energy,  $V_{steric}$ , is given by the sum of interpenetration,  $V_{steric}^{inter}$ , and the elastic,  $V_{steric}^{elas}$ , terms:

$$V_{steric}^{inter} = \frac{4\pi a \delta^2 k_B T \bar{\phi}_2^a (0.5 - \chi)}{v} \left( \frac{l}{2\delta} - \frac{1}{4} - \ln \frac{l}{\delta} \right) \quad \text{Equation 2.16}$$

$$V_{steric}^{elas} = \frac{2\pi a \delta^2 k_B T \bar{\phi}_2^a \rho}{M^a} \left\{ \frac{l}{\delta} \ln \left[ \frac{l}{\delta} \left( \frac{3 - \frac{l}{\delta}}{2} \right)^2 \right] - 6 \ln \left( \frac{3 - \frac{l}{\delta}}{2} \right) + 3 \left( 1 - \frac{l}{\delta} \right) \right\} \quad \text{Equation 2.17}$$

where  $\rho$  is the density and  $M^a$  the molecular weight of the adsorbed species.

#### §2.1.1.4 Structural energy

In previous discussions, the liquid separating the surfaces has been treated as a structureless continuum, which is a perfectly adequate approximation for large surface separations. However, for a sufficiently fine scale analysis, the discreteness of solvent should be considered. The structural energy,  $V_{structural}$ , is so called because it is a consequence of the arrangement of molecules, or structure, of the solvent between the surfaces (Figure 2.1 (c)).

#### §2.1.1.5 DLVO theory

In the 1940s, Russian scientists Derjaguin and Landau [84] and Dutch scientists Verwey and Overbeek [85] independently suggested that the interparticle forces determining colloidal

stability were given by the sum of vdW attraction and double layer repulsion. The resultant theory, now known as DLVO theory, is treated as the fundamental theory of colloid science.

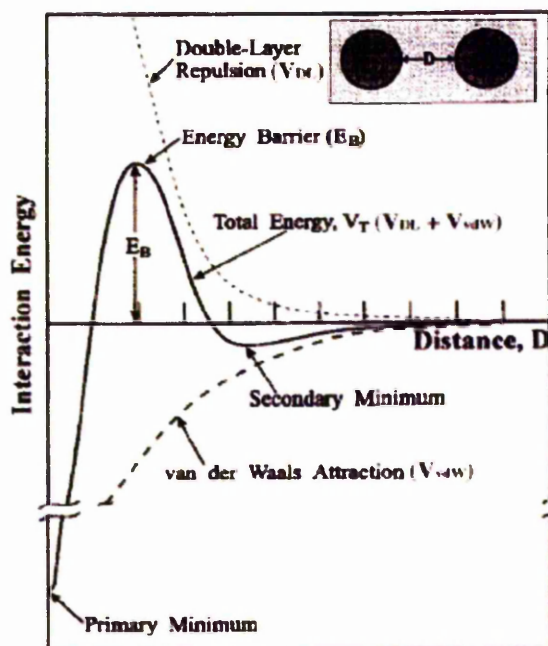


**Figure 2.3 Potential energy of interaction between two particles with electrical double layers (the secondary minimum is not expected when  $\kappa a < 1$ )** <sup>[86]</sup>

Figure 2.3 shows schematically the interparticle potential energy as a function of the separation between two particles. It indicates that at both small and large interparticle separations, the vdW attraction dominates, whereas, at an intermediate separation, the electrostatic repulsion dominates and forms an energy barrier to prevent particles touching. The height of this energy barrier, i.e. primary maximum  $E_B$ , depends on the surface potential and the double-layer thickness. The classical DLVO theory treats counterions as point charges and assumes that the double-layer thickness decreases to zero with large additions of electrolyte to produce an identical interparticle potential to that at the IEP where only the vdW attraction is present. However, Lange and coworkers <sup>[87-89]</sup> found that weakly attractive interparticle potentials could be achieved by adjusting the pH far from the IEP to produce a long-range electrostatic potential first, and subsequently adding excessive amounts of an indifferent electrolyte. In such a case, particles reside in a shallow potential

well, referred to as the secondary minimum in Figure 2.3, and are attracted to one another by the vdW attraction. They only feel repulsion at very small separation distances. When the pH is at the IEP in an aqueous suspension, particles are brought into contact by the vdW attraction and reside in a deep potential well, referred to as the primary minimum in Figure 2.3. Lange et al. <sup>[87-89]</sup> produced weakly attractive, aqueous alumina suspensions at pH conditions below the IEP point and found that the yield strength increased with increased electrolyte concentration. The weakly attractive network can easily be overcome by shear forces, therefore dense packing of particles can be obtained during consolidation <sup>[88, 90]</sup>. In some cases, such weakly attractive network is necessary to avoid sedimentation <sup>[91]</sup>, or to avoid damage during strain recovery after consolidation <sup>[92]</sup>.

### §2.1.2 Suspension rheology

The flow properties of suspensions, which are extremely important for processing and forming considerations, are determined by the particle volume fraction ( $\phi_p$ ), size distribution and interparticle forces.

The apparent viscosity ( $\eta$ ) is related to the applied shear stress ( $\tau$ ) and shear rate ( $\dot{\gamma}$ ) by the following expression:

$$\tau = \eta \dot{\gamma} \quad \text{Equation 2.18}$$

Various types of flow behaviour can be observed under steady shear depending on suspension composition and stability. Newtonian behaviour is the simplest flow response, where viscosity is independent of shear rate; pseudoplastic or shear-thinning behaviour occurs when the viscosity decreases with shear rate; dilatant or shear-thickening behaviour occurs when the viscosity increases with shear rate <sup>[32]</sup>.

Dilute ceramic suspensions,  $\phi_p < 0.3$ , exhibit Newtonian rheology. The viscosity of a suspension,  $\eta$ , is always higher than that of the pure solvent,  $\eta_s$ , and the relation between  $\eta$  and  $\eta_s$  can be expressed as <sup>[31]</sup>:

$$\frac{\eta}{\eta_s} = \left[ \frac{1 + \frac{\varphi_p}{2}}{(1 - \varphi_p)} \right]_{sphere} \quad \text{Equation 2.19}$$

Equation 2.19 was derived for spherical particles and is valid for a mixture of different sized spheres at dilute concentrations ( $\varphi_p < 0.3$ ). It has been shown experimentally <sup>[93]</sup> that the viscosity of non-spherical particle suspensions increases proportionally to the square of the ratio between the large and small axes for ellipsoids of revolution when the particles are prolate and increases directly proportional to the ratio between the large and small axes for ellipsoids of revolution when the particles are oblate <sup>[94]</sup>. The reason for this effect is that anisotropic particles rotate in the shear field and have an effective volume fraction larger than that of the particles themselves.

For most systems, the viscosity of a suspension changes drastically at a critical particle concentration,  $\varphi_c$ , which corresponds to the formation of a space-filling particle network. When  $\varphi_p < \varphi_c$ , the suspension has no yield stress. Above  $\varphi_c$ , the suspension can sustain a stress before yielding, showing significant elasticity. The magnitude of  $\varphi_c$  depends on the interparticle forces. Higher repulsive forces between particles induce higher  $\varphi_c$ . And for a given  $\varphi_p$ , the viscosity of a suspension shows an inversely proportional relationship to the zeta potential of particles <sup>[95]</sup>.

Zaman and Dutcher <sup>[96]</sup> developed an equation to explain the dependence of suspension viscosity on the particle sizes ( $a_p$ ), when mono-sized particles were dispersed in the suspension:

$$\log \eta = -\alpha a_p + \beta \quad \text{Equation 2.20}$$

where both  $\alpha$  and  $\beta$  are model parameters that change with shear rate, and  $a_p$  is the particle size. A clear reduction in the viscosity has been observed with an increase in the particle size distribution with comparable volume fractions <sup>[97, 98]</sup>.



### §2.1.3 Colloidal consolidation

Consolidation of colloidal suspensions into dense, homogeneous bodies is a crucial feature of colloidal processing. Several colloidal routes have been developed to produce ceramic components of various geometric shapes, complexity, and microstructural control based on various consolidation mechanisms, i.e. consolidation via fluid flow/removal, via particle flow or via gelation. Colloidal consolidation methods are listed in Table 2.1.

**Table 2.1 Representative colloidal-forming routes classified by consolidation mechanisms <sup>[32]</sup>**

Forming method	Consolidation Mechanisms	
Slip casting	A. Fluid removal	Fluid flow into porous mold driven by capillary forces
Pressure filtration		Fluid flow through porous filter driven by an applied pressure
Osmotic consolidation		Fluid flow through a semipermeable membrane driven by osmotic pressure difference
Tape Casting		Fluid removal due to evaporation
Sedimentation	B. Particle flow	Particles settle due to gravity
Centrifugal consolidation		Particles flow due to applied centrifugal force
Electrophoretic deposition		Particles flow due to applied electric field
Aqueous injection molding	C. Gelation	Physical organic gel forms in response to a temperature change
Gelcasting		Cross-linked organic network forms because of chemical reaction
Direct coagulation casting		Colloidal gel forms because of flocculation

Particle consolidation into dense coatings or bodies accompanies fluid removal in several forming routes, including pressure filtration <sup>[99-101]</sup>, slip casting <sup>[102, 103]</sup>, tape casting <sup>[104-106]</sup> and osmotic consolidation <sup>[107, 108]</sup>. During these processes, a portion of the liquid vehicle is removed to yield a saturated ceramic body.

Particle consolidation into a dense coating or body occurs via particle flow in response to an applied force in several forming routes, including sedimentation <sup>[109-114]</sup>, centrifugation <sup>[115-117]</sup> and electrophoretic deposition <sup>[10-12]</sup>. Particles flow in response to gravitational forces during sedimentation; and in response to centrifugal forces during centrifugation; and in response to an applied electric field during EPD, to form a certain shaped ceramic body.

The formation of dense coatings or bodies occurs via gelation in several forming routes, including aqueous injection molding <sup>[118, 119]</sup>, gelcasting <sup>[120-122]</sup>, and direct coagulation casting <sup>[123]</sup>. These methods rely on either physical or chemical approaches to induce gelation in a colloidal suspension. After the consolidation, the ceramic coating or body subsequently needs to be dried to form a green compact.

### **§2.1.4 Drying process**

To remove the solvent used to suspend the ceramic particles for green body fabrication, the green body is heated or placed in an atmosphere where the solvent evaporates. Depending on the type of ceramic particles used and the green body fabrication process different solvents are used. Solvents are typically organics or water. Organic solvents are chosen to easily wet the ceramic particles surfaces and easily evaporate during drying. A low enthalpy of vaporization and a reasonably high vapour pressure are important for a solvent to evaporate easily. Drying is a multistage process which involves capillary driven fluid flow, viscous deformation of the coating (or body), evaporation, and diffusion. The removal of the liquid required for the colloidal processing is often accompanied by problems such as dimensional shrinkage, segregation, and cracking <sup>[7-9, 50, 51, 124-130]</sup>.

#### **§2.1.4.1 Drying stages**

Drying of colloidal assemblies can be divided into three stages: 1) constant-rate period (CRP), 2) first falling-rate period (FRP1), and 3) second falling-rate period (FRP2) <sup>[131, 132]</sup>.

In the CRP, the drying rate is controlled by external conditions. Fluid is supplied via capillary-driven transport to the external surfaces of the component, where evaporation

takes place. The driving force is the capillary force ( $P_c$ ) which is developed in liquid-filled surface pores and is related to the radius of curvature ( $r_{pore}$ ) of the meniscus which forms to minimize the high potential solid-vapour interface and maximize the relative low potential liquid-vapour and liquid-solid interfaces:

$$P_c = -\frac{2\gamma_{LV}}{r_{pore}} \quad \text{Equation 2.21}$$

where  $\gamma_{LV}$  is the surface tension of the liquid. Under constant external conditions, the evaporation rate ( $V_E$ ) is determined by the difference between the vapour pressures of the liquid ( $P_V$ ) and the ambient vapour pressure ( $P_A$ ):

$$V_E = K_d(P_V - P_A) \quad \text{Equation 2.22}$$

$$P_V = P_0 \exp\left(-\frac{P_c V_m}{R_g T}\right) \quad \text{Equation 2.23}$$

where  $K_d$  is a factor depending on the design of the drying chamber, air movement rate, etc,  $V_m$  is the molar volume of the liquid,  $R_g$  is the ideal gas constant and  $T$  is the temperature in degrees kelvin. When the meniscus is small enough to fit into the pore, the capillary force reaches its maximum. Assuming that the pore is in a cylindrical shape, the minimum radius ( $r_{min}$ ) of curvature of the meniscus is:

$$r_{min} = \frac{r_{pore}}{\cos\theta} \quad \text{Equation 2.24}$$

where  $r_{pore}$  is the pore radius and  $\theta$  is the contact angle of the liquid on the particle surface. When the pores are on the scale of micrometer, no significant reduction in  $P_V$  can occur (Equation 2.23), and the evaporation rate per unit area of the drying surface is independent of time and is close to that from an open dish of liquid.

As drying proceeds, large pores drain as fluid is drawn to smaller pores with higher suction potential. The drained pores may penetrate far into the component interior, provided the rate of capillary redistribution of fluid exceeds the evaporation rate. The transition to the FRP1 occurs when fluid can no longer be supplied to the external surfaces at a rate equivalent to the evaporation rate observed during the CRP. In FRP1, evaporation occurs

from the fluid menisci, causing them to retreat into the body, i.e. the funicular state. As further evaporation occurs, fluid resides in isolated pockets, i.e. the pendular state, thereby marking the transition to FRP2. In FRP2, the remaining liquid is removed from the body by vapour-phase diffusion [51, 125, 131].

### §2.1.4.2 Constrained drying and crack formation

Stress evolution in ceramic coatings prepared by colloidal methods on a rigid substrate has been extensively studied. Chiu et al [128, 129], Guo et al [57] and Lan et al [7-9] studied the drying of coatings composed of ceramic particles and solvent without binders. The in situ stress evolution was measured using an optical interference method and the tensile stress was attributed to the capillary force in the wet coating. The stress was greatest when the air-liquid interface began to recede into the coating then decayed to zero or a lower residual stress when liquid drained from the pores in the coating. Four regions have been delineated: 1) stress rise ( $\sigma_{\text{rise}}$ ); 2) stress maximum ( $\sigma_{\text{max}}$ ); 3) stress decay ( $\sigma_{\text{decay}}$ ); and 4) residual stress ( $\sigma_{\text{res}}$ ), as schematically illustrated in Figure 2.4.

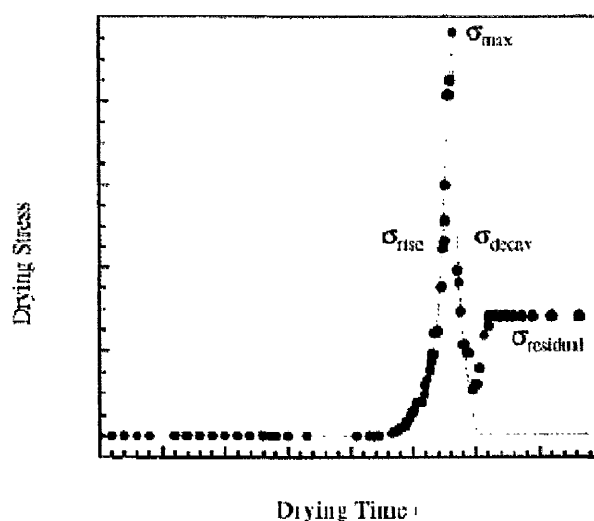


**Figure 2.4 Schematic illustration of the characteristic stress evolution during drying of colloidal coatings on a rigid substrate [32]**

When the stress exceeded the cohesive strength of the coating, cracks formed and propagated. These failures could be avoided by reducing the coating thickness or the stress.

Critical coating thickness above which failures occurred could be decided by statistical experiments <sup>[128, 129]</sup>. The stress could be reduced by decreasing liquid surface tension or increasing particle/agglomerate size in the coating <sup>[128, 129]</sup>.

A common observation in drying processes is that a colloidal ceramic coating is more likely to crack during drying when the coating is thick or the drying rate is high <sup>[126, 131, 132]</sup>. The critical cracking thickness (CCT) is defined as the coating thickness above which cracks start to form. The existence of a CCT has been explained by Lange <sup>[132]</sup>. The strain energy ( $U_0$ ) stored in a crack-free coating is given by:

$$\frac{\partial U_0}{\partial V} = \frac{\sigma_t^2(1-\nu_v)}{2E_v} \quad \text{Equation 2.25}$$

where  $\sigma_t$  is the tensile stress in the coating,  $E_v$  and  $\nu_v$  are, respectively, the Young's modulus and Poisson's ratio of the coating and  $V$  is the coating volume. The strain energy of a coating containing a small crack of length  $c_c$  is:

$$U_c = U_0 - \left[ \frac{\sigma_t^2(1-\nu_v)}{2E_v} \right] Z_c c_c d_d^2 + G_c c_c d_d \quad \text{Equation 2.26}$$

where  $d_d$  is the dry coating thickness,  $G_c$  is the energy needed to form two crack surfaces per unit area (which is also known as the critical strain-energy release rate in the fracture mechanics literature) and  $Z_c$  is a dimensionless parameter which differs for different types of cracks <sup>[133]</sup>. A crack can only extend if it reduces the free energy of the system:

$$\frac{\partial U_c}{\partial c_c} = G_c d_d - Z_c d_d^2 \frac{\sigma_t^2(1-\nu_v)}{2E_v} \leq 0 \quad \text{Equation 2.27}$$

$$d_d \geq d_c = \frac{2G_c E_v}{Z_c \sigma_t^2(1-\nu_v)} \quad \text{Equation 2.28}$$

Equation 2.28 suggests that there is a critical thickness  $d_c$  (CCT) above which cracks can propagate. Though the drying rate does not affect the magnitude of the capillary pressure or the fracture resistance of a coating, it does affect the relaxation of the stress, resulting in a

lower CCT at a higher drying rate <sup>[126]</sup>. The CCT increases with the particle size due to the decrease in the capillary force (Equation 2.21) <sup>[128,129]</sup>. When cracking occurs, the crack width scales linearly with the coating thickness <sup>[134, 135]</sup>.

## §2.2 Principle of electrophoretic deposition

EPD is a colloidal method which is attracting increasing interest as a material processing technique <sup>[10-14]</sup>. EPD is usually carried out in a two electrode cell, as schematically shown in Figure 2.5.

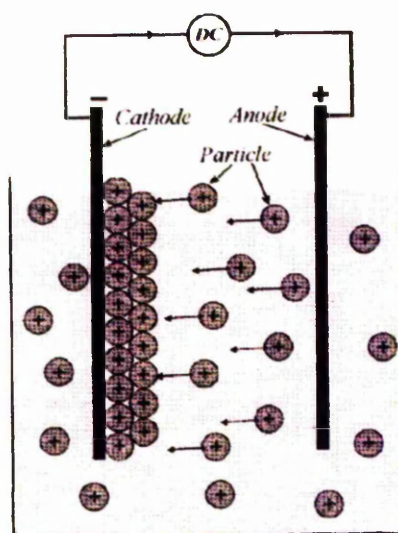


**Figure 2.5 Schematic drawing of EPD cell showing the process** <sup>[13]</sup>

EPD is a combination of two processes: electrophoresis and deposition.

- 1) Electrophoresis is the motion of charged particles in a suspension under the influence of an electric field. An Indian scientist Bose <sup>[136]</sup> discovered this phenomenon during the 1740s in a liquid-siphon experiment. In 1807, a Russian scientist Reuss first observed the electric-field-induced motion of solid particles in water <sup>[13, 14]</sup>.
- 2) Deposition is the coagulation of particles to form a dense mass. The first practical application of EPD was for ThO<sub>2</sub> and tungsten deposition on a platinum cathode as an emitter for electron tube application in 1933 by Harsanyi <sup>[137]</sup>.

In order to effectively apply EPD to process materials, it is essential to prepare a stable suspension containing charged particles that are free to move when an electric field is applied. Therefore EPD can be applied to any solid that is available as a fine powder (e.g.  $<30\mu\text{m}$  particle size) or as a colloidal suspension, including metals, polymers, ceramics and glasses. In the last 15 years, the interest in EPD as a technique to produce advanced materials has widely increased, both in the academic and the industrial sector, and since then a wide range of new applications of EPD for processing a variety of bulk materials and coatings has been reported [10-14, 138-142]. The increasing significance of EPD in materials processing follows from its high versatility for application with various materials, its cost-effectiveness, simplicity, the requirement of only basic equipment and the ability to be scaled-up to large product volumes and sizes. Moreover, compared with other processing methods based on the packing of particles, EPD is able to produce uniform deposits with high microstructural homogeneity, to provide adequate control of deposit thickness. EPD can deposit coatings on a wide range of shapes and form complex 3D structures [10-14, 138-142].

### §2.2.1 Electrophoretic mobility

The response of charged particles in suspension to an electric field can be defined as the electrophoretic mobility [143-147], which can be obtained by measuring the velocity,  $v$ , of a charged particle in the suspension under the influence of an electric field  $E_{sus}$ :

$$\mu = \frac{v}{E_{sus}} \quad \text{Equation 2.29}$$

where  $\mu$  is the electrophoretic mobility of the colloidal particles. The electrophoretic mobility of a rigid colloidal particle can be derived from the Henry equation [148-152]:

$$\mu = \frac{2\varepsilon_r\varepsilon_0\zeta}{3\eta} f(\kappa a_p) \quad \text{Equation 2.30}$$

where  $\zeta$  is the zeta potential,  $\eta$  is the viscosity of the solvent, and  $a_p$  is the particle size and  $\kappa$  is defined previously in Equation 2.10. The function  $f(\kappa a_p)$  increases from 1 for  $\kappa a_p \ll 1$  to 1.5 for  $\kappa a_p \gg 1$ . For particles that are much smaller than the Debye length ( $\kappa^{-1}$ ), the electrophoretic mobility  $\mu$  is given by Debye-Hückel formula [153].

$$\mu = \frac{2\varepsilon_r\varepsilon_0\zeta}{3\eta} \quad \text{Equation 2.31}$$

For particles that are much larger than the Debye length ( $\kappa^{-1}$ ), the electrophoretic mobility is given by Helmholtz-Smoluchowski equation <sup>[148]</sup>:

$$\mu = \frac{\varepsilon_r\varepsilon_0\zeta}{\eta} \quad \text{Equation 2.32}$$

According to Lindner <sup>[154, 155]</sup>,  $\text{NiMn}_2\text{O}_4$  particles with larger specific surface area showed higher electrophoretic mobility, and are preferentially deposited during EPD. However, no appreciable segregation effect was observed in <sup>[156]</sup>. In contrast, Negishi et al <sup>[157]</sup> observed preferential deposition of fine particles by comparing the agglomerate size distributions of particles in the suspension and the deposited particles.

### §2.2.2 EPD kinetics

An important issue of EPD is the kinetics of the deposition process. It is essential to have a description of the deposition yield during EPD of particles to fully control the deposition of coatings or bulk materials. Hamaker <sup>[147]</sup> derived an empirical equation that has proven to be a good description of the EPD process:

$$\frac{dY}{dt} = \alpha_d \mu C_{sus} E_{sus} S \quad \text{Equation 2.33}$$

where  $Y$  is the deposition yield,  $t$  is the deposition time,  $\mu$  is the electrophoretic mobility (discussed in section 2.2.1),  $C_{sus}$  is the particle concentration in the suspension,  $E_{sus}$  is the effective electric field strength in the suspension,  $S$  is the depositing area on the electrode, and  $\alpha_d$  is the factor that takes into account that not all particles brought to the electrode are incorporated in the deposit ( $\alpha_d \leq 1$ ). This equation is now accepted as describing the basis for the kinetics of electrophoretic deposition.

The deposition area of the electrodes ( $S$ ) and the concentration of particles in the suspension ( $C_{sus}$ ) can easily be determined or calculated during the process. The electrophoretic mobility ( $\mu$ ) can be measured following Equation 2.29. Although the



electric field strength in the suspension ( $E_{sus}$ ) is almost always evaluated from the applied voltage ( $E_{app}$ ) and the inter-electrode distance ( $b$ ), however, such a calculation is subject to conditions. The voltage drop over an electrophoretic deposition cell with flat equal surface area electrodes can in general be described as consisting of four terms as schematically shown in Figure 2.6 and Equation 2.34:

$$E_{app} = E_{ele1} + E_{dep} + E_{sus} + E_{ele2} \quad \text{Equation 2.34}$$

where the applied voltage  $E_{app}$  drops over four parts in the EPD cell: the voltage drop at the electrodes caused by the polarization of the electrodes,  $E_{ele1}$  and  $E_{ele2}$ ; the voltage drop caused by the suspension,  $E_{sus}$ ; and the voltage drop across the deposited layer,  $E_{dep}$ . The conditions required for the electric field strength in a suspension to be close to the applied voltage divided by the inter-electrode distance are thus: The voltage drops at each of the electrodes should be negligible, and the specific resistance of the deposit should be of the same order as the specific resistance of the suspension.

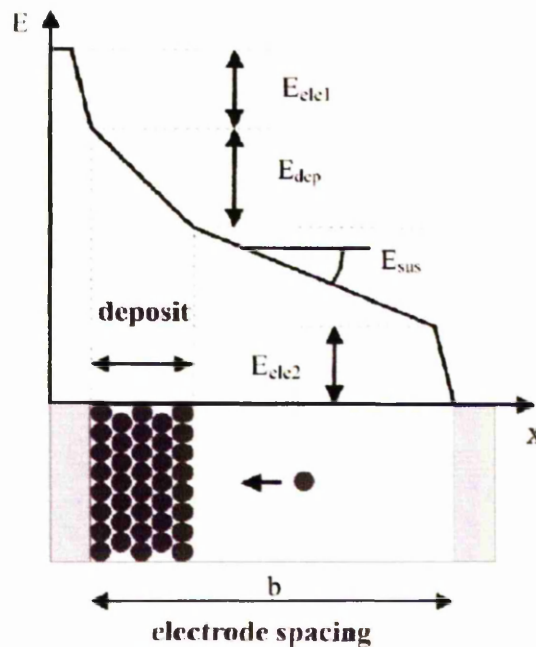


**Figure 2.6 Evolution of the voltage in an electrophoretic deposition cell: The applied voltage is consumed by a voltage drop at each electrode and by an ohmic voltage drop over the suspension and the deposit <sup>[12]</sup>**

The validity of the approximation for the electric field strength is rendered doubtful by the fact that under constant applied voltage, the current is found to decrease during EPD. The following explanations have been proposed: a change in polarization at the electrodes <sup>[147, 158]</sup>; a higher specific resistance of the deposit compared with the suspension <sup>[159-163]</sup>, and changes in the conductivity of the suspension <sup>[163]</sup>.

Starting from the electrode, it should be realized that in order for a net current to flow through the solid/liquid interface, a potential in excess of the equilibrium potential is required (activation overvoltage). Nernst's law suggested that the equilibrium potential over a solid/liquid interface depends on the concentration of the reactants <sup>[12]</sup>:

$$\Delta\phi = \Delta\phi_0 + \frac{R_g T}{zF} \ln\left(\frac{C_{ox}}{C_{red}}\right) \quad \text{Equation 2.35}$$

where  $\Delta\phi_0$  is the standard equilibrium potential drop over the solid/liquid interface,  $\Delta\phi$  is the equilibrium potential drop over the solid/liquid interface,  $C_{ox}$  is the activity of the species being oxidized,  $C_{red}$  is the activity of the species being reduced,  $R_g$  is the gas constant,  $T$  is the temperature,  $z$  is the valence of the reduction reaction, and  $F$  is Faraday's constant. If during electrophoretic deposition the transport of reactants for the electrode reaction toward the electrode is slower than the consumption at the electrode, the concentration at the electrode will drop and the concentration overvoltage will increase. Note that changes in the proton or hydroxyl concentration were expected and observed in some of the investigations into the mechanism of deposition. Moreover, the fact that a deposit forms on one of the electrodes can be expected to hinder the transport of reactants toward that electrode, thus enhancing the probability for an increase in concentration overvoltage (Figure 2.7) <sup>[12]</sup>.

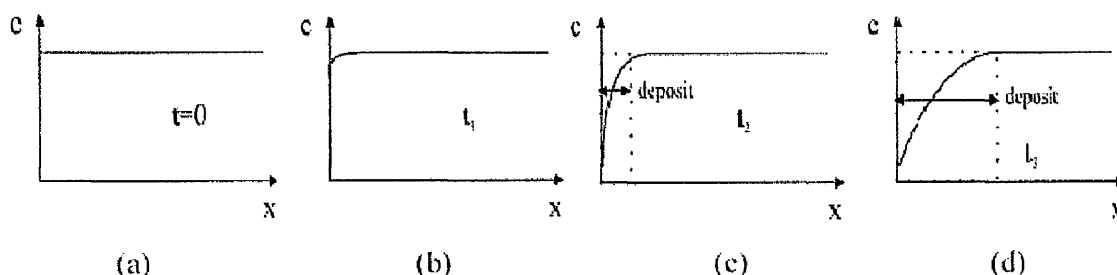


**Figure 2.7 Schematic illustration of a possible influence of the growing deposit on the concentration of the reactant for the electrode reaction as a function of the distance from the electrode <sup>[12]</sup>**

Before any potential is applied, no concentration gradients exist (Figure 2.7 (a)). As soon as a current starts to flow, the concentration of the species reacting at the electrode drops, and the amount consumed at the electrode is replaced through diffusion, convection and migration (Figure 2.7 (b)). The presence of the deposit influences the transport of reactants to the electrode, and if this results in a decreased incoming flux, the concentration at the electrode will start to drop (Figure 2.7 (c)). Because the diffusion flux is determined by the slope of the concentration gradient, the diffusion term in the flux decreases with increasing deposit thickness (Figure 2.7 (d)).

Most authors have simply inferred the higher specific resistance of the deposit from the decrease in current during EPD <sup>[159-162]</sup>. Sarkar et al <sup>[15, 16, 164-166]</sup> measured the electric field strength by measuring the potential drop between two platinum probes placed between the electrodes and also monitored the potential drop between the deposition electrode and one platinum probe in the suspension. Sarkar et al <sup>[15, 16]</sup> also observed a transient effect when the voltage was disconnected for 30 s and the experiment continued afterward: The increase in resistance had disappeared while the deposit was still on the electrode. It was only after about 30 s that the potential required for the constant applied current reached the value it had reached before the experiment was interrupted. Such a transient effect indicates that the increase in potential drop is caused by concentration overvoltage. During the time the experiment is paused, the formed concentration gradients can be relieved by diffusion, and the concentration overvoltage needs to be built up once again.

The resistance of the suspension is also not necessarily constant. Anne et al <sup>[163]</sup> modelled the conductivity of a suspension as consisting of a contribution of ions outside the double layers of the particles and a contribution by the electric charges associated with the moving particles (Figure 2.8), and the consumption of moving particles due to the deposition decreased the particle concentration in the suspension so that the conductivity of the suspension decreased.

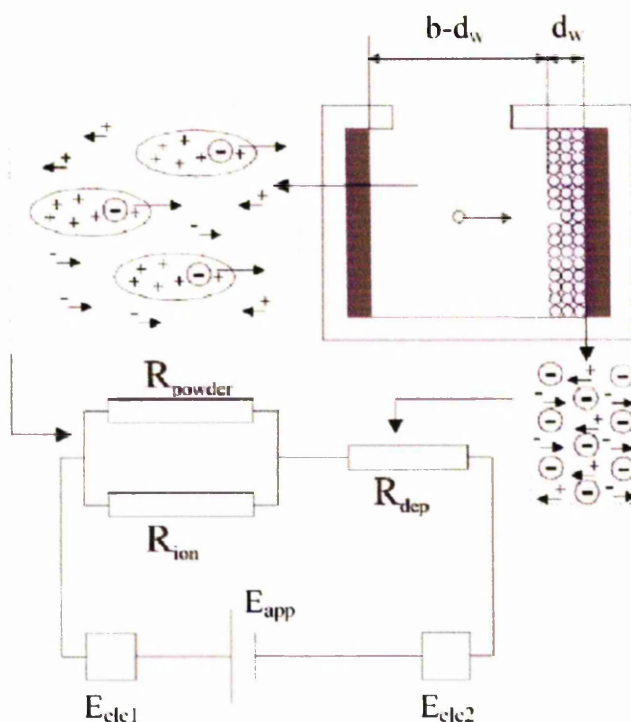


**Figure 2.8** Schematic diagram for the resistance of the EPD cell <sup>[12]</sup>

Figure 2.8 schematically models the equivalent circuit of the EPD cell. In the suspension moving ions as well as moving particles contribute to the electrical conductivity, which can be represented by two resistors ( $R_{powder}$  and  $R_{ion}$ ) in parallel. In the deposit, only ions are moving, hence it is represented by one resistance,  $R_{dep}$ , in series with the resistance of the deposit. And there is also voltage drop at each electrode ( $E_{ele1}$  and  $E_{ele2}$ ).

It should be noted that a higher specific resistance of the deposit compared with the suspension is indeed expected. In a deposit, the volume fraction of the liquid, i.e. the

effective area for ionic conductance, is lower than in the suspension <sup>[167]</sup>.

### §2.2.3 Deposit formation mechanisms

Despite numerous advantages of the EPD technique and a large range of applications achieved, there is need for further theoretical and experimental work to gain an understanding of the mechanism, especially on the linkage of the parameters of the EPD process to the final deposit properties.

The mechanisms of EPD have been discussed in numerous publications <sup>[13, 23, 168-171]</sup>. Up to now, the proposed mechanisms can be divided into four categories: particle accumulation, charge-neutralisation or electrocoagulation,  $\zeta$ -potential lowering or electrochemical coagulation, and electrical double layer distortion and thinning.

- 1) Particle accumulation: Hamaker and Verwey <sup>[147, 168]</sup> observed similarities between the formation of deposits by electrophoresis and gravitation. In fact, in both processes, the pressure exerted by the arriving particles enables the particles close to the deposit to overcome the inter-particle repulsion and form a deposit. Therefore the primary function of the applied electric field in EPD is to move the particles towards the electrode to accumulate. This mechanism can also explain the deposition of coatings onto membranes that do not serve as electrodes.
- 2) Particle charge neutralization: Grillon et al. <sup>[169]</sup> suggested that the charged particles are neutralized when they touch the electrode. This mechanism explains the deposition of single particles and monolayers and the deposition of powders charged by the addition of salts to the suspension as shown experimentally by Brown and Salt <sup>[170]</sup>. However this mechanism cannot explain deposition carried out for longer times, or for processes in which the particle-electrode contact is not permitted, e.g. when the deposition occurs on a semi-permeable membrane placed between the electrodes.
- 3) Electrochemical coagulation: This mechanism implies the reduction of the repulsive forces between the particles in suspension. Koelmans <sup>[23]</sup> calculated the rise of the ionic strength close to the electrode when a difference of potential was applied. This

behaviour was due to an increase in the electrolyte concentration around the particles. He discovered that the value of ionic strength was similar to that required to flocculate a suspension, so he proposed a mechanism based on the fact that an increase of the electrolyte concentration produces a decrease in the repulsion between the particles close to the electrode (lower  $\zeta$ -potential) and consequently the particles coagulate. Considering that a finite time is needed for the increase of the electrolyte concentration next to the electrode, it can be concluded that a certain time has to pass in order to have deposition. This time is inversely proportional to the square of the applied voltage, i.e. the higher the applied potential the shorter the time required for deposition. This mechanism is plausible when the electrode reactions generate  $\text{OH}^-$  ions, e.g., suspensions containing water, but it is invalid when there is no increase of electrolyte concentration near the electrode.

- 4) Electrical double layer distortion and thinning: Sarkar and Nicholson <sup>[13]</sup> proposed a mechanism based on the distortion of the particle double layer to explain the invalidation of the electrochemical coagulation mechanism when there is no increase of ion concentration near the electrode. They found that when a positive particle and its shear layer are moving towards the cathode, the double layer is distorted (thinner ahead and wider behind), as shown in Figure 2.9, due to fluid dynamics and the effect of the applied electric field. As a result the counter ions in the extended tail experience a smaller coulombic attraction to the positively charged particle and can more easily react with other cations moving towards the cathode. This process reduces the thickness of the double layer and therefore, when another particle with a thin double layer is approaching, the two particles may come close enough to interact through attractive London-vdW force and coagulate. This mechanism is plausible considering a high concentration of particles is expected close to the electrode (or high collision frequency). This mechanism works also for incoming particles with thin double layer heads, coagulating with particles already in the deposit.

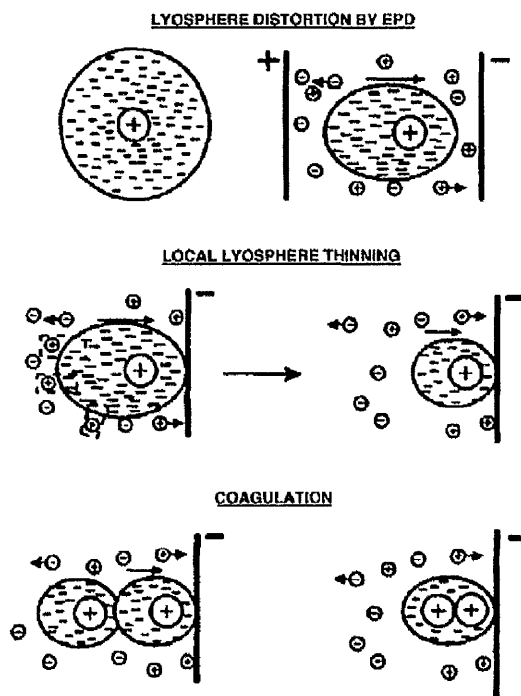


**Figure 2.9 Schematic representation of the deposition mechanism due to electrical double layer distortion and thinning<sup>[13]</sup>**

Subsequently Fukada et al.<sup>[171]</sup> proposed a new theory based on a decrease of the concentration of  $H^+$  near the cathode due to particle discharge or other chemical reactions. Therefore the local pH increases towards the isoelectric point (IEP),  $\zeta$ -potential decreases and the particles coagulate. This mechanism applies to all suspensions containing hydrogen ions.

#### **§2.2.4 Aggregation of deposited particles during EPD**

Studies of electrodynamic particle aggregation during EPD have been carried out under steady and alternating electric fields. Experimental observation of clustering of colloidal particles deposited near an electrode in a DC electric field is also reported by many researchers and explained by considering convection due to electro-osmotic flow<sup>[27-30, 172-182]</sup>. Numerical simulations have also been employed to a limited extent to model the accumulation of charged particles on an electrode during EPD<sup>[173, 174]</sup>. Ristenpart et al.<sup>[176, 177]</sup> have recently studied, both theoretically and experimentally, the flow around a charged spherical colloid next to an electrode in order to understand the nature of long-range

particle-particle attraction near the electrodes, which is schematically shown in Figure 2.10.

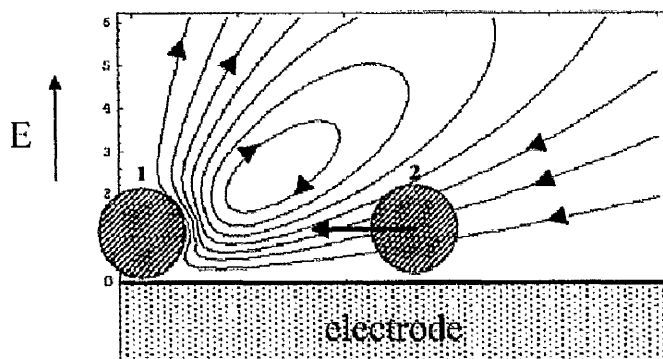


**Figure 2.10 Schematic illustration of the electro-osmotic flow around a spherical charged particle <sup>[27]</sup>**

Assuming particle-1 is fixed on the electrode and the local electric field around the particle is distorted by the presence of the surface charge of particle-1 together with its diffuse double-layer. The electro-osmotic flow around particle-1 is proportional to the strength of the electric field near particle-1 ( $E_{dep}$ ) and the  $\zeta$ -potential ( $\zeta$ ) of particle-1. The velocity of the electro-osmotic flow ( $u$ ) is expressed <sup>[182]</sup>:

$$u = \frac{\epsilon_r \epsilon_0 \zeta}{\eta} E_{dep} \quad \text{Equation 2.36}$$

where  $\epsilon_r$  and  $\epsilon_0$  are respectively the relative dielectric constant of solvent and the dielectric permittivity of the vacuum, and  $\eta$  is the viscosity of the solvent. If there is another particle (particle-2) in the electro-osmotic flow around the fixed particle-1, particle-2 will be dragged toward particle-1 by the electro-osmotic flow and form an aggregate. The aggregate formation rate is proportional to the electric field strength and the  $\zeta$ -potential of particle-1. The aggregates can be re-dispersed by an electric field with reversed direction <sup>[172, 175-179]</sup>.

### §2.2.5 Remarks on EPD of advanced materials

The EPD process has gained considerable interest in recent years for fabrication of advanced materials. The process is a simple, easy to use and cost-effective method of



deposition, which finds innumerable applications including thin and thick films <sup>[15, 183]</sup>, layered ceramics <sup>[184-188]</sup>, hybrid materials <sup>[189, 190]</sup>, fiber reinforced composites <sup>[191, 192]</sup> as well as nano-composites <sup>[193]</sup>, nano-scale assembly of 2-D and 3-D ordered structures and micro-patterned coatings <sup>[21, 22, 194-196]</sup>. Although the mechanisms are still not completely clear, the possibility of deposition on both conducting and non-conducting substrates opens up a range of applications including gas separation sensors <sup>[197, 198]</sup>, solid oxide fuel cells <sup>[199-203]</sup>, thermal barrier coatings <sup>[25, 26, 204]</sup> etc. However, further researches, i.e., how the electro-osmosis mechanism applies on thick (multi-layer) EPD coatings, how important the wet particle packing is on the final structure after drying and sintering, and are there any specific particle packing conditions which benefit the following drying and sintering processes, are still required into fundamental understanding on mechanisms of particle packing during EPD for practical applications.

### **§2.3 Sintering of colloidal ceramic coatings**

Sintering is a process on bonding of particles by molecular or atomic attraction in a solid state by the application of heat, causing strengthening of a powder mass and possibly resulting in densification and re-crystallization by transport of materials. From another point of view, sintering can be treated as a diffusional creep under the action of capillary forces <sup>[205]</sup>.

When a coating bonded to a rigid substrate is sintered, the shrinkage only occurs in the thickness direction, whereas the in-plane contractions are constrained by substrates. Tensile stresses arise and reduce the sintering potential of the coating, resulting in a high porosity <sup>[206]</sup> and can lead to warping <sup>[207]</sup>, cracking or even delamination <sup>[52-54]</sup>. It is thus imperative to understand the densification behaviour and stress development during the constrained sintering of ceramic coatings <sup>[52-54, 208, 209]</sup>.

#### **§2.3.1 Mechanisms of sintering**

During sintering, the temperature of the ceramic compact is raised sufficiently so that various mass-transport mechanisms begin to operate. Diffusion of atoms and molecules can take place along the particle surfaces or through the bulk of particles. Evaporation and

condensation of molecules can also occur. The net result is that molecular bridges between the particles are established. Necks are formed between particles and begin to grow in size. Note that the surface area of the merged object is less than that of the two starting particles, so the surface energy is decreased. As the ceramic is sintered, the pores, which were initially percolated to form a connected network, become smaller and fewer in number, and eventually become isolated from each other. The ceramic undergoes densification. Grain growth occurs at elevated temperatures but may be blocked by the presence of the pores [205].

During a sintering process of porous compacts of ceramics, the pores initially present can change shape, becoming channels or isolated spheres, without necessarily changing in size. More commonly, however, both the size and shape of the pores present change during the firing process, the pores becoming more spherical in shape and smaller in size as sintering continues (Figure 2.11) [205].

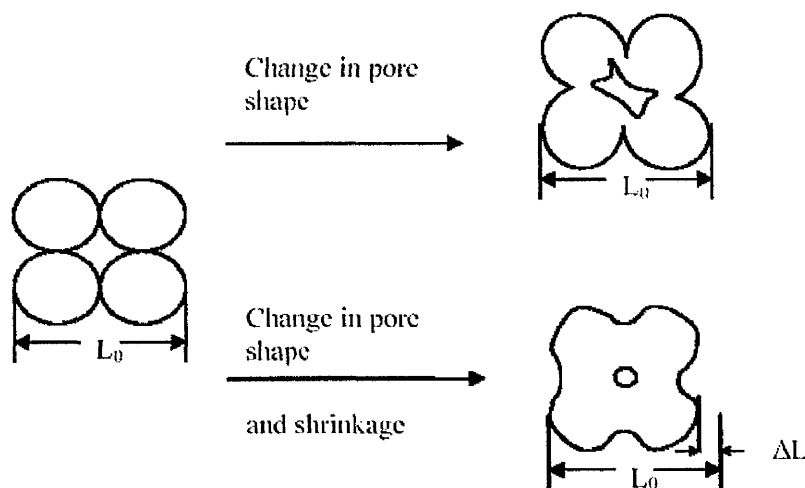


**Figure 2.11 Schematic drawing of sintering of particle compacts with only changes in pore shape, and with both changes in pore shape and shrinkage** [205]

The free-energy change that gives rise to densification is the decrease in surface area and lowering of the surface free energy by the elimination of solid-vapour interfaces. The material transfer is affected by the vapour pressure difference and changes in free energy across a curved surface. This usually takes place with the coincidental formation of new but lower-energy solid-solid interfaces. The intrinsic sintering stress,  $\sigma_s$ , can be expressed in

terms of the surface energy,  $\gamma_{sv}$ , of pores and the grain boundary energy,  $\gamma_{gb}$ ,<sup>[210, 211]</sup>.

$$\sigma_s = \frac{2\gamma_{sv}}{r_p} + \frac{2\gamma_{gb}}{a_g} \quad \text{Equation 2.37}$$

where  $r_p$  and  $a_g$  are, respectively, the radius of curvature of pores and grain size. If the particle size, and consequently the radius of pore curvature, is small, sintering stress may be of a substantial magnitude (Equation 2.37). They become large when the radius of curvature is less than a few microns. This is one of the major reasons why much ceramic technology is based on and depends on the use of fine-particle materials.

Since the driving force (surface energy) is the same in all systems, considerable differences in behaviour in various types of systems must be related to different mechanisms of material transfer. Mechanisms for mass transport during sintering are listed in Table 2.2.

**Table 2.2 Mechanisms for mass transport during sintering<sup>[48]</sup>**

Mechanism	Transport Path	Source of Matter	Sink of Matter	Densification
Surface diffusion	Surface diffusion	Surface	Neck	No
	Lattice diffusion	Surface	Neck	No
Evaporation-condensation	Vapour transport	Surface	Neck	No
Boundary diffusion	Boundary diffusion	Grain boundary	Neck	Yes
Lattice diffusion	Lattice diffusion	Grain boundary	Neck	Yes
	Lattice diffusion	Dislocations	Neck	Yes

Surface diffusion is a general transport mechanism that can produce surface smoothing, particle joining, and pore rounding, but it does not produce volume shrinkage. In materials where the vapour pressure is relatively high, sublimation and vapour transport to surfaces of lower vapour pressure also produce these effects. Diffusion along the grain boundaries and diffusion through the lattice of the grains produce both neck growth and volume

shrinkage.

### §2.3.2 Sintering stages

For sintering of ceramic compacts, to help understand the sintering process, three stages of densification have been described, i.e. the initial, the intermediate, and the final stage. The microstructural observations in each stage are listed in Table 2.3:

**Table 2.3 Microstructural changes observed in the initial, intermediate and final stages during sintering of ceramic compacts <sup>[48]</sup>**

Stage	Observations
Initial	Particle surface smoothing and rounding of pores Grain boundaries form, neck formation and growth Rounding of interconnected, open pores Homogenization of segregated materials by diffusion Small porosity decreases (<12%)
Intermediate	Shrinkage of open pores intersecting grain boundaries Mean porosity decreases significantly Slow grain growth
Final	Closed pores (density>92%) Closed pores intersect grain boundaries Pores shrink to a limited size or disappear Pores larger than the grains shrink relatively slowly.

The initial stage of sintering <sup>[212-214]</sup> is frequently referred to as the neck formation stage. The sintering driving force for the initial particle compact is the curvature difference between the particle surface and that of the particle contacts.

The intermediate stage of sintering <sup>[215-218]</sup> begins after grain and pore shape changes caused during the initial stage. At this stage, the pore shape approximates a continuous cylindrical channel. The cylindrical pore and grain-boundary matrix consisting of equilibrium dihedral angles formed on the solid-vapour (pore) surfaces at the intersections with the solid-solid (grain-boundary) interfaces. During the intermediate stage, the cylindrical pore shrinks.

During the final stage <sup>[216]</sup>, the removal of closed pores takes place. The densification is dependent on the association of pores with grain boundaries and the rate of grain growth.

### §2.3.3 Sintering kinetics

Since the introduction of a mathematical model for sintering by Kuczynski <sup>[219, 220]</sup> numerous other models have been proposed. Reviews of these sintering kinetic models are given in <sup>[221-223]</sup>.

#### §2.3.3.1 Sintering shrinkage

The bulk shrinkage during sintering has been extensively discussed in classic books <sup>[31, 48, 59, 205]</sup>. For solid state sintering, the linear shrinkage ( $\Delta L/L_0$ ), as shown in Figure 2.11, is given by:

$$\frac{\Delta L}{L_0} = \left( \frac{KD^* \gamma_{sv} \Omega t}{k_b T a_p^n} \right)^m \quad \text{Equation 2.38}$$

where  $T$  is the sintering temperature,  $a_p$  is the particle size,  $K$  and  $k_b$  are the geometry-dependant constant and the Boltzmann constant respectively,  $\Omega$  is the atomic volume of the diffusion vacancy,  $D^*$  is the exponential temperature-dependent  $[\exp(-E_{act}/k_b T)]$  mass diffusion coefficient ( $E_{act}$  is the activation energy for diffusion),  $\gamma_{sv}$  is the surface energy of the particle, and  $m$  and  $n$  are constants that depend on the mechanisms of mass transport, i.e.  $n=2$  for volume diffusion <sup>[213]</sup>,  $n=3$  for grain-boundary diffusion <sup>[224]</sup>, and  $m$  is commonly in the range 0.3-0.5. This equation indicates that temperature is the most critical factor for the initial sintering shrinkage due to its exponential function to the diffusion coefficient. From the equation, it can be also found that smaller particles packed identically, i.e. at similar particle packing densities, will produce more shrinkage in equivalent time.

#### §2.3.3.2 Effect of particle packing on sintering kinetics

It is commonly accepted that the green density has a great influence on densification. For green compacts of same particles, high green density was found to be easily densified due to short-distance mass diffusion <sup>[34, 225, 226]</sup>.

Furnas <sup>[227, 228]</sup> was the first to suggest that the pores in a framework of large connected particles could be filled with smaller particles. His model assumed that the fine agglomerates are small enough to enter the voids formed by the larger agglomerates. Later, numerous studies were reported on the use of mixtures of particle sizes to increase the bulk density of powder compacts <sup>[35-39]</sup>. McGeary <sup>[38]</sup> found that the maximum particle packing density is achieved when the size ratio (large/small) is greater than 7 and the smaller particles are dispersed uniformly. Hellmig <sup>[35]</sup> introduced a model to describe the maximum packing density of trimodal and bimodal powder mixtures and applied the model to  $\text{Al}_2\text{O}_3$  powder mixtures with a large difference in mean particle size with the smaller components being nano-powders. Studies of the packing efficiency to achieve high density have led to widespread use of mixed particle sizes in practical ceramics systems <sup>[39]</sup>.

Compared with uniform small powders, mixtures have higher green densities and less shrinkage during sintering. The presence of large particles can provide a control for achieving sintered bodies with a specific level of porosity <sup>[36]</sup>. In mixtures of large and small particles, intermediate sintering rates were observed where a weighted average particle size could be assigned to characterize the behaviour of the mixture <sup>[229]</sup>. Large particles, which are performing as rigid inclusions in a compact during sintering, inhibit shrinkage among small particles <sup>[209]</sup>. From Kuczynski's model <sup>[230]</sup> for the sintering of a single particle to a flat plane, it may be deduced that sintering between the small and large particles occurs more rapidly than sintering between large particles alone. It is envisioned that, after some shrinkage, a tensile stress will arise on the boundaries of small particles with large particles, whereas a compressive stress will be generated on the contacts between larger particles, due to the different densification rates between small-small, small-large and large-large particles. Thus, the large particles will inhibit continued shrinkage between the mixed-pair contacts, and the presence of the small particles will enhance the sintering rate on the contacts between large particles. An intermediate shrinkage rate, not predictable from either size alone, is expected, unless the smaller particles tear away from one or more of the adjacent larger particles. O'Hara <sup>[229]</sup> experimentally confirmed that the coarse particle may constrain the sintering shrinkage rate of surrounding fine particles. They isothermally sintered bimodal mixtures of coarse alumina particles (16, 33, and 66  $\mu\text{m}$  average grain size) and various fractions of fine particles (3 to 6  $\mu\text{m}$ ) at 1500°C for up to 28

min. Examining only the initial stage of sintering, they observed that the maximum linear shrinkage occurred for mixtures with 80 to 100% of the fine component. To explain their results, they suggested that micro-stresses developed because of differential shrinkage in the compact. They found that this stress retardation effect occurs at low temperatures and short sintering times, whereas, at higher temperatures and longer times, the effect vanishes because of stress relief through creep and cracking. Coble <sup>[231]</sup> theoretically verified that these stresses can arise due to the sintering of fine-to-coarse particles. However, the stress may either enhance or reduce the sintering process, depending on geometric considerations. Evans <sup>[232]</sup> found that microstructural defects (e.g., cracks) may develop as a result of the stresses developed at non-uniformities in packing, such as at a collection of fine particles sintering adjacent a large particle.

#### §2.3.4 Constrained sintering of ceramic coatings

Constrained sintering can be defined as a process in which the sintering behaviour of a ceramic body is retarded because of some constraint. The constraint may be either internal to the body, as in the case of a ceramic matrix containing dense parts, or external to it, as in the case of a particulate coating attached to a rigid substrate. If the coating remains attached to the substrate during sintering, and does not crack, shrinkage can occur only in the direction perpendicular to the plane of the substrate and the substrate exerts a tensile stress on the coating at the interface. The strain rates in the presence of stresses are <sup>[54]</sup>:

$$\dot{\epsilon}_i = \dot{\epsilon}_f + \frac{1}{E_v}(\sigma_i - \nu_v \sigma_j - \nu_v \sigma_k) \quad \text{Equation 2.39}$$

$$E_v = \frac{3\eta\rho}{3-2\rho} \quad \text{Equation 2.40}$$

$$\nu_v = \frac{1}{2} \left( \frac{\rho}{3-2\rho} \right)^{1/2} \quad \text{Equation 2.41}$$

where  $\dot{\epsilon}_i$  is the strain rate in the  $i$  direction and  $\dot{\epsilon}_f$  is the unconstrained strain rate,  $E_v$  and  $\nu_v$  are, respectively, the uniaxial viscosity and viscous Poisson's ratio of the porous material, which are both dependent on the compact density  $\rho$  (Equations 2.40 and

2.41). For sintering of ceramic coatings on rigid substrate there is not an external load besides the tensile stress,  $\sigma_t$ , so it follows that:

$$\sigma_z = 0 \quad \text{Equation 2.42}$$

$$\sigma_x = \sigma_y = \sigma_t \quad \text{Equation 2.43}$$

$$\dot{\epsilon}_x = \dot{\epsilon}_y = 0 \quad \text{Equation 2.44}$$

where the  $z$  direction is perpendicular to the substrate (thickness direction). Substituting  $\sigma_x$ ,  $\sigma_y$ ,  $\sigma_z$ ,  $\dot{\epsilon}_x$ , and  $\dot{\epsilon}_y$  into Equation 2.37:

$$\sigma_t = -\frac{E_v}{1-\nu_v} \dot{\epsilon}_f \quad \text{Equation 2.45}$$

$$\dot{\epsilon}_z = \dot{\epsilon}_f - \frac{2\nu_v \sigma_t}{E_v} = \frac{1+2\nu_v}{1-\nu_v} \dot{\epsilon}_f \quad \text{Equation 2.46}$$

By analogy to the elastic behaviour, two viscous contents, i.e. the shear viscosity  $G_v$  and the bulk viscosity  $K_v$ , are defined as:

$$G_v = \frac{E_v}{2(1+\nu_v)} \quad \text{Equation 2.47}$$

$$K_v = \frac{E_v}{3(1-2\nu_v)} \quad \text{Equation 2.48}$$

The viscosity of a porous sintering body is proportional to the power of 2 or 3 of the grain size, depending on the prevalent diffusion mechanism <sup>[233-236]</sup>.

Because the sintering mechanism is not changed by the tensile stress:

$$\frac{2}{3} \sigma_t = K_v (\dot{\epsilon}_z - 3\dot{\epsilon}_f) = K_v \dot{\epsilon}_f \frac{2\nu_v - 1}{1 - \nu_v} \quad \text{Equation 2.49}$$

Due to the existence of the tensile stress, the actual sintering stress,  $\sigma'_s$ , is decreased by:

$$\sigma'_s = \sigma_s - \frac{2}{3} \sigma_t \quad \text{Equation 2.50}$$



Calata et al. <sup>[237]</sup> sintered a cordierite glass – ceramic layer on silicon plates and observed the appearance of very large pores near the interface coating/substrate, which decreases the local density. They attributed this result to the combined effect of the geometrical constraint as well as the poor wetting of the substrate by the glass. Investigating gold circuit pastes, Choe et al. <sup>[238]</sup> could not differentiate free from constrained sintered films by means of grain size measurements, so that the observed densification retardation could not be explained by the grain coarsening argument.

Guillon and coworkers <sup>[46, 239]</sup> studied pore orientations in constrained sintered coatings and revealed that pores tend to be aligned along the thickness direction. The proposed explanation is that the constraining stress modifies the diffusional fluxes and inhibits the neck growth in the plane. Pores thus have a non-spherical geometry, and a preferential orientation is induced, leading to anisotropic viscous properties such as uniaxial viscosities or Poisson's ratios <sup>[240]</sup>. As soon as grain growth takes place, the anisotropic pores and the uniaxial viscosities should then affect the grain morphology <sup>[46]</sup>.

Because the tensile stress can be released by shear deformation <sup>[236, 241]</sup>, the magnitude of the tensile stress is dependent on the ratio ( $\beta$ ) of the shear rate,  $\dot{\epsilon}_s$ , to the densification rate,  $\dot{\epsilon}_z$  <sup>[213]</sup>.

$$\beta = \frac{\dot{\epsilon}_s}{\dot{\epsilon}_z} \quad \text{Equation 2.51}$$

$$\dot{\epsilon}_s \propto \frac{D_l^*}{a_p^2} \quad \text{Equation 2.52}$$

$$\dot{\epsilon}_z \propto \frac{\delta_{gb} D_{gb}^*}{a_p^3} \quad \text{Equation 2.53}$$

$$\beta \propto \frac{a_p}{\delta_{gb}} \exp\left(-\frac{\Delta E_{act}}{R_g T}\right) \quad \text{Equation 2.54}$$

where  $a_p$  is the particle size,  $D_l^*$  is the lattice diffusion coefficient,  $D_{gb}^*$  is the grain boundary diffusion coefficient,  $\delta_{gb}$  is the grain boundary width,  $\Delta E_{act}$  is the difference in activation energy between boundary diffusion and lattice diffusion. Equation 2.54 predicts

that a larger particle size and a higher temperature would increase  $\beta$ . However, a larger particle size would decrease the sintering potential according to Equation 2.37.

The constrained sintering of coatings on rigid substrates not only leads to a reduction in the sintering stress (Equation 2.50), but also leads to processing flaws, i.e. cracks and delamination. Damage during constrained sintering typically begins in the early stages of densification and near pre-existing defects <sup>[242, 243]</sup>. It can be in the form of macroscopic cracks, diffuse damage, or a combination of the two. This problem has been theoretically analyzed <sup>[208, 244, 245]</sup>. Garino and Bowen <sup>[244, 245]</sup> showed the importance of increasing the inter-particle-neck size before densification to avoid cracking, whereas Bordia and Jagota <sup>[52]</sup> found that the friction between coating and substrate, crack length as well as coating thickness play an important role in crack extension. The crack evolution during sintering follows the same rules of crack development in the drying stages (Equations 2.26-2.28) and is affected by the coating thickness, interfacial traction and pre-existing cracks <sup>[52]</sup>. The critical cracking thickness (CCT), above which cracks grow during sintering, is given by:

$$d_s \geq d_c = \frac{2G_c E_v}{Z_c \sigma_i^2 (1 - \nu_v)} \quad \text{Equation 2.55}$$

where  $d_s$  and  $d_c$  are respectively the thickness of the sintered coating and the CCT of the coating, and as defined in previous section,  $G_c$  is the energy needed to form two crack surfaces per unit area, and  $Z_c$  is a dimensionless parameter related to the crack types. Substituting  $\sigma_i$  in Equation 2.45 to Equation 2.55 gives:

$$d_s \geq d_c = \frac{2G_c (1 - \nu_v)}{Z_c E_v \dot{\epsilon}_f^2} \quad \text{Equation 2.56}$$

## §2.4 Summary

This chapter gives an overview of the colloidal processing of ceramics. To achieve the optimal microstructure for a given application, it is essential to control interparticle forces, and consolidation, drying and sintering behaviours during the entire processing. EPD, as a consolidation technique in the colloidal processing, is fundamentally reviewed on its

## Chapter 2-Literature Review

---

kinetics, mechanisms and applications. The packing behaviour of particles in the EPD deposit, especially in thick deposit, is an arisen direction which needs further researches not only for understanding the deposit formation process in EPD but also for tailoring microstructures of EPD products. The solid-state sintering of ceramic compacts is briefly reviewed. The sintering mechanisms, microstructural developments and kinetics are discussed. In addition, for the fabrication of ceramic coatings, the phenomena and factors which need to be considered in constrained sintering, have also been introduced.

## **Chapter 3 Experimental Procedure and Characterisation Methods**

### **§3.1 Preparation of suspensions**

#### **§3.1.1 Raw materials and preparation procedure**

Commercial 8mol% YO<sub>1.5</sub> stabilized Zirconia (YSZ) particles (99%+, Pi-KEM, Shropshire, UK) with various sizes, which were prepared by the supplier by comminution of synthesized fully stabilized cubic YSZ bulk materials followed by sieving to obtain specific sizes, were employed as raw particles. The dispersing solvent used as the media of suspensions was acetylacetone (2,4-pentanedione, 99%+, Sigma Aldrich Co Ltd.). The suspension was prepared as follows: a certain amount ( $5.0 \times 10^{-4}$ - $1.0 \times 10^{-2}$ kg) of YSZ particles was dispersed in  $4.0 \times 10^{-5}$ m<sup>3</sup> acetylacetone in a glass beaker ( $5.0 \times 10^{-5}$ m<sup>3</sup>), followed by 300s of ultrasonication using an ultrasonic probe (22.5 kHz, MICROSON™, Ultrasonic Cell Disruptor). The particle concentration in a suspension was varied in the range of 12.5-250kg/m<sup>3</sup> (volume concentration 0.21%-4.13%). In the study of effect of suspension electrical conductivity, a small amount ( $1.0 \times 10^{-8}$ - $2.0 \times 10^{-7}$ m<sup>3</sup>) of iodine alcohol (20kg/m<sup>3</sup>) was added into suspensions before the ultrasonic treatment, and the iodine content in the suspension was controlled in the range of 0-0.1kg/m<sup>3</sup>.

#### **§3.1.2 Centrifuge treatment**

Centrifuge treatment was used to separate particles with broad size distributions.  $3.0 \times 10^{-5}$ m<sup>3</sup> of prepared suspension with certain particle concentration (50kg/m<sup>3</sup>) was centrifuged for 120s at the speed of 800-2000 revolutions per minute (rpm). Particles with relative large sizes were settled down to the bottom and small particles stayed in the suspension, so that the original suspension was separated into two groups of suspensions which had relatively narrow particle size distributions.

### **§3.1.3 Attrition milling treatment**

An attrition miller (01HD, Szegvari Attritor System, Union Process) was employed for some specific experiments to break severe agglomerates in the suspensions. A  $7.5 \times 10^{-4} \text{m}^3$ -capacity milling tank was loaded with 0.02kg of particles, 0.8kg of tetragonal zirconia polycrystalline (TZP) milling balls (diameter of  $3.0 \times 10^{-3} \text{m}$ ), and  $2.0 \times 10^{-4} \text{m}^3$  of acetylacetone. The rotation speed of the stirring arm of the attrition miller was 550 rpm while cooling water was used to keep the milling tank at a constant temperature. Suspensions with certain particle concentrations were prepared by dilution of the milled mixture with pure acetylacetone followed by 300s of ultrasonication.

## **§3.2 Characterisation of particles and suspensions**

### **§3.2.1 Particle size, shape and surface morphology determination**

A field emission gun scanning electron microscopy (FEG-SEM, Philips XL-30, Eindhoven, Netherlands) was used to check the primary particle sizes and the shapes and surface morphologies of YSZ particles used in the study. To make samples for SEM observations, the particles were ultrasonically dispersed in ethanol and a small drop of the resulting suspension was placed on an aluminium stub polished to mirror smooth. The samples were carbon-coated in vacuum before used for SEM observations.

### **§3.2.2 Agglomerate sizes determination**

The hydrodynamic diameter of the YSZ particles was measured using a Malvern Mastersizer (Micro Trac X100, Worcestershire, UK) particle size analyzer with a minimum detectable size of 50nm. Acetylacetone was used as the dispersant in the agglomerate size analysis. The refractive indices of YSZ and acetylacetone were set as 2.15 and 1.45 respectively in the measurement. By this method, agglomerated particles will be regarded as one big particle so it is a good index of the particle agglomeration in suspension. Ultrasonic treatments were carried out for 300 seconds before the agglomerate size measurements. Also treatments of mechanical dispersion, i.e. the suspension was mechanical stirred for up to 900s at 240 rpm, and treatments of sedimentation of

suspensions for up to 3600s were carried out for specific samples before the agglomerate size measurements as comparisons to the ultrasonic treatment.

### **§3.2.3 Zeta potential measurement**

The zeta potential of the particles in the suspension was measured by a Doppler electrophoretic light scattering method using a zeta potential analyzer (Beckman, Coulter DELSA 440SX, Miami, Fl, USA). To measure the zeta potential, the suspensions need to be diluted using pure solvent, acetylacetone in this study. For suspensions with the addition of iodine for the electrical conductivity study, the solvent, used to dilute the suspension for the zeta-potential measurement, was adjusted to the same electrical conductivity as the suspension by adding iodine.

### **§3.2.4 Other characterisations**

The specific surface area of the YSZ particles was determined using a Brunauer-Emmett-Teller (BET) adsorption analyser (COULTER SA 3100<sup>TM</sup> Series Surface Area and Pore Size analyzer) with nitrogen as adsorbant.

The electrical conductivity of freshly-prepared suspensions was measured by an electrical conductivity meter (METTLER-TOLEDO InLab 737, Columbus, OH, USA).

## **§3.3 Fabrication of EPD green coatings**

As-prepared fresh suspensions were employed in the deposition experiments, which were carried out using an EPD setup, as schematically shown in Figure 3.1. A platinum sheet was used as the anode and a Fecralloy substrate (1mm thick, Fe72.8/Cr22/Al5/Y0.1/Zr0.1, GoodFellow, Cambridgeshire, UK) which had been polished down to 1 $\mu$ m was used as the cathode. The two electrodes were set parallel to each other with a fixed separation distance of  $1.0 \times 10^{-2}$ m, between which a voltage was applied in the range of 15-480V. Sedimentation of YSZ particles was prevented by mild stirring (120 rpm) using a magnetic bead stirrer. The deposition time was varied from 30s to 1200s.

To investigate the effect of an electric field on the particle-packing condition of an as-deposit EPD wet coating, a 2-step experiment was designed. In the first step, a coating was prepared by EPD following the above procedures. After deposition, the two electrodes with the deposit on the substrate electrode were taken out of the suspension, and put immediately into another beaker containing pure acetylacetone. A voltage in the range of 0-250V was applied between the two electrodes for a certain time (60-1200s). This second step carried out in pure acetylacetone is referred to as a 'densification' process later. A standard resistor (499 $\Omega$ ) and a voltage meter were connected into the EPD circuit to detect the current flow during both EPD and the densification. The coated substrate was then removed from the solvent and dried in an ambient environment, and the green coating was obtained.

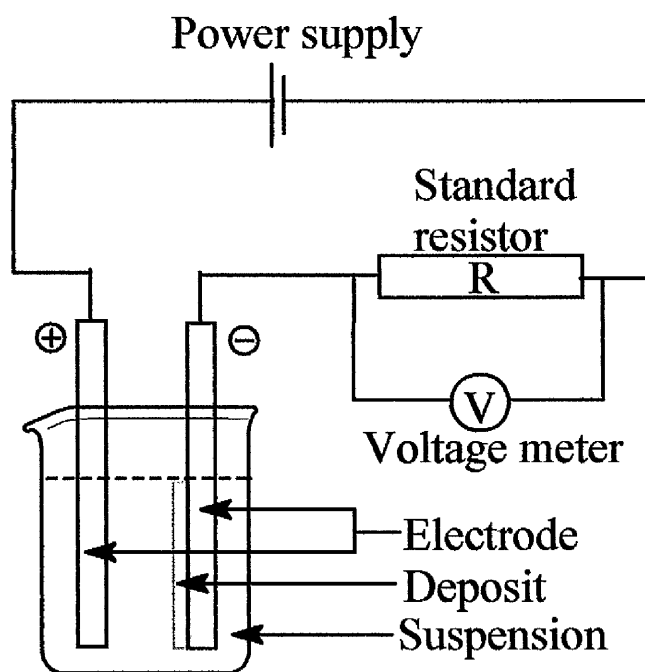


**Figure 3.1 Schematic diagram of the electrophoretic deposition apparatus.**

### §3.4 Characterisation of EPD deposits

#### §3.4.1 Characterisation of wet coatings

The particle packing density of an as-deposited wet EPD coating was defined as the volume occupation ratio of solid particles in the wet coating. The masses of the wet coating and the dry coating were measured respectively by a balance (Ohaus AB-S, Leicester, UK). And the particle packing density of the wet coating,  $\rho_w$ , was calculated from the equation below:

$$\rho_w = \frac{\frac{m_d}{\rho_{YSZ}}}{\frac{m_w - m_d}{\rho_{AcAc}} + \frac{m_d}{\rho_{YSZ}}} \quad \text{Equation 3.1}$$

where  $m_d$  and  $m_w$  are respectively the mass of wet coating and dry coating, and  $\rho_{YSZ}$  and  $\rho_{AcAc}$  are the theoretical density of fully dense YSZ ( $6.05 \times 10^3 \text{ kg/m}^3$ ) and pure acetylacetone ( $0.98 \times 10^3 \text{ kg/m}^3$ ) respectively.

The thickness of a wet deposit  $d_w$  was defined as below:

$$d_w = \frac{\frac{m_w - m_d}{\rho_{AcAc}} + \frac{m_d}{\rho_{YSZ}}}{S} \quad \text{Equation 3.2}$$

where  $S$  is the deposit area which was measured and calculated by analyzing (Image tool, UTHSCSA) the image of the top coating taken by an optical microscope (Olympus BH, Tokyo, Japan).

The thickness shrinkage  $\delta$  during drying was defined:

$$\delta = \frac{d_w - d_d}{d_w} \quad \text{Equation 3.3}$$

where  $d_d$  is the dry coating thickness measured by a magnetic thickness gauge ( $\pm 2 \mu\text{m}$ ), and the thickness values were also confirmed by using of SEM.



### §3.4.2 Characterisation of green coatings

Green density  $\rho_d$  was measured and calculated from a mass and volume method:

$$\rho_d = \frac{m_d}{S \cdot d_d} \quad \text{Equation 3.4}$$

where  $m_d$ ,  $d_d$  are the mass and thickness of the green coating respectively, and  $S$  is the deposit area, the measurement of all these values were the same as stated previously. The green densities were obtained from taking the average value of ten coatings fabricated under identical conditions. The results are reproducible ( $\pm 3\%$ ).

The microstructure of the green coating was observed using SEM from both the top surface and the fractured cross section. The fracture surfaces were obtained by removing the green coating from the substrate using a razor to crack off the coating along the substrate, by doing which the microstructure of the coating was kept unaffected, and the peeled off coatings were referred as free standing coatings.

Since green EPD coatings are too fragile to take further tests to investigate their microstructures and particle packing conditions, it is essential for them to gain strength from sintering.

### §3.5 Sintering of EPD deposits

Green coatings were sintered isothermally at certain temperatures ranging from 1000°C to 1300°C, with the sintering time from 2 hours to 40 hours and with a heating and cooling rate of 3K·minute<sup>-1</sup>.

For the studies on the kinetics of sintering of EPD coatings and for examining the particle packing conditions of EPD coatings, free standing coatings were sintered without the constraint of substrates. And also experiments on constrained sintering with coatings on FeCrAlloy substrates were carried out to investigate the effects of substrates on properties of EPD coatings.

### §3.6 Characterisation of sintered EPD deposits

#### §3.6.1 Measurement of densities of sintered deposits

It is difficult to measure the density of a free standing coating because the free standing coating was in fairly small pieces with random shapes, which induce inaccuracy in mass measurement and volume measurement of the small piece. The density of the green coating was measured before removing it (for obtaining free standing samples) from the substrate using the method described previously. Two top-view images of a specific free standing piece were recorded by the optical microscope both before and after sintering. By image analysis of the two pictures taken from the identical piece of coating using the Image Tool, the shrinkage (linear/area) ratio during sintering were obtained. The thickness shrinkage ratio due to sintering was calculated from the measured value of both green coating thickness  $d_d$  and freely sintered coating thickness  $d_{fs}$  using the thickness gauge. With knowing the green density,  $\rho_d$ , and the shrinkage ratio, the free standing sintered density  $\rho_{fs}$  can be calculated from the following equation:

$$\rho_{fs} = \frac{\rho_d}{\left(1 - \frac{\Delta L}{L_0}\right)^2 \left(\frac{d_{fs}}{d_d}\right)} \quad \text{Equation 3.5}$$

where  $\Delta L/L_0$  is the linear shrinkage ratio during sintering measured from the image analysis of the top-view pictures.

For constrained sintering, the coating can only perform shrinkage along the thickness direction, so the constrained sintered density  $\rho_{cs}$  can be calculated from the equation:

$$\rho_{cs} = \frac{\rho_d}{\frac{d_{cs}}{d_d}} \quad \text{Equation 3.6}$$

where  $d_{cs}$  is the thickness of the constrained sintered coating measured by the thickness gauge.

### §3.6.2 Characterisation of microstructures

The microstructures of sintered coatings were observed from both the fracture cross-sections and the top surfaces using SEM.

The pore structure of coatings was measured using a mercury intrusion porosimetry technique (Quantachrome Poremaster, Hook, UK) which is based on the premise that non-wetting mercury can only be intruded into pores under pressure. The pore size distribution of free-standing coatings was measured with an applied intrusion pressure up to 50000psi ( $3.45 \times 10^8$ Pa). The surface tension of mercury and the contact angle of mercury to YSZ were set as 480dyn/cm and  $140^\circ$  respectively in the measurement. Both the open porosity and the pore size distribution could be measured using the mercury intrusion method. For the constrained sintered coatings, the substrates were removed by polishing followed by a chemical dissolution with a mixture of HCl and HNO<sub>3</sub>. The top coatings obtained were washed thoroughly using deionised water and dried in an oven at 100°C for over night before carrying out the mercury intrusion test.

### §3.6.3 Mechanical hardness

A Micro-indentation (Wilson Instruments, Norwood, USA), which has a diamond Vickers indenter, was employed to test the mechanical hardness of sintered coatings. The test was performed in two steps: 1) the Vickers indenter was first forced into the polished cross section, or top surface for some specific samples, of a sintered coating using a fixed load force 0.98 Newton (100gram-force); 2) the length of the diagonals of the resulting indent was measured and the Micro-hardness was calculated as the applied load,  $P$ , over the surface area of the indentation:

$$HV = \frac{1.85F}{d^2} \quad \text{Equation 3.7}$$

where  $F$  is the applied force and  $d$  is the average diagonal length of the indentation and is measured in millimetre (mm). For each specimen, 15-20 independent indentations were performed and the average value was used.

## Chapter 4 Particle Packing Mechanism during EPD

### §4.1 Introduction

The microstructure of EPD coatings was mostly studied after drying. EPD of micrometer latex particles has been investigated *in-situ* by Bohmer <sup>[181]</sup> who observed using optical microscopy that the particles deposited on an electrode aggregated to form large ordered clusters in a D.C. electric field and that the deposit peeled off from the electrode when the direction of the electric field was reversed. Such aggregation phenomena during EPD could be explained by a hydrodynamic model which is based on the electro-osmotic flow around deposited particles as schematically shown in Figure 4.1 <sup>[27-30]</sup>.

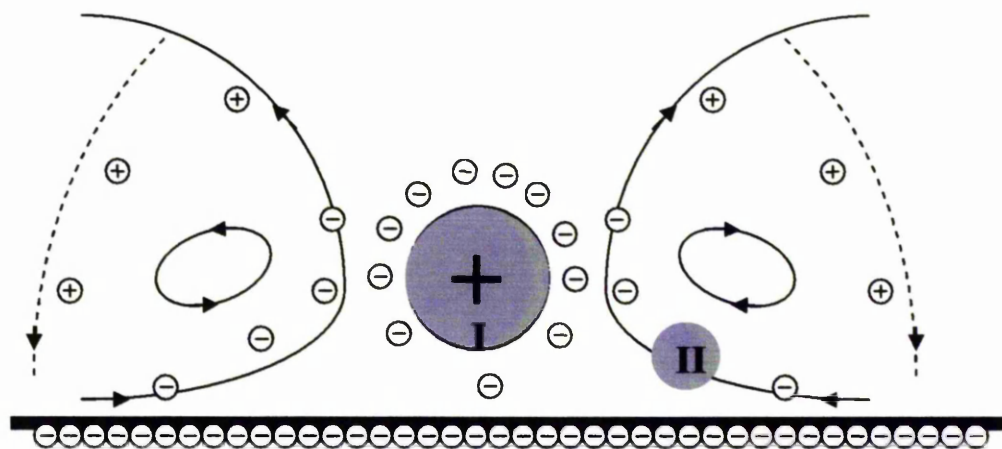


**Figure 4.1 Schematic drawing of the electro-osmotic flow around a positively charged particle.**

Up to now, although a number of theoretical <sup>[148, 242, 243]</sup> and experimental works <sup>[160, 244]</sup> investigated the deposition kinetics, very few studies have been carried out to investigate the packing mechanisms of EPD particles. Therefore, it is essential to determine the relationship between deposition parameters and the particle packing density of the EPD deposit.

In this chapter, the deposit weight was recorded to investigate the deposition kinetics. The wet packing density was found to be controlled by deposition time, applied voltage, and the

electrical conductivity and particle concentration of the suspension. When an as-deposited wet coating was immersed in a pure acetylacetone solvent under a D.C electric field, the wet packing density increased. The results are consistent with the rearrangement of particles by electro-osmotic flow. The rearrangement ability of particles was proportional to the strength of the local electric field in the deposit.

### §4.2 Results

#### §4.2.1 Characterisation on suspensions

Figure 4.2 shows the SEM image of the raw YSZ particles used in this chapter. By image analyzing the picture, the average primary particle size was evaluated as approximate  $(0.16 \pm 0.04) \mu\text{m}$ , and slight agglomerates with sizes around  $(0.7 \pm 0.2) \mu\text{m}$  (as highlighted in red circles) can also be found in the particles. Smooth surfaces and like spherical shapes were the features of the particles, which can be identified from the image.

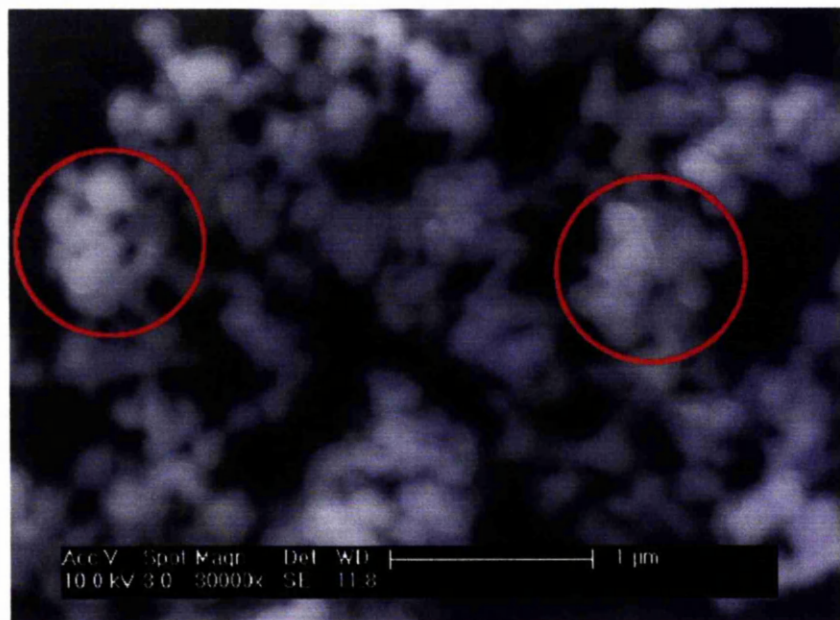


**Figure 4.2 SEM images of the submicrometre YSZ particles**  
(Red circles marking typical agglomerates)

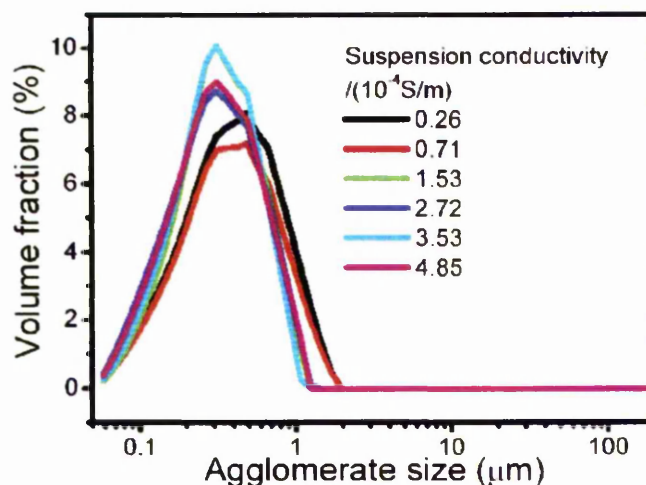


**Figure 4.3 Agglomerate size distributions as a function of electrical conductivities of suspensions**

For the interest of investigating effects of the electrical conductivity of suspensions on the EPD process, i.e. the particle packing during deposition, iodine was added to the suspension to adjust the suspension electrical conductivity. Figure 4.3 shows the particle agglomerating conditions in suspensions with various electrical conductivities. It can be found that the agglomerate sizes slightly decreased from the increasing of the suspension electrical conductivity. By considering the average agglomerate size, there was a significant agglomerate size decrease from  $0.49 \mu\text{m}$  to  $0.31 \mu\text{m}$  when the electrical conductivity of the suspension was increased from  $0.71$  to  $1.53 (\times 10^{-4} \text{ S/m})$ . For further increasing the electrical conductivity from  $1.53$  to  $4.85 (\times 10^{-4} \text{ S/m})$ , the agglomerate sizes kept almost unaffected. The particle agglomeration was directly controlled by the particle  $\zeta$ -potential, so the  $\zeta$ -potentials of particles and the electrical conductivities of suspensions were measured as a function of the iodine concentration and the plots were shown in Figure 4.4.



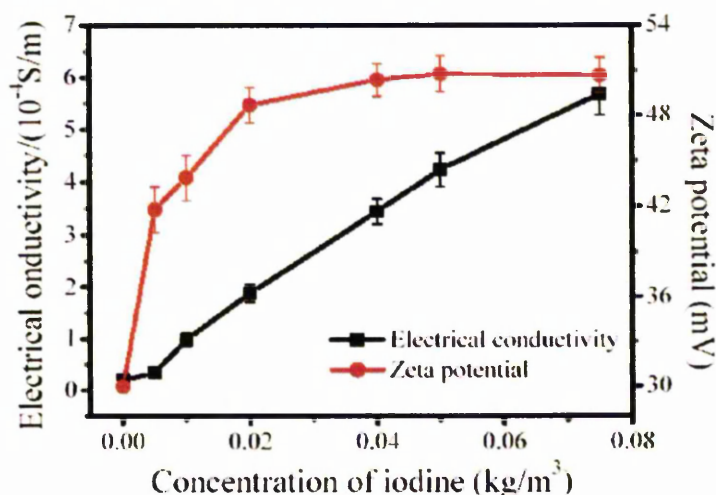


**Figure 4.4 Electrical conductivity and  $\zeta$ -potential as a function of iodine content (the particle concentration of the suspension is lower than  $2.5 \times 10^{-2} \text{ kg/m}^3$ ).**

Figure 4.4 shows both the  $\zeta$ -potential and the electrical conductivity as a function of the iodine content in a suspension with a solid concentration lower than  $2.5 \times 10^{-2} \text{ kg/m}^3$ . In pure acetylacetone, the  $\zeta$ -potential of particles was measured to be around +30mV, which was much higher than the data (near zero) reported before [245, 246]. This may be due to different chemical and surface properties of the particles used in this work from that of previous researches. In previous studies, various methods, such as adding iodine to suspensions [245, 246], attrition milling [247] or using mixture of organic solvents [26], were used to increase the  $\zeta$ -potential of particles and prepare stable suspensions. In the present study, the commercially obtained YSZ particles could be well dispersed in pure acetylacetone due to the high  $\zeta$ -potential (+30mV). With the addition of iodine, the  $\zeta$ -potential of particles first increases, and then maintains a constant value around +50mV when the iodine concentration is above  $0.4 \text{ kg/m}^3$ . In addition, the electrical conductivity of the suspension increases linearly with the amount of the iodine added. The  $\zeta$ -potential measurements also revealed the reason for the agglomerate size change. When the electrical conductivity increased to  $1.53 \times 10^{-4} \text{ S/m}$ , the  $\zeta$ -potential increased and the agglomerate size decreased. The agglomerate size was maintained at a certain size for the suspension with an electrical conductivity as high as  $4.85 \times 10^{-4} \text{ S/m}$  was also attributed to the  $\zeta$ -potential remaining almost the same in the range of suspension conductivity.

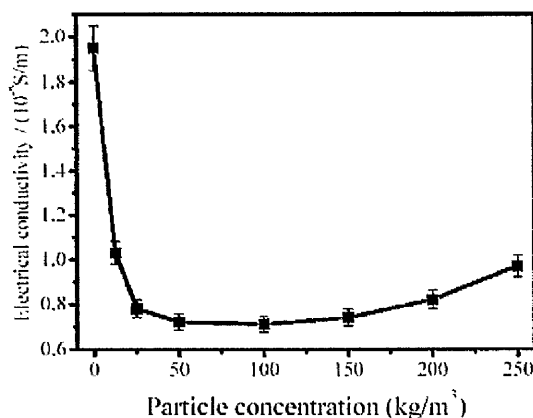


**Figure 4.5 Suspension electrical conductivity as a function of particle concentration**

It was found that the particle concentration in the suspension also altered the electrical conductivity of the suspension, though the effect showed much less significant than iodine. Figure 4.5 shows the suspension electrical conductivity as a function of the particle concentration. The electrical conductivity of pure acetylacetone was measured to be around  $1.9 \times 10^{-5} \text{ S/m}$ . With initial addition of particles, the electrical conductivity of the suspension decreased significantly. When the particle concentration reached the range of  $50\text{--}100 \text{ kg/m}^3$ , the electrical conductivity of the suspension is constant at  $7.0 \times 10^{-6} \text{ S/m}$ . Thereafter, the electrical conductivity of the suspension increases slightly with the particle concentration from  $150 \text{ kg/m}^3$  to  $250 \text{ kg/m}^3$ .

#### §4.2.2 Deposition kinetics

To investigate the effect of deposition conditions on deposition kinetics, only one parameter was changed while the others were kept constant for each set of experiments. Since YSZ particles could be well dispersed and suspended, with  $\sim 30 \text{ mV}$   $\zeta$ -potential in the suspension (Figure 4.4), in pure acetylacetone, deposition experiments were carried out without addition of iodine for the investigations on the function of deposition time, applied voltage and particle concentration. Iodine was only used in experiments carried out to investigate the function of the electrical conductivity of suspensions, which could be easily adjusted by the addition of iodine according to the relation showed in Figure 4.4.



## Chapter 4- Particle Packing Mechanism during EPD

The deposition kinetics of YSZ particles were characterized as functions of deposition conditions by measuring the deposit weight and the deposition rate/efficiency. The deposit weight was normalized by the deposition area, so it was presented in the unit of  $\text{kg}\cdot\text{m}^{-2}$ . The deposition rate was defined as the weight of particles (kg, measured after drying) deposited per unit area ( $\text{m}^2$ ) per second (s), in the unit of  $\text{kg}\cdot\text{m}^{-2}\cdot\text{s}^{-1}$ . The deposition efficiency was defined as the deposition rate ( $\text{kg}\cdot\text{m}^{-2}\cdot\text{s}^{-1}$ ) normalized by the applied voltage (V) and the particle concentration in the suspension ( $\text{kg}\cdot\text{m}^{-3}$ ), i.e. deposition efficiency ( $\text{m}\cdot\text{s}^{-1}\cdot\text{V}^{-1}$ ) = [deposition rate ( $\text{kg}\cdot\text{m}^{-2}\cdot\text{s}^{-1}$ )] / [applied voltage (V)  $\times$  particle concentration ( $\text{kg}\cdot\text{m}^{-3}$ )]. The results were summarized in Figure 4.6, which showed the effects of EPD conditions on the deposition kinetics.

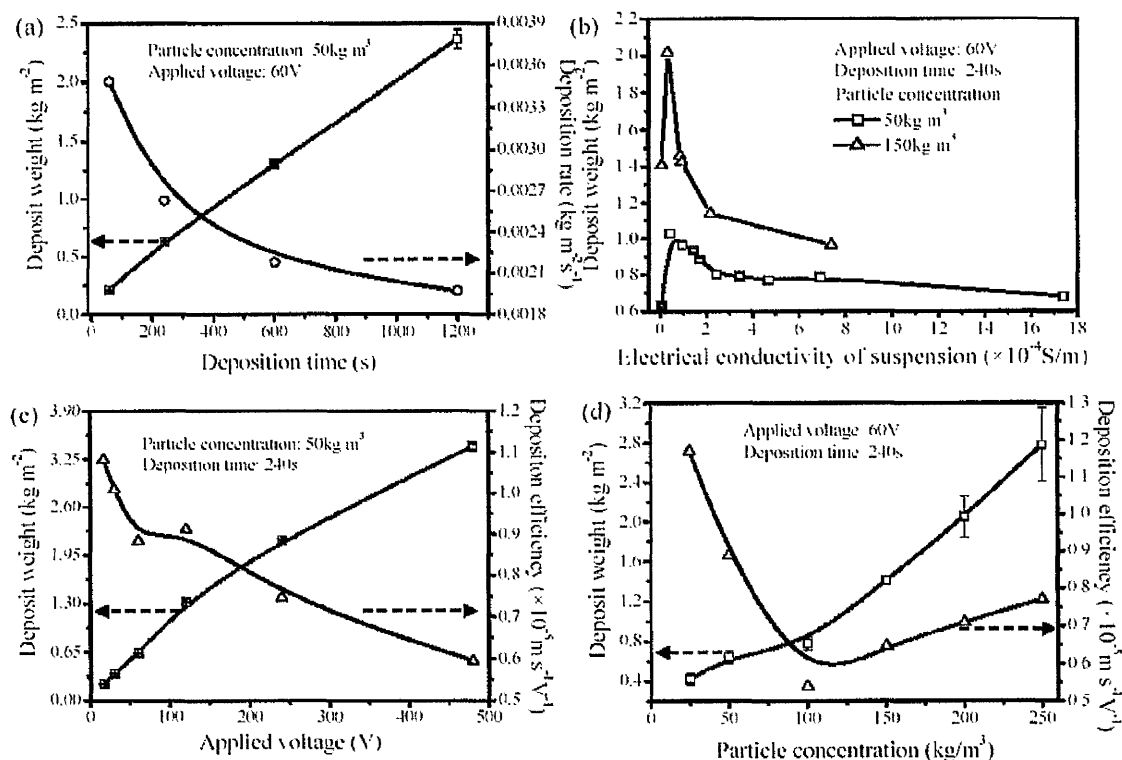


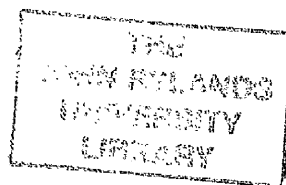
**Figure 4.6 Both deposit weight and deposition rate/efficiency as a function of (a) deposition time, (b) electrical conductivity of suspensions, (c) applied voltage and (d) particle concentration in the suspension.**

Consistent with the expression of EPD kinetics reported by Hamaker <sup>[147]</sup>, the deposit weight increased with an increase in the deposition time (Figure 4.6 (a)), applied voltage

(Figure 4.6 (c)) and particle concentration (Figure 4.6 (d)). In addition, with an increase in the electrical conductivity of the suspension, the deposit weight increased initially, and reached a maximum at the electrical conductivity of  $4.7 \times 10^{-5} \text{ S/m}$  and  $3.4 \times 10^{-5} \text{ S/m}$ , respectively, for the suspensions with  $50 \text{ kg/m}^3$  and  $150 \text{ kg/m}^3$  particle concentration, thereafter decreases (Figure 4.6 (b)). The deposition rate/efficiency decreased with the increase in the deposition time (Figure 4.6 (a)) and applied voltage (Figure 4.6 (c)). As the particle concentration increased, the deposition efficiency decreased first to a minimum at the particle concentration of  $100 \text{ kg/m}^3$ , and then increased slightly (Figure 4.6 (d)). It is worth to point out that at least five samples were repeated for each experimental condition. The relative errors were smaller than 5% for most experiments, representing good reproducibility. Big relative errors in the range of 15-20% were observed when the particle concentration was higher than  $150 \text{ kg/m}^3$ , which might be due to the instability of suspensions with high particle concentration. In addition, it was noticed that when the applied voltage was higher than 240V, the coating surface became rougher observed using optical microscope due to unstable current density. To prepare uniform coatings, an applied voltage of 60V was mainly used in this study.

### §4.2.3 Wet packing density

The most direct product fabricated from EPD was a wet coating on the substrate, so it would be worth plotting the wet coating density as functions of EPD conditions to figure out the effects of EPD conditions on particle packing during deposition. The wet coating density was defined as the volume occupation ratio of particles in the wet deposit, which can be worked out from Equation 3.1 by measuring both the mass of dry particles in the coating and the mass of solvent (acetylacetone) in the wet coating. The wet coating density also can be used to evaluate the average distance between deposited particles, which reflected the particle packing condition in the wet coating.



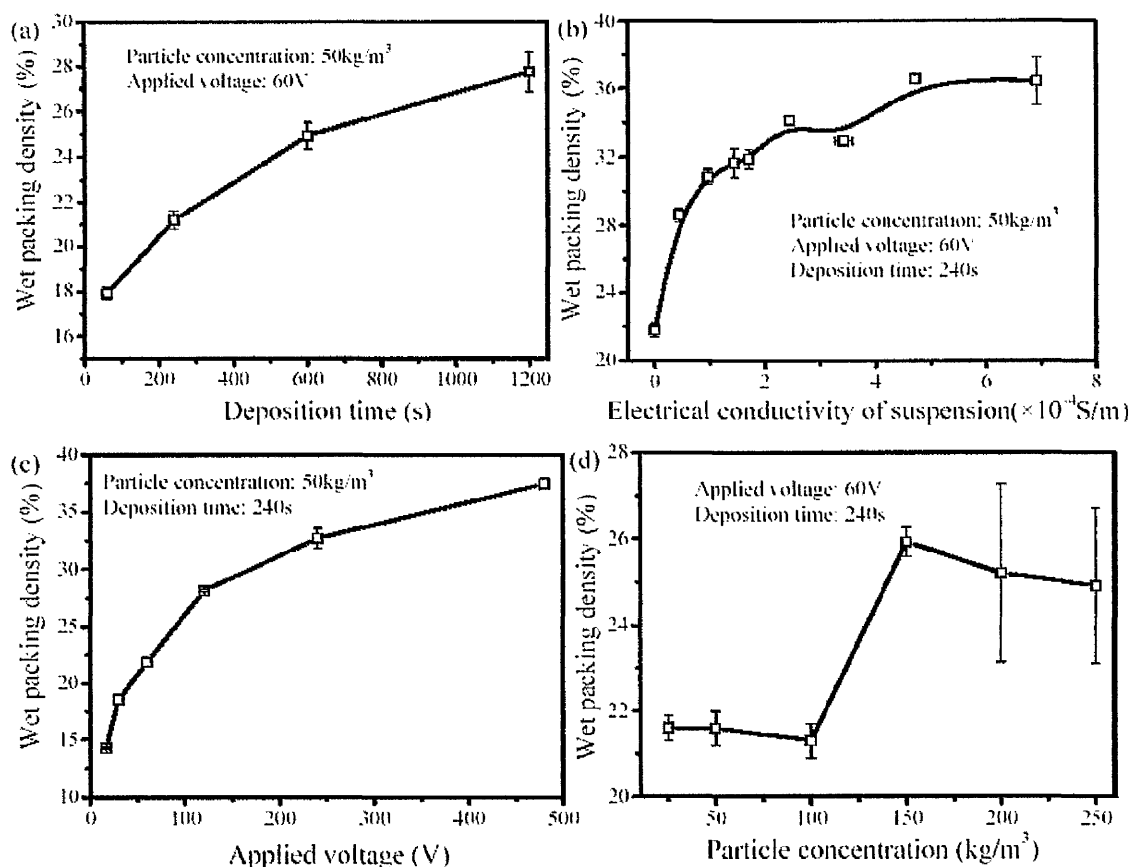
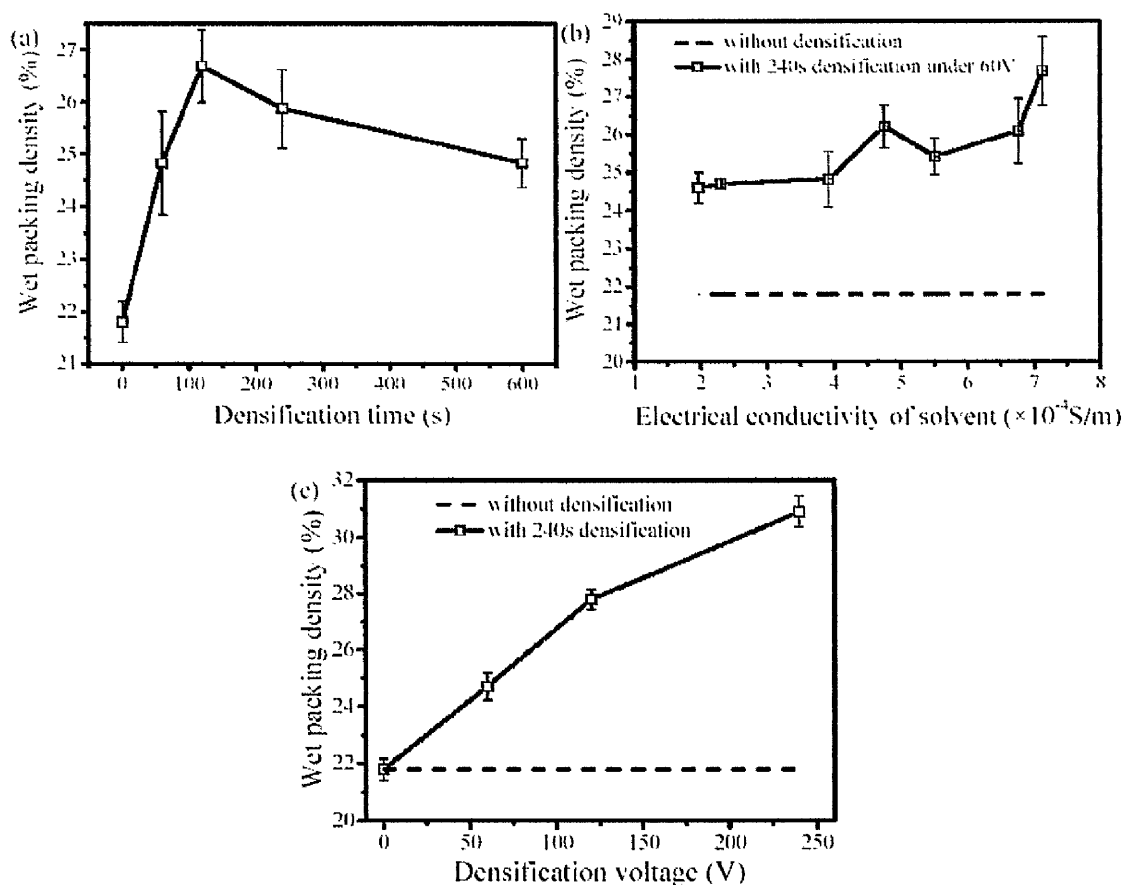


**Figure 4.7 Wet packing density i.e. volume occupation of particles in a wet coating as a function of (a) deposition time, (b) electrical conductivity of suspensions, (c) applied voltage and (d) particle concentration in the suspension.**

Figure 4.7 shows the wet coating density as a function of various deposition parameters. With an increase in the deposition time (Figure 4.7 (a)), electrical conductivity of the suspension (Figure 4.7 (b)) and the applied voltage (Figure 4.7 (c)), the wet coating density increased significantly. The particle concentration showed less obvious effect on the wet coating density (Figure 4.7 (d)). In general, the wet coating density remained constant in the particle concentration range of 25-100 kg/m<sup>3</sup>, and reached a maximum at the particle concentration of 150 kg/m<sup>3</sup>, thereafter, decreased slightly with the particle concentration. Again, bigger relative errors were observed when the particle concentration was higher than 150 kg/m<sup>3</sup> (Figure 4.7 (d)), which implied relatively unstable suspensions for those with high solids concentrations.

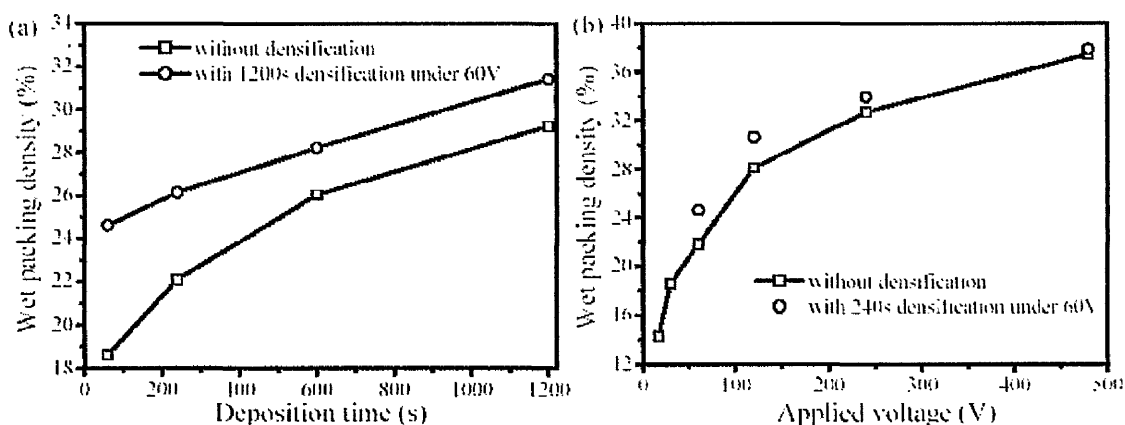
## §4.2.4 Electric field densification

EPD conditions showed direct effects on the particle packing density of wet coatings, but it was still difficult to work out a clear picture on the particle packing mechanism during the deposition because the increase of the wet coating density caused by the EPD conditions was also accompanied by the increase of both coating thickness and deposit weight. So to completely single out the effect of EPD parameters on the particle packing conditions of wet coatings, a two-step EPD was designed to examine the effect of an electric field applied on the wet EPD coating without further deposition of particles to the deposited coating. The detailed experimental procedure for this two-step EPD was explained in Chapter 3.



**Figure 4.8 Effect of the electric field densification process on the wet packing density: (a) densification time; (b) electrical conductivity of solvent; (c) densification voltage. (For all densification processes, a deposit was first prepared by EPD using the following parameters, particle concentration= $50 \text{ kg/m}^3$ , applied voltage= $60 \text{ V}$ , deposition time= $240 \text{ s}$ ,  $\text{I}_2$  content= $0 \text{ kg/m}^3$ .)**

Figure 4.8 shows the effect of the application time of the electric field, the electrical conductivity of the acetylacetone solvent and the applied voltage on the wet packing density of coatings which was prepared using EPD with the following parameters: particle concentration= $50\text{kg/m}^3$ , applied voltage= $60\text{V}$ , deposition time= $240\text{s}$ ,  $\text{I}_2$  content= $0\text{kg/m}^3$ . For a given voltage of  $60\text{V}$ , as time increases, the wet packing density increased first, and reached a maximum value after  $120\text{s}$  densification, and then decreased slightly with the time (Figure 4.8 (a)). After  $240\text{s}$  densification in an electric field of  $60\text{V}$ , the wet coating density increased with an increase in the electrical conductivity of the solvent (Figure 4.8 (b)). And as the applied voltage increased from  $0\text{V}$  to  $240\text{V}$ , the wet coating density increased from  $22\%$  to  $31\%$  (Figure 4.8 (c)).



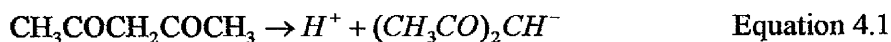
**Figure 4.9 Effect of the electric field densification process on the wet packing density of coatings which were prepared (a) with different deposition times, and (b) under different applied voltages.**

Figure 4.9 shows the effect of the densification process on the wet packing densities of coatings produced at different EPD conditions. It appeared that the increase in the wet coating density was more significant in the coatings with lower densities which were prepared with a shorter deposition time (Figure 4.9 (a)) or under a lower applied voltage (Figure 4.9 (b)).

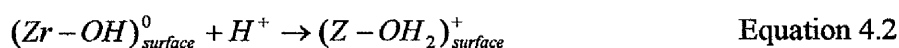
### §4.3 Discussion

#### §4.3.1 Suspension properties

The  $\zeta$ -potential measurement shows that YSZ particles are positively charged in pure acetylacetone (+30mV, Figure 4.4), which can be explained as follows. In this study, the specific surface area of particles was measured to be  $5.8 \times 10^3 \text{ m}^2/\text{kg}$ , which can adsorb hydroxyl groups from moisture in air or residual water in acetylacetone and form amphoteric hydroxyl groups of  $(\text{Zr-OH})^0$ . Acetylacetone,  $\text{CH}_3\text{COCH}_2\text{COCH}_3$ , has an acidic proton due to the two  $\text{C}=\text{O}$  functional groups and is a weak acid. It can be ionized to produce free ions of  $\text{H}^+$  and  $(\text{CH}_3\text{CO})_2\text{CH}^-$ , which leads to the high electrical conductivity of pure acetylacetone ( $1.9 \times 10^{-5} \text{ S/m}$ , Figure 4.5).



When YSZ particles are added into acetylacetone,  $\text{H}^+$  ions are adsorbed to the surfaces of particles, resulting in a positive  $\zeta$ -potential (Figure 4.4) and a decrease in the content of free ions in acetylacetone.



In an electric field, both free ions and charged particles work as current carriers. In comparison with charged particles, ions have a much higher mobility. Therefore, the electrical conductivity of a suspension decreases significantly with the particle addition due to the adsorption of free  $\text{H}^+$  ions to the particle surfaces (Figure 4.5). The adsorption of  $\text{H}^+$  ions to the particle surface shifts the equilibrium of Equation 4.1 to the right side, i.e. an increase in the  $(\text{CH}_3\text{CO})_2\text{CH}^-$  concentration. Therefore, with further addition of particles, the generation of  $(\text{CH}_3\text{CO})_2\text{CH}^-$  due to more absorption of  $\text{H}^+$  ions at more YSZ surfaces leads to a slight increase in electrical conductivity of the suspension when the particle concentration is higher than  $150 \text{ kg/m}^3$  (Figure 4.5).

When iodine is added to acetylacetone, the following reaction occurs and releases  $H^+$  ions [153].



More  $H^+$  ions can be adsorbed to particle surfaces, resulting in an increase in the  $\zeta$  - potential with an increase in the iodine content (Figure 4.4). When particle surfaces are saturated with  $H^+$  ions, excess of  $H^+$  ions will compress the electric double layer of the particles, resulting in a constant  $\zeta$  -potential when the iodine content increased from  $4.0 \times 10^{-2} \text{kg/m}^3$  to  $8.0 \times 10^{-2} \text{kg/m}^3$  (Figure 4.4). Since the electrical conductivity of suspensions depends on the content of charge carriers, the reaction between acetylacetone and  $I_2$  which produces  $H^+$  ions as charge carriers induces a linear increase in the electrical conductivity of the suspension with the iodine content (Figure 4.4).

It should also be noted that the  $H^+$  ion adsorption at particle surfaces in pure acetylacetone is not saturated. As more particles are added to acetylacetone, the charge density of  $H^+$  ions at a particle surface is expected to decrease, resulting in a decrease in the  $\zeta$  -potential. In deposition experiments, big relative errors were observed for the suspensions with a particle concentration higher than  $150 \text{kg/m}^3$  (Figure 4.6 (d) and Figure 4.7 (d)), suggesting that thick suspensions are not stable. When  $6.25 \times 10^{-2} \text{kg/m}^3$  iodine was added to the suspension with a particle concentration of  $250 \text{kg/m}^3$ , the relative error of the deposit weight decreased from 18% to 7%, suggesting that the lower  $\zeta$  -potential resulting from a lower surface-charge density led to the instability of suspensions without the presence of iodine.

#### §4.3.2 Deposition kinetics

The yield of deposition is well described by Hamaker's equation [147]:

$$M = \int_0^t \alpha_d S C_{sus} \mu E_{sus} dt \quad \text{Equation 4.4}$$

$$\mu = \frac{2 \varepsilon_r \varepsilon_0 \zeta f(\kappa a_p)}{3 \eta} \quad \text{Equation 4.5}$$

where  $M$  is the mass of the deposit in time  $t(s)$ ,  $C_{sus}$  is the particle mass concentration in the suspension,  $E_{sus}$  is the electric field over the suspension,  $S$  is the substrate area,  $\alpha_d$  is a coefficient which takes into account that not all particles brought to the substrate are incorporated in the deposit ( $\alpha_d < 1$ ),  $\mu$  and  $\zeta$  are, respectively, the electrophoretic mobility and the  $\zeta$ -potential of ceramic particles, and  $f(\kappa a_p)$  is the Henry's function which depends on the relation between the thickness of the electric double layer ( $\frac{1}{\kappa}$ ) and the particle radius ( $a_p$ )<sup>[69]</sup>. In an electrochemical cell, the applied potential,  $E_{app}$ , consists of voltage drops at electrodes ( $E_{ele}$ ), suspension ( $E_{sus}$ ) and deposit ( $E_{dep}$ )<sup>[12]</sup>.

$$E_{app} = E_{ele} + E_{sus} + E_{dep} \quad \text{Equation 4.6}$$

When a constant voltage is applied,  $E_{sus}$  decreases with deposition due to the build-up of a resistive powder deposit on the substrate<sup>[244]</sup>,  $C_{sus}$  decreases due to particles deposition, and the other parameters, such as  $\alpha_d$ ,  $\mu$ ,  $\zeta$ , are assumed constant. The voltage drop over the deposit ( $E_{dep}$ ) is controlled by both the size and the electric potential of pores in the deposit, as well as the deposit thickness<sup>[160, 163]</sup>.

Substituting  $\mu$  with Equation 4.5, Equation 4.4 becomes:

$$M = \int_0^t \frac{2 \alpha_d \varepsilon_r \varepsilon_0 \zeta f(\kappa a_p) S C_{sus} E_{sus}}{3 \eta} dt \quad \text{Equation 4.7}$$

Equation 4.7 suggests that the deposit weight is proportional to the electric field over the suspension ( $E_{sus}$ ), the particle concentration in the suspension ( $C_{sus}$ ) and the  $\zeta$ -potential of particles ( $\zeta$ ). This is in accordance with the experimental results which show that the deposit weight increases with increased deposition time (Figure 4.6 (a)), applied voltage (Figure 4.6 (c)) and particle concentration (Figure 4.6 (d)). The deposition rate decreases with the deposition time, because the increase in the deposit weight reduces the particle concentration in the suspension and the deposited layer screens the applied voltage.

Figure 4.4 shows that the maximum  $\zeta$ -potential is reached at an electrical conductivity of  $1.9 \times 10^{-4} \text{ S/m}$ . According to Equation 4.7, the maximum deposit weight should also be



obtained at that value. However, Figure 4.6 (b) shows the maximum deposit is reached at an electrical conductivity of  $4.7 \times 10^{-5} \text{ S/m}$  and  $3.4 \times 10^{-5} \text{ S/m}$ , respectively, for the suspensions with  $50 \text{ kg/m}^3$  and  $150 \text{ kg/m}^3$  particle concentration. Such disagreement may be attributed to the difference between the  $\zeta$ -potential when the particle concentration was smaller than  $2.5 \times 10^{-2} \text{ kg/m}^3$  for the  $\zeta$ -potential measurement and that when the suspension ( $50 \text{ kg/m}^3$  or  $150 \text{ kg/m}^3$ ) was used for deposition. Much more particles used in EPD should consume more free ions in acetylacetone, resulting in a decrease in the electrical conductivity of the suspension (Figure 4.5). Therefore, it is reasonable to believe that when particles reach their maximum  $\zeta$ -potential, i.e. saturated with  $\text{H}^+$  ion adsorption, the content of free ions is lower in the suspension with a higher particle concentration, leading to a lower electrical conductivity for the maximum  $\zeta$ -potential. When the thickest deposit is obtained, the electrical conductivity ( $3.4 \times 10^{-5} \text{ S/m}$ ) of the suspension with  $150 \text{ kg/m}^3$  particle concentration is lower than that ( $4.7 \times 10^{-5} \text{ S/m}$ ) of the suspension with  $50 \text{ kg/m}^3$  particle concentration (Figure 4.6 (b)).

Although the  $\zeta$ -potential of particles in a concentrated suspension cannot be measured, it is expected to decrease with the particle concentration as more particle surfaces compete for consumption of free  $\text{H}^+$  ion in the solvent. The deposition efficiency decreases with the particle concentration, because the mobility of an individual particle decreases with increased particle concentration in the suspension (Figure 4.6 (d)). However, it is difficult to understand that the deposition efficiency increases with the particle concentration when the particle content is higher than  $150 \text{ kg/m}^3$ .

### §4.3.3 Particle packing during EPD

The increase in wet coating density during a densification process (Figure 4.8 and Figure 4.9) suggests that a distinct particle movement/rearrangement occurs in a D.C. electric field. It is reasonable to assume that deposited particles are dispersed in a solvent close to the electrode surface. As schematically shown in Figure 4.1, the local electric field around a deposited particle is distorted by the presence of charges on the particle surface, causing the electro-osmotic flow which can pull particles together to form aggregation. The aggregation velocity is proportional to the electro-osmotic velocity  $u$  [182].

$$u = \frac{\epsilon_r \epsilon_0 \zeta E_{dep}}{\eta d_w} \quad \text{Equation 4.8}$$

where  $E_{dep}$  is the voltage over the deposit and  $d_w$  is the thickness of wet coatings.

For the densification processes described in Figure 4.8, the original deposit is the same, thus, the electro-osmotic velocity can be simplified as:

$$u = KE_{dep} \quad \text{Equation 4.9}$$

where  $K$  is a constant integrating all other parameters in Equation 4.8. Equation 4.9 suggests that for a given deposit, the densification effect is only dependent on the electric field over the deposit. Since an applied voltage is over three parts in an EPD cell (Equation 4.6) and the electrode polarization is found to be negligible in this study, the electric field over the deposit can be written as:

$$E_{dep} = E_{app} \frac{d_w}{d_w + (b - d_w) \frac{r_s}{r_d}} \quad \text{Equation 4.10}$$

where  $b$  is the distance between two electrodes ( $1.0 \times 10^{-2} \text{m}$ ),  $r_s$  and  $r_d$  are, respectively, the specific resistance of the solvent/suspension which are inversely proportional to their electrical conductivity and the deposit, and  $d_w$  is the thickness of the wet coating.

For a given solvent (during the electric field densification), a higher applied voltage ( $E_{app}$ ), indicating a higher electric field over the deposit ( $E_{dep}$ ) according to Equation 4.10, can cause a more significant densification effect according to Equation 4.9. This is in accordance with Figure 4.8 (c), which shows the wet coating density increasing with the applied voltage. Equation 4.10 also indicates that the electric field over the deposit increases with the decrease in the solvent resistance, i.e. the increase in the electrical conductivity of the solvent. Thus, a higher wet coating density is obtained for the deposits which have been densified in the solvent with a higher electrical conductivity (Figure 4.8 (b)). It was also noted that the densification process completed within a time period, but not immediately. Figure 4.8 (a) shows that after a coating has been densified for 120s, the wet coating density reaches a maximum value, and with the densification time further

increasing, the wet coating density decreases slightly because the diffusion of deposited particles (Figure 4.8 (a)).

After EPD, a higher wet coating density is obtained in the coating which has been prepared with a longer deposition time (Figure 4.9 (a)) or under a higher applied voltage (Figure 4.9 (b)). In addition, both longer deposition time and higher applied voltage increase the deposit thickness, which is proportional to the deposit weight (Figure 4.6 (a) and (c)). For a given densification voltage, a faster electro-osmotic flow is expected in the deposit with a thinner deposit thickness due to the higher electric potential according to Equations 4.8 and 4.10, resulting in a more significant increase in the wet coating density (Figure 4.9).

In an EPD process, particle deposition and particle rearrangement occur at the same time. The wet coating density is a combining result of the deposition rate and the rearrangement ability of particles. In the initial period of EPD, the deposition rate is much higher than that at the latter period (Figure 4.6 (a)). At the beginning, the time to deposit particles may be too short for particles to find optimum positions at the substrate surface, resulting in a loose packing structure, whereas, in the latter period, a longer time is available for the particles to find optimal positions. A gradient structure is expected for EPD deposits, i.e. loose bottom and dense top, which has been observed in other experiments <sup>[249]</sup>. When the applied voltage is increased from 15V to 480V, the deposit rate increases, and the velocity of electro-osmotic flow also increases according to Equations 4.8 and 4.10. The two effects from both particle deposition and particle rearrangement compete with each other, resulting in an increase in the wet coating density with the applied voltage (Figure 4.7 (c)). An increase in the electrical conductivity of the suspension results in an increase in both the particle  $\zeta$ -potential (Figure 4.4) and the electric field over the deposit (Equation 4.10), which both facilitate the particle rearrangement by the electro-osmotic flow (Equation 4.8, Figure 4.7 (b)).

The variation of the wet coating densities with the particle concentration in the suspension is complicated. As the particle concentration increases, the deposition rate increases (Figure 4.6 (d)), which decreases the packing efficiency of particles. Therefore, the wet coating density decreases when the particle concentration increases from 150kg/m<sup>3</sup> to 250kg/m<sup>3</sup>.

However, it is not clear why the wet coating density increases when the particle concentration increases from  $100\text{kg/m}^3$  to  $150\text{kg/m}^3$ .

### §4.4 Summary

EPD was used to fabricate YSZ coatings on metal substrates. Suspensions were prepared by blending submicrometer sized particles with acetylacetone. The charging mechanism of YSZ particles in acetylacetone is proton transfer. The addition of iodine can improve the  $\zeta$ -potential of YSZ particles, and thus increase the suspension stability, particularly for the suspensions with a particle concentration higher than  $150\text{kg/m}^3$ . The deposition kinetics of a deposition process was characterized by measuring both the deposit weight and the deposition rate/efficiency. The packing density of particles in a wet deposit was analyzed as a function of various deposition conditions. The results are consistent with the rearrangement of particles induced by electro-osmotic flow which resulted from the distortion of the local electric field with the presence of charged deposited particles. The rearrangement ability is proportional to the strength of the local electric field in the deposit and the  $\zeta$ -potential of YSZ particles. The packing density of EPD particles is a function of both the deposition rate and the electric-field-induced rearrangement of particles, which increases with the longer deposition time, the higher applied voltages and the higher suspension electrical conductivity. In addition, the packing density of EPD particles further increases when the deposit is immersed in pure acetylacetone with a constant electric field applied.

## Chapter 5 Microstructural Development in EPD Coatings

### §5.1 Introduction

It has been discussed in Chapter 4 that particle packing densities of as-deposited wet EPD coatings varied with EPD conditions, i.e. the deposition time, applied voltages and etc., however, how these differences of wet coating densities caused during EPD can further influence the microstructures of EPD coatings after drying and sintering was left unrevealed. Properties of raw particles, such as the particle size, shape and surface morphology, are important during the formation of ceramic coatings and they control the microstructures of ceramic coatings<sup>[250]</sup>. Studies on effects of particle size on EPD coatings have been reported, Sato et al.<sup>[42]</sup> found the effect of  $\text{YBa}_2\text{Cu}_3\text{O}_7$  particle size reduction on crack formation, Hyam et al.<sup>[40]</sup> revealed the boron particle size effect on suspension stability and the chronoamperometry during EPD, and Guelcher et al.<sup>[41]</sup> modelled the aggregation behaviour of two particles deposited on the electrode, and suggested that smaller particles tended to more easily form agglomerates than larger particles. However, there were few studies on the effect of particle sizes or particle size distributions on the deposition process during EPD, such as on the deposition rate and on the coating density, as well as their effects on the microstructures of green and sintered EPD coatings.

In this Chapter, four batches of YSZ particles with different particle sizes are used to prepare suspensions for EPD. The agglomerate size distributions of those particles in acetylacetone and the stability of those suspensions are quantified and systematically analyzed. Microstructures of EPD coatings obtained are characterized from wet densities, green densities and freely sintered densities, and the microhardness of freely sintered coatings are also examined to evaluate the uniformity of particle packing conditions, i.e. the agglomerate conditions, in the EPD coatings. The microstructural developments during the electric field densification are also examined by contrasting them with EPD coatings without the electric field densification.

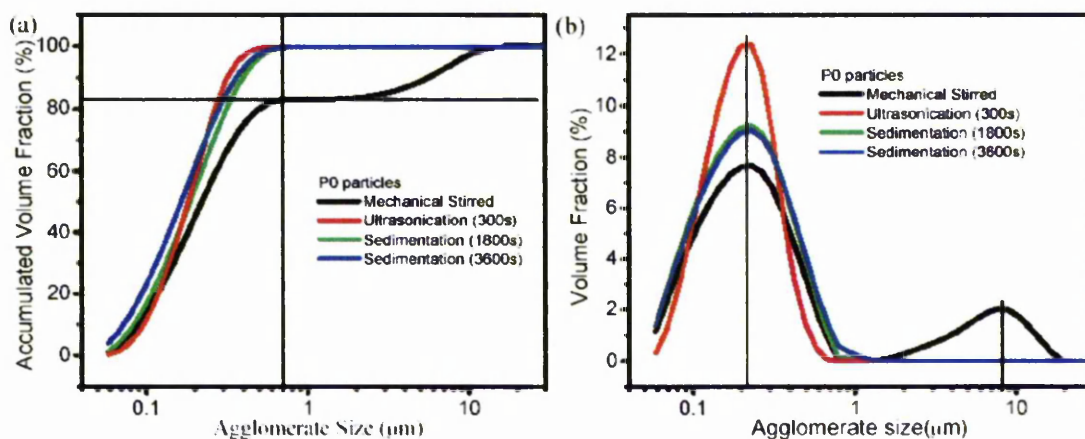
## §5.2 Results

### §5.2.1 Characterisation of suspensions

Raw particles were all commercially available YSZ (Pi-KEM), and the dispersing solvent was acetylacetone. The preparation of the suspension followed the procedure stated in Chapter 3.

#### §5.2.1.1 Agglomerate size distributions of particles

The agglomerate size distributions of the four batches of particles dispersed by various pre-treatments in acetylacetone, i.e. by the mechanical dispersion (mechanical stirred for 15 minutes at 240rpm), by the ultrasonication (22.5 kHz ultrasonic probe treated for 5 minutes) and by the sedimentation (settled for up to 60 minutes), were shown in Figure 5.1. Both the cumulative volume fraction and the individual volume fraction as a function of agglomerate sizes were plotted for each batch of particles.



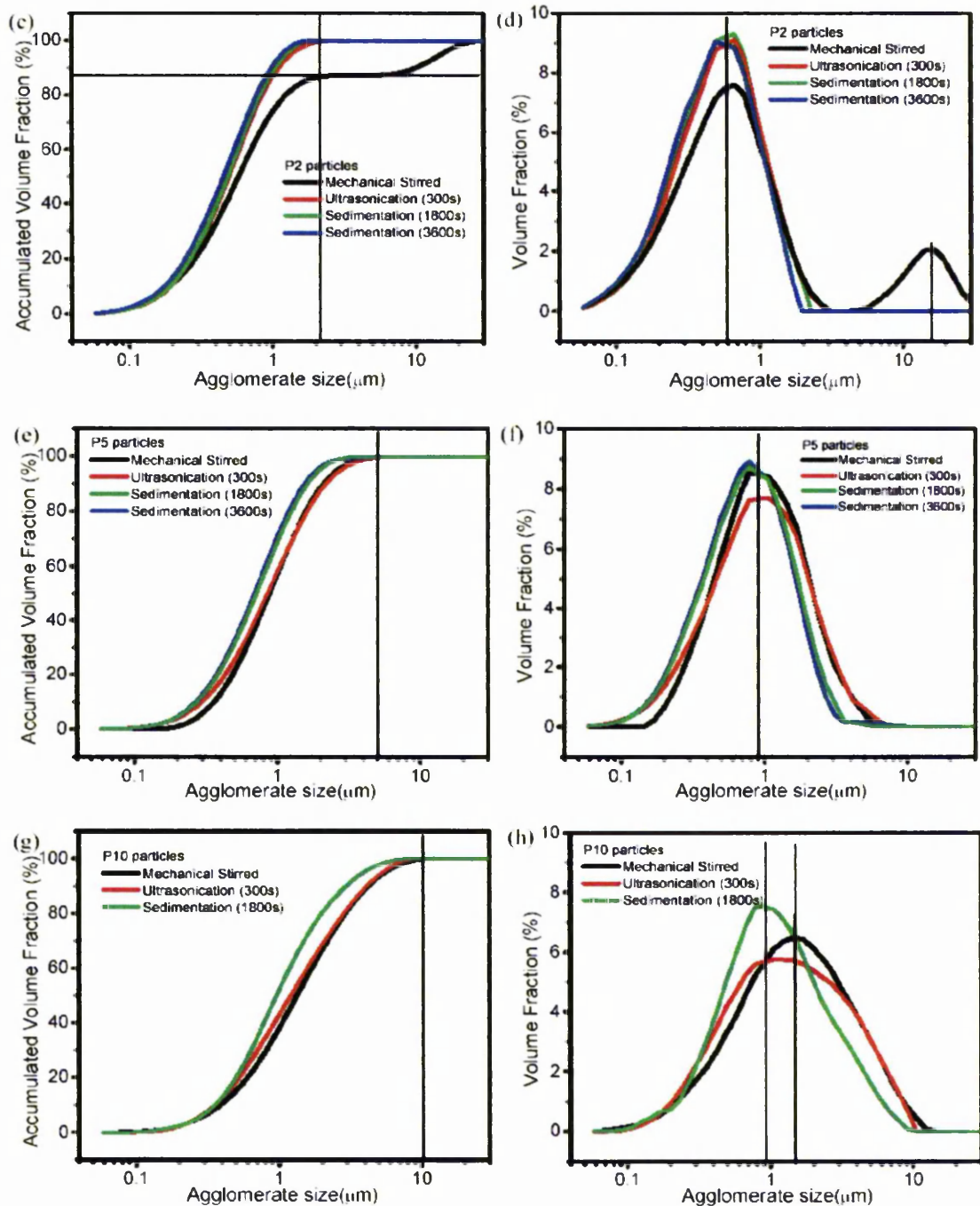


**Figure 5.1 Agglomerate size distributions of particles (a) and (b) P0, (c) and (d) P2, (e) and (f) P5 and (g) and (h) P10 after different pre-treatments, i.e., mechanical stirred for 15 minutes, ultrasonication treated at 22.5kHz for 5 minutes, or settled for up to 60 minutes**

Figure 5.1 (a) shows the accumulated volume fraction of P0 particles, which showed at least 80% of particles with agglomerate sizes smaller than  $0.71\mu\text{m}$ . By sufficient (5 minutes) ultrasonic treatment, those ~18% (black lines in Figure 5.1 (a)) second-ordered soft agglomerates could be broken into first-ordered agglomerates with sizes less than  $0.71\mu\text{m}$ . In Figure 5.1 (b), a bimodal curve for the mechanical stirring treated P0 particles indicated that it was difficult to break up the second-ordered agglomerates by mechanical dispersion. To break-up the soft agglomerate in the colloidal suspension of ceramic particles, ultrasonication is a widely adopted technique. The chemical and physical effect of ultrasonic wave on particle is via the formation, growth and implosive collapse of bubbles in a liquid. During the process, the implosive collapse of the bubble generates localized hot spots through adiabatic compression or shock wave formation within the gas phase of the collapsing bubble <sup>[251]</sup>. Also the suspensions were steadily settled, for up to 1 hour, after ultrasonic treatment to evaluate the stability of suspensions and the agglomerate sizes were measured after certain sedimentation times (30 minutes and 1 hour). For P0 particles no significant size difference was found after the sedimentation which meant that the P0 particles were suspended stably in acetylacetone suspension. To effectively quantify the agglomerate size of particles from the particle size distribution curves, the average agglomerate size ( $a_{50}$ ) was defined. In the accumulated volume fraction curves (Figure 5.1 (a)), the corresponding agglomerate size, where 50% of particles were smaller than that size, was treated as average agglomerate size ( $a_{50}$ ); and in the same way, for example,  $a_{80}$  represented the agglomerate size where 80% of particles were smaller than the size. For ultrasonically treated P0 particles, the average agglomerate size ( $a_{50}$ ) was determined to be approximate  $0.19\mu\text{m}$ .

Figure 5.1 (c) and (d) show agglomerate size distributions of P2 particles, Again, there were second-ordered agglomerates ( $\sim 16\mu\text{m}$ , small peak in Figure 5.1 (d)) detected in P2 suspensions, if the suspensions were only pre-treated with mechanical dispersing. After ultrasonic treatment, those second-ordered agglomerates, about 13% of the total volume (marked as black lines in Figure 5.1 (c)), in P2 suspensions were eliminated, whereas the sizes of first-ordered agglomerates were not affected by the ultrasonication. P2 had an  $a_{100}$  value approximate  $2.0\mu\text{m}$  (Figure 5.1 (c)). The sedimentation experiments indicated P2



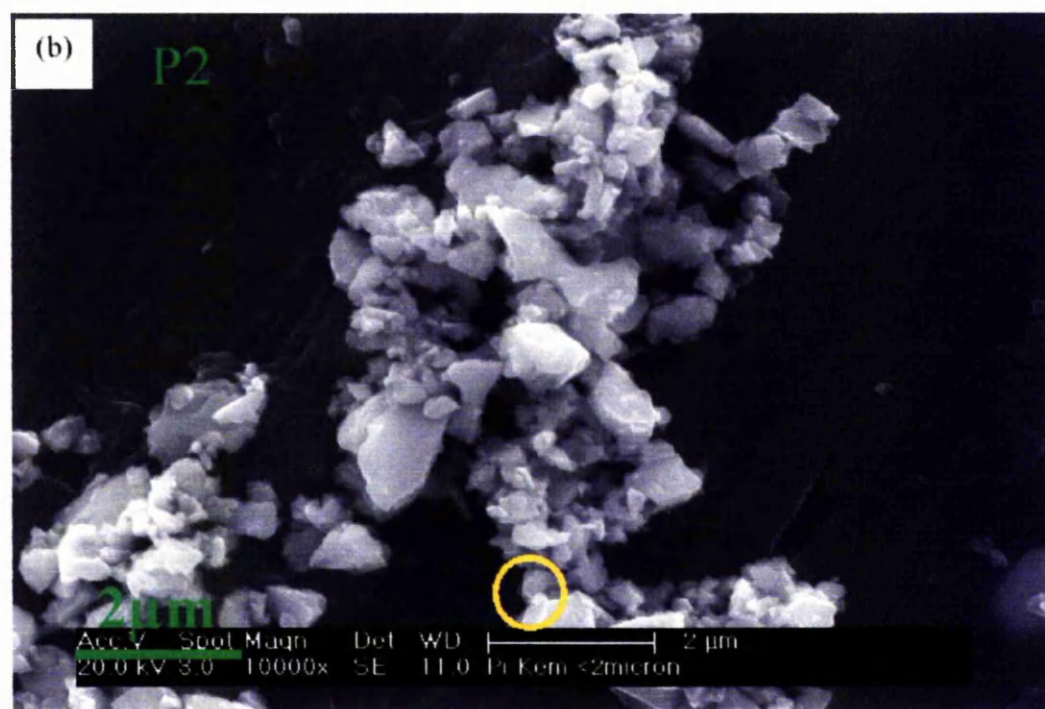
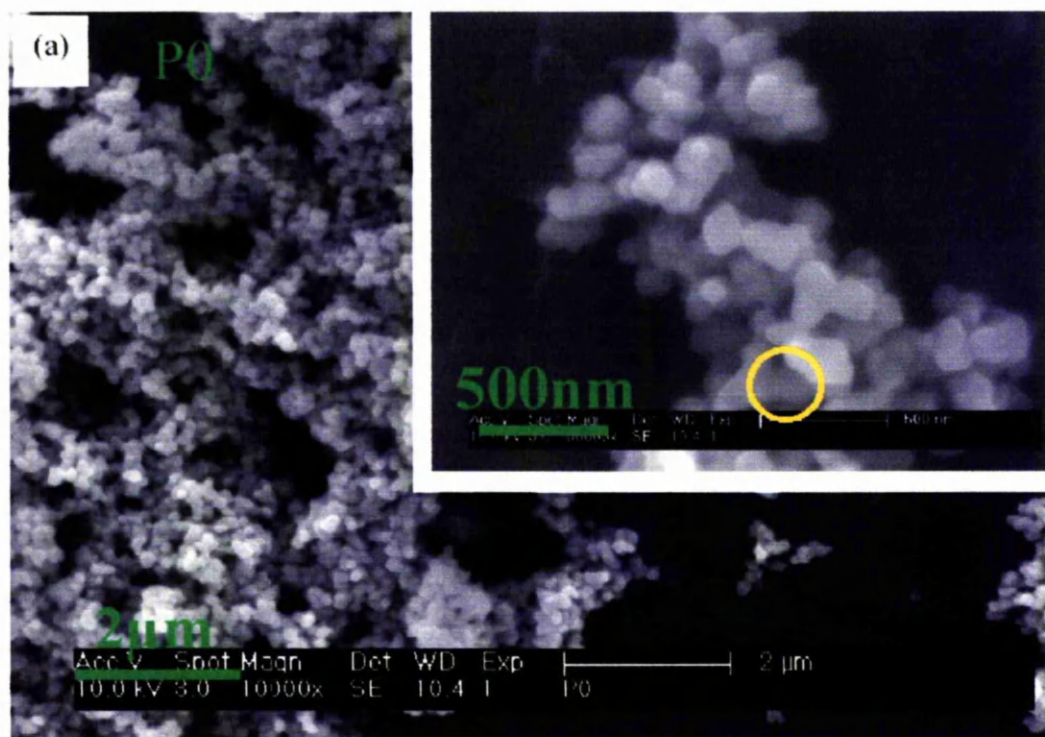
particles in acetylacetone were stable. The average agglomerate size ( $a_{50}$ ) of P2 in acetylacetone suspension was around 0.50 $\mu\text{m}$ .

Figure 5.1 (e) and (f) were the size distributions of P5 particles, and P5 had  $a_{100}$  approximate 5.0 $\mu\text{m}$ . There were no second-ordered agglomerates detected in P5 suspensions. The ultrasonication still could affect the agglomerate sizes of P5 suspensions, though the  $a_{50}$  value was not changed by the ultrasonication, the agglomerate size distributions for particles with sizes less than  $a_{30}$  (0.60 $\mu\text{m}$ ) were affected, which indicated that relatively smaller particles in P5 suspensions could get well dispersed from the ultrasonication. Those relatively large particles (larger than 4 $\mu\text{m}$ ) in P5 suspensions might settle down during sedimentation, which appeared in the diagrams as  $a_{100}$  decreased from ~5.0 $\mu\text{m}$  to ~4.0 $\mu\text{m}$  after 1 hour's sedimentation. The average agglomerate size ( $a_{50}$ ) for P5 particles was approximate 0.87 $\mu\text{m}$  Figure 5.1 (e).

The agglomerate size distributions of P10 particles were shown in Figure 5.1 (g) and (h), in which it can be found that the  $a_{100}$  of P10 particles was ~10 $\mu\text{m}$ . The ultrasonication had relatively little effect on larger particles but did broaden the size distribution peak slightly to the smaller sizes, which indicated agglomerates formed by relatively small particles could be broken down by the ultrasonication. The sedimentation of relatively large particles was detected for P10 particles within 30 minutes, which decreased  $a_{50}$  from 1.23 $\mu\text{m}$  to 0.97 $\mu\text{m}$ , which indicated that P10 suspensions were less stable than other particles, P0, P2 and P5, because of the large sizes.

The agglomerate size measurements of particles suggested that sufficient, 5 minutes in the present study, ultrasonic treatments were essential for preparing suspensions with well dispersed particles, however longer time ultrasonication might cause significant temperature increase of the suspension and other side-effects which were out of the scope of the current study. Figure 5.1 also provided information on the stability of suspensions against sedimentation, which indicated that suspensions studied in this study could be treated as stable suspensions for short period EPD, e.g. 4 minutes deposition time.

§5.2.1.2 Particle shape and surface morphology



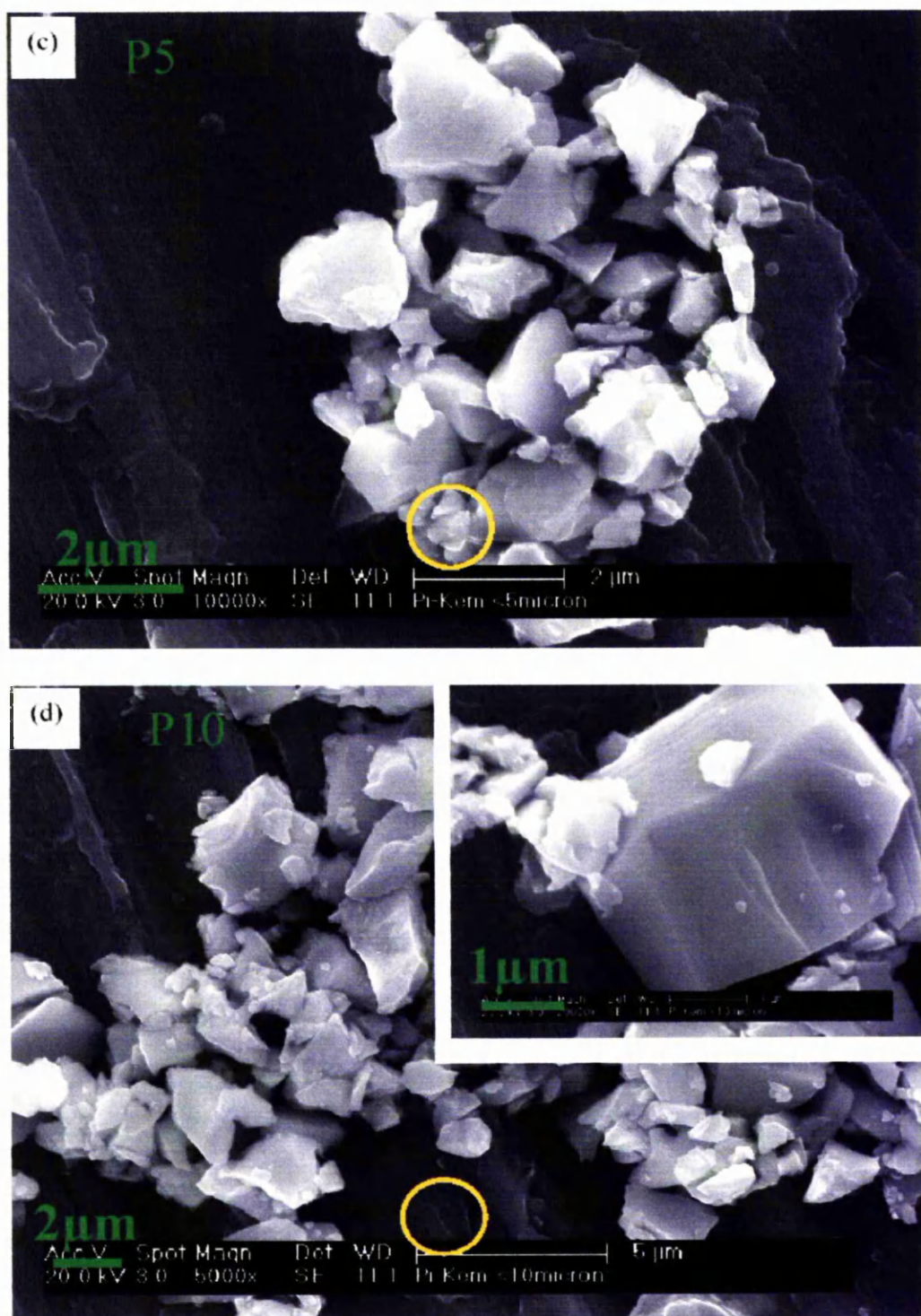


**Figure 5.2 SEM images of raw particles (a) P0, (b) P2, (c) P5 and (d) P10**

(Yellow circles describing the average size obtained from Figure 5.1)

SEM images shown in Figure 5.2 revealed the shapes and surface conditions of raw particles. P0 particles had spherical like shapes and smooth surfaces with relatively uniform sizes, which can be clearly observed from the image with higher magnification showed on the top right corner of Figure 5.2 (a). Figure 5.2 (b), (c) and (d) show that P2, P5 and P10 particles were all having random shapes. From the high magnification image shown on the top right corner of Figure 5.2 (d), dense and large particles could be found in those particles, which also had smooth surfaces. Significant differences of particle sizes were noticed for P2, P5 and P10 particles, in which both small, with sizes smaller than  $0.5\mu\text{m}$ , and large, with sizes larger than  $1\mu\text{m}$ , particles were coexisting in those batches of particles. The difference in particle sizes for each individual batch of particles could also be quantified by calculating the standard deviation of each size distribution curve showed in Figure 5.1, and the resulted values were listed in Table 5.1. A higher standard deviation value represented a broader particle size distribution, and this aspect for particles with widely distributed sizes was further discussed in later sessions.

**Table 5.1 BET surface area and statistically quantified agglomerate-size results of raw particles**

Particles	P0	P2	P5	P10
BET surface area ( $\times 10^3 \text{ m}^2/\text{kg}$ )	$8.1 \pm 0.2$	$7.2 \pm 0.2$	$4.5 \pm 0.2$	$2.7 \pm 0.2$
Average size $a_{50}$ ( $\mu\text{m}$ )	0.19	0.50	0.87	1.23
Standard deviation ( $\frac{a_{84.1}}{a_{50}}$ )	1.524	1.825	2.038	2.665

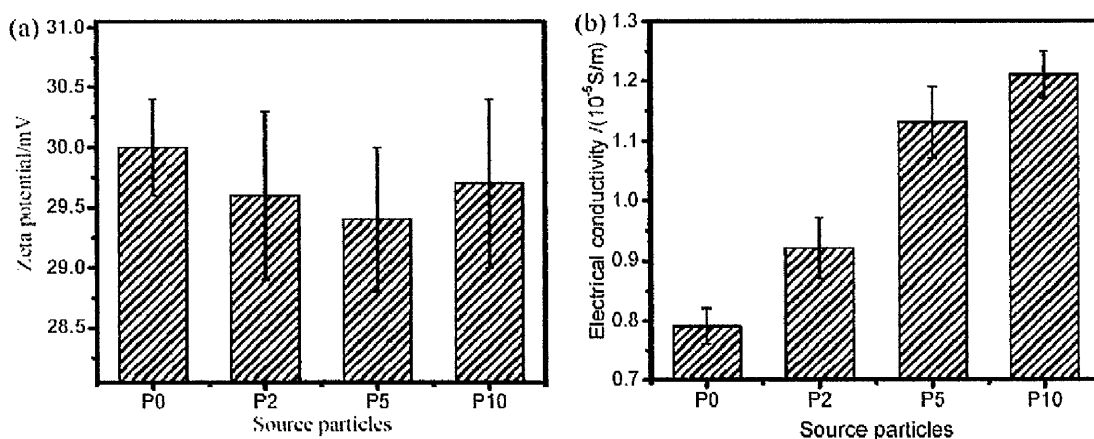
The surface condition of particles was also examined by the BET surface area method. The BET surface area and the average agglomerate sizes as well as the standard deviation of those particles obtained from Figure 5.1 were listed in Table 5.1, and those average agglomerate sizes of each batch of particles were also marked as yellow circles in each corresponding image shown in Figure 5.2. By comparing values of the four batches of particles shown in Table 5.1, it can be found that P0 particles showed the smallest  $a_{50}$  size



but the highest BET surface area and they had the smallest standard deviation which reflected the most uniform sizes. P10 particles showed the largest  $\alpha_{50}$  size but the lowest BET surface area and they had the largest standard deviation which meant they had the broadest size distribution. Those quantified values of particles showed a consistent trend with the observation from Figure 5.2.

#### §5.2.1.3 Zeta potential and electrical conductivity of suspensions

Effects of sizes of raw particles on properties of the suspension were characterized from the particle zeta potential and the suspension electrical conductivity, which has been identified to be effective on particle packing during EPD in Chapter 4, and the results of both zeta potential and electrical conductivity were plotted for each batch of raw particles in Figure 5.3.



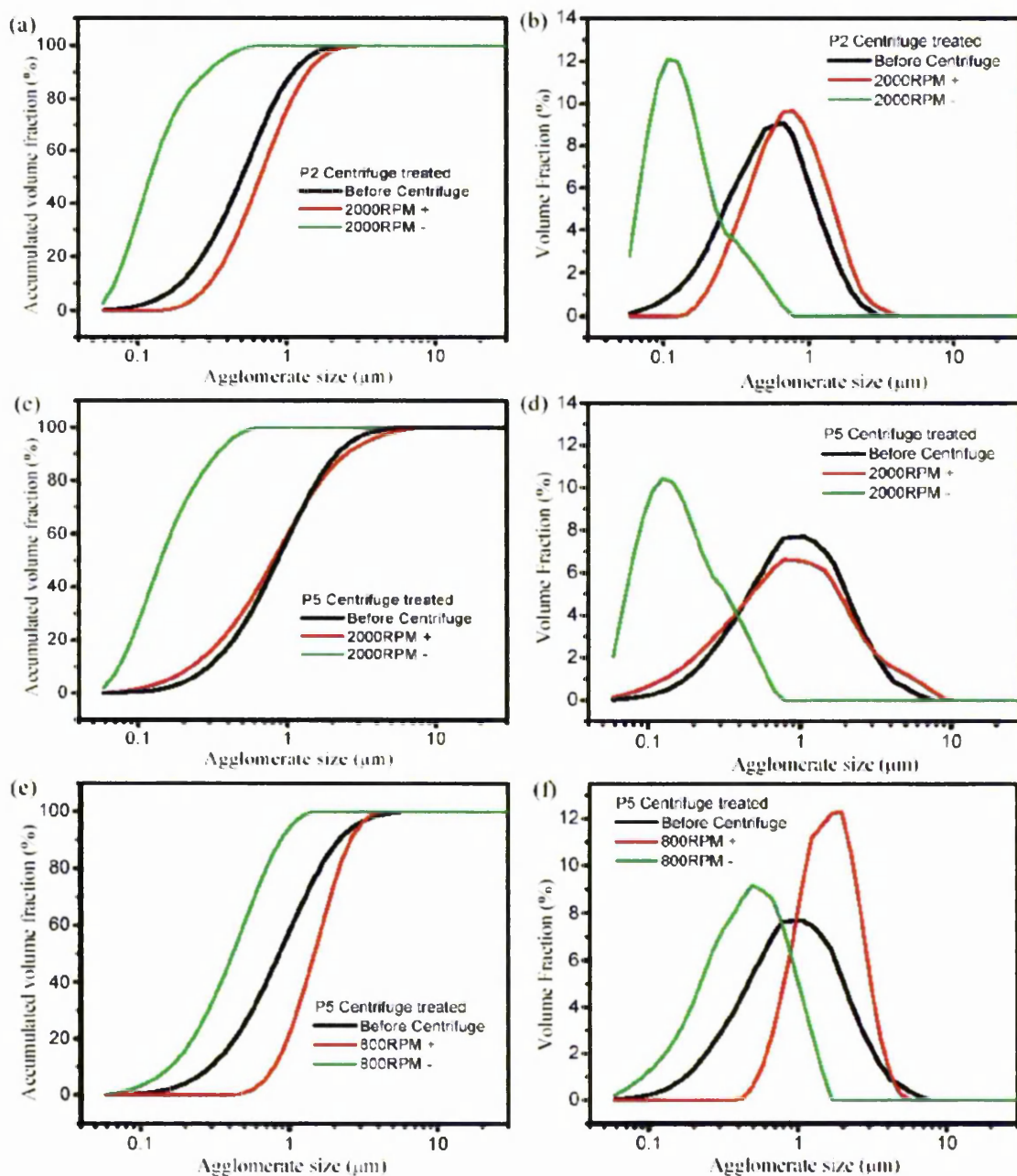
**Figure 5.3 Properties of P0, P2, P5 and P10 suspensions (a) zeta potential of particles and (b) electrical conductivity of suspensions**

Figure 5.3 (a) presents the measured zeta potentials of the four batches of particles in acetylacetone without any additives. It can be found that the zeta potential varies within a very narrow range ( $29.7 \pm 0.3$  mV) for those particles regardless of particle sizes, which could be treated as same zeta potentials. The surface charging mechanism of zirconia particles in acetylacetone has been discussed in Chapter 4 with Equations 4.1 and 4.2. Classical electrokinetic theory also indicated that there was no dependence of zeta potential on the particle sizes<sup>[69]</sup>, if particles and dispersing solvent were all the same.

The electrical conductivity of suspensions has been identified to vary with particle concentration in Chapter 4, so in the present study of the electrical conductivity of the suspension for different particles, a fixed particle concentration,  $50\text{kg/m}^3$ , was prepared for all four batches of particles, and the results were listed in Figure 5.3 (b). The electrical conductivity of suspension was slightly higher for particles with larger sizes. Two kinds of charge-carriers in the suspension contributed to the electrical conductivity of suspension as discussed in Chapter 4, which were free ions deionised from the acetylacetone molecules (Equation 4.1), and charged particles whose charging mechanism has been explained in Equation 4.2. The addition of particles into acetylacetone caused decreasing of the concentration of free ions in the suspension, so that the electrical conductivity decreased when particles were added into acetylacetone. Because the particle charging reaction/adsorption mainly happened on the surfaces of particles, the surface area of particles was the most determinative factor of controlling the concentration of free ions in the suspension, i.e. particles with higher surface area tended to adsorb more free ions (Equation 4.2) and leave less free ions in the suspension. The electrical conductivity of the suspension was one reflection of the concentration of free ions in the suspension, so for suspensions with same particle concentrations in the suspension, particles with higher surface area consumed more free ions and caused a lower electrical conductivity of the suspension. Figure 5.3 (b) proved that particles with higher surface areas, i.e. P0 particles, had lower electrical conductivity of their acetylacetone suspension than particles with lower surface areas, i.e. P5 and P10, did.

### §5.2.1.4 Centrifuge separation of particles

From SEM observation and quantitative analysis of the agglomerate size distribution curves of those particles, it has been found that of all those four batches of particles only P0 had relatively uniform sizes, whereas particle sizes of P2, P5 and P10 particles all showed non-uniform features. Both relatively small ( $<0.5\mu\text{m}$ ) particles and relatively large ( $>1.0\mu\text{m}$ ) could be found in P2, P5 and P10 particles, which could be treated as mixed sized particles. Centrifuge treatments were carried out on P2 and P5 particles to separate those particles, and to obtain more information on the mixed sized feature of those particles.



**Figure 5.4 Agglomerate size distributions of centrifuge treated particles (a) and (b) P2 after 2000RPM centrifuge treated, (c) and (d) P5 after 2000RPM centrifuge treated and (e) and (f) P5 after 800RPM centrifuge treated**

**Table 5.2** Statistic quantified data of centrifuge treated particles

Centrifuge treated Particles	2000RPM				800RPM	
	P2-	P2+	P5-	P5+	P5-	P5+
Average size $a_{50}$ ( $\mu\text{m}$ )	0.12	0.67	0.14	0.87	0.41	1.51
Standard deviation ( $\frac{a_{84.1}}{a_{50}}$ )	1.926	1.813	2.029	2.232	1.838	1.551
Mass ratio (%)	27.6	72.4	5.6	94.4	44.6	55.4

Centrifuge treated particles were separated into two individual groups of particles, the settled down relative large particles (referred as “+”), and the remained up suspending relative small particles (referred as “-”). The separated “+” and “-” particles were measured respectively of the agglomerate size distributions and compared to those of the original particles, and the distribution curves and quantitatively analysed results were showed in Figure 5.4 and Table 5.2 respectively. It can be found that the centrifuge treatments were effective on separating particles by comparing their  $a_{50}$  sizes (Table 5.2). Under high centrifuge speed, i.e. 2000RPM, very small particles could be separated out from P2 (P2-  $a_{50}=0.12\mu\text{m}$ ) and P5 (P5-  $a_{50}=0.14\mu\text{m}$ ) particles, however, the standard deviations of the separated “+” and “-” particles were not affected significantly because of the relatively low mass ratio of those very small “-” particles in the raw particles (27.6% in P2 and 5.6% in P5). After relative low-speed centrifuge, i.e. 800RPM, P5 particles were separated almost equally (44.6% “-” particles and 55.4% “+” particles), and more over the standard deviations of those separated particles were reduced, which meant that the size distribution has been narrowed down. So the centrifuge speed for the separation of P5 particles was selected to be 800RPM for further studies on the size effects on EPD coatings.

SEM images of P5- and P5+ (800RPM) particles were shown in Figure 5.5 to provide direct information on the sizes separated by the centrifuge. Obvious differences were found on particle sizes between P5- and P5+ which indicated an effective size separation.



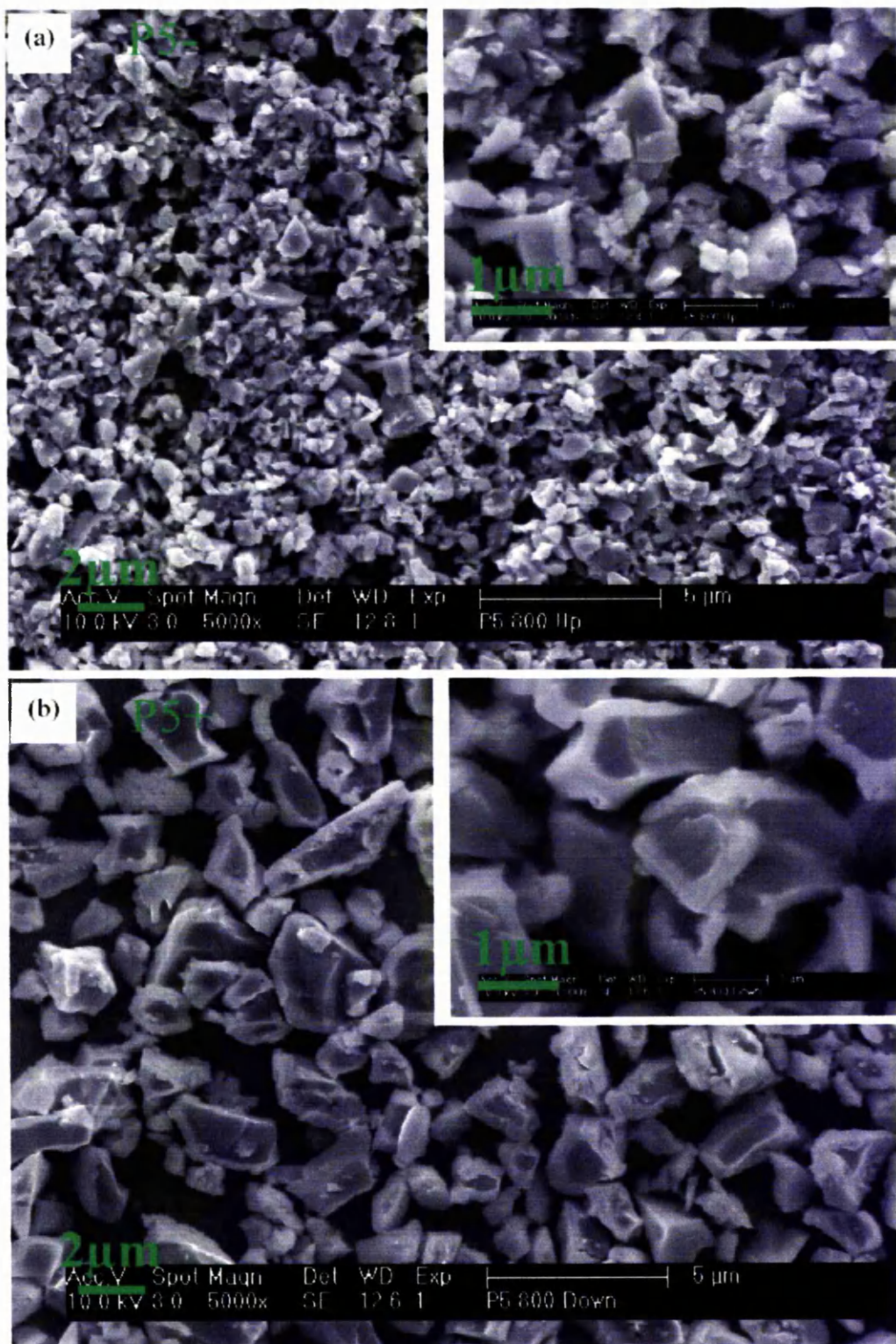


**Figure 5.5 SEM images of 800RPM centrifuge treated P5 particles (a) P5- and (b) P5+**

### §5.2.2 EPD of particles with different sizes

After systematically characterising the raw particles and their corresponding acetylacetone suspensions, EPD was carried out to study the coating formation processes and the effects of agglomerate sizes on microstructures of EPD coatings.

#### §5.2.2.1 Formation of EPD coatings

EPD experimental conditions were fixed for all coatings, i.e. the applied voltage was 120V, deposition time was 240s, and particle concentration was  $50\text{kg/m}^3$  and no addition of iodine for all coatings, so the only differences were the agglomerate sizes for various raw particles. Effects of the electric field densification on each EPD coating were also examined by comparing coatings with and without the electric field densification. For the reason of producing significant enough contrast for the effects of the electric field densification, a high voltage (240V) and long time (240s) were used for the electric field densification process.

The measured properties of EPD coatings during formation, i.e. the deposit weight, wet coating density ( $\rho_w$  in Equation 3.1), wet coating thickness ( $d_w$  in Equation 3.2) and the coating thickness shrinkage during drying ( $\delta$  in Equation 3.3), were measured for different raw particles and shown in Figure 5.6.

Figure 5.6 shows general relations between particle sizes of raw materials and properties of EPD coatings, which indicated that particles with larger sizes could lead to higher deposit weight (Figure 5.6 (a)) and higher wet coating density (Figure 5.6 (b)). EPD coatings with large particles had relatively thinner wet coating thickness (Figure 5.6 (c)), which could attribute mainly to the higher wet coating density of those coatings. The thickness shrinkage during drying,  $\delta$ , followed the same trend as the wet coating thickness (Figure 5.6 (d)), which was also determined by the wet coating density.

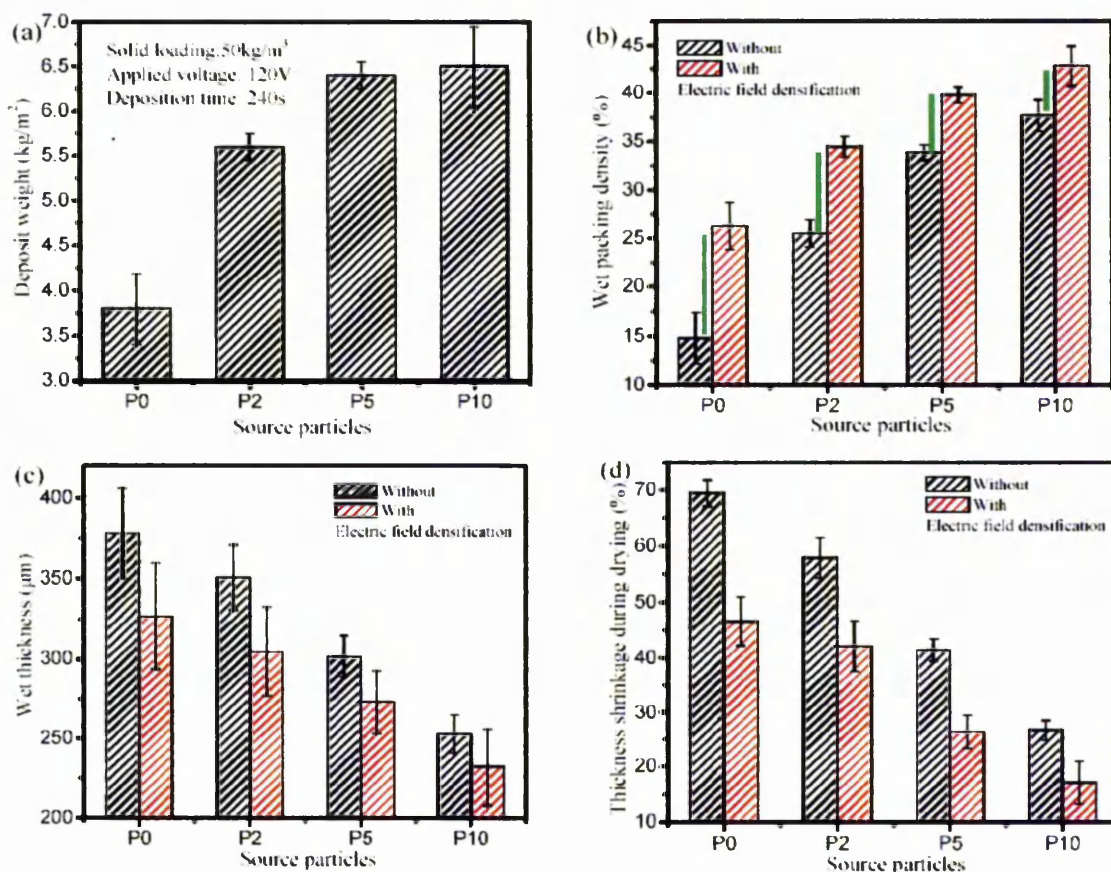


**Figure 5.6 Measured properties of EPD coatings fabricated from various raw particles with different sizes (a) deposit weight, (b) wet packing density, (c) thickness of wet coating, and (d) coating thickness shrinkage during drying**

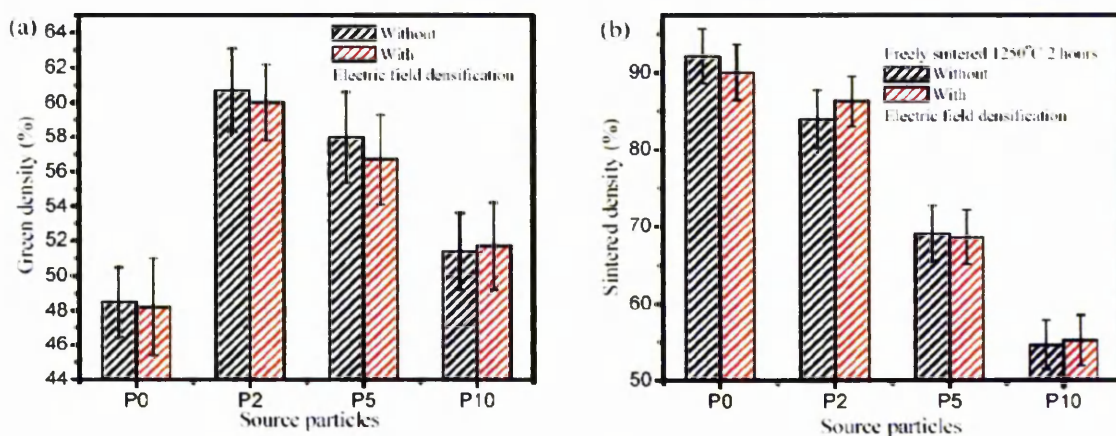
The electric field densification increased the wet coating density as was revealed in Chapter 4, while it was found in Figure 5.6 (b) that the electric field densification was more effective for EPD coatings with small particle sizes. The green bars showed in Figure 5.6 (b) indicated the differences in wet coating densities caused by electric field densification. It was clearly shown that P0 coatings could be affect much by the electric field densification, whose wet coating density increased from 14.8% to 26.3% after the electric field densification. For coatings with larger particles, i.e. P2, P5 and P10 coatings, the effect of the electric field densification on wet coating densities became less significant gradually with increasing sizes. For coatings with the largest particle size (P10 particles), the increase of the wet coating density from the electric field densification reduced to approximately 5.1% (from 37.7% to 42.8%).



Figure 5.6 (c) and (d) show the dependence of wet coating thickness and the thickness shrinkage during drying on particle size, and they indicated that smaller particles tended to build thicker wet deposits with lower particle packing densities and to provide coatings with more shrinkage during drying. Systematic studies on the constrained drying behaviour of YSZ slurries on metallic substrate have been reported [7-9]. The thickness shrinkage also reflected the rearrangement of deposited particles during drying. The electric field densification processes decreased the wet coating thickness and also lowered the rearrangement of deposited particles during drying.

#### §5.2.2.2 Microstructure

For studying the microstructures of EPD coatings, it is essential to know the coating densities of those EPD coatings. To simplify the study, EPD coatings were removed from the substrate and were sintered without the constraint of the substrate to understand the particle packing conditions of EPD coatings. Identical sintering conditions, 1250°C for 2 hours with  $\pm 3^\circ\text{C}/\text{minute}$  heating/cooling rates, were applied for all coatings in this Chapter. Systematic studies on sintering conditions and the substrate constraint effects during sintering will be discussed in Chapter 6.



**Figure 5.7 EPD coatings fabricated with different particle sizes, (a) green density and (b) freely sintered density at 1250°C for 2 hours**

Figure 5.7 (a) shows the green densities of EPD coatings fabricated from the four batches of source particles. It can be seen from the diagram that coatings fabricated from particles with relative broad size distributions, i.e. P2, P5 and P10 coatings, had higher green

densities than P0 coatings, which had uniform particle sizes. Previous studies <sup>[35-39]</sup> on the important effects of particle sizes and particle size distributions on packing densities of powder compacts suggested that mixed sized particles or particles with broad size distributions can increase the bulk density. For the EPD coatings, the green densities were also determined by the agglomerate sizes of raw particles in the suspensions, and coatings with broad agglomerate size distributions showed high green densities. Apart from green densities, sintered densities are also important which may directly determine the coating performances during application. Freely sintered coatings were examined for further understanding of the effects of particle size on microstructures of EPD coatings, and the freely sintered densities were shown in Figure 5.7 (b). Freely sintered densities showed significant dependence on particle sizes, i.e. smaller particles provided higher sintered densities, and this phenomenon agreed with classical sintering theories on that smaller particles benefit sintering.

The electric field densification showed limited effects on green and sintered densities. Neither green nor sintered densities could be contrasted out by the electric field densification even though there were significant differences on wet coating densities (Figure 5.6 (b)) caused by the electric field densification. It implied that there were no direct relations between wet coating densities and dry coating densities, whereas the agglomerate sizes were the dominant factor on determining dry coating densities and freely sintered densities.

For further examination of the microstructures of those EPD coatings, observations on fracture surfaces of sintered coatings were taken by SEM, and images were shown in Figure 5.8. Different micro-packing structures were noticed for electric field densified coatings by comparing the images shown in Figure 5.8. For P0 coatings, agglomerate-like microstructures were found in coatings with the electric field densification, and inter-agglomerate voids (marked in a red circle in Figure 5.8 (b)) were also detected which were caused by the differential sintering within the coating due to the uneven packing of particles. For P5 coatings, special microstructures of smaller particles tightly gluing on the surfaces of larger particles (marked in a yellow circle in Figure 5.8 (d)) were extensively observed in coatings with the electric field densification, which were also believed to be introduced by

the electric field densification. Effects of the specific microstructures caused by the electric field densification on the properties of EPD coatings need further examination.

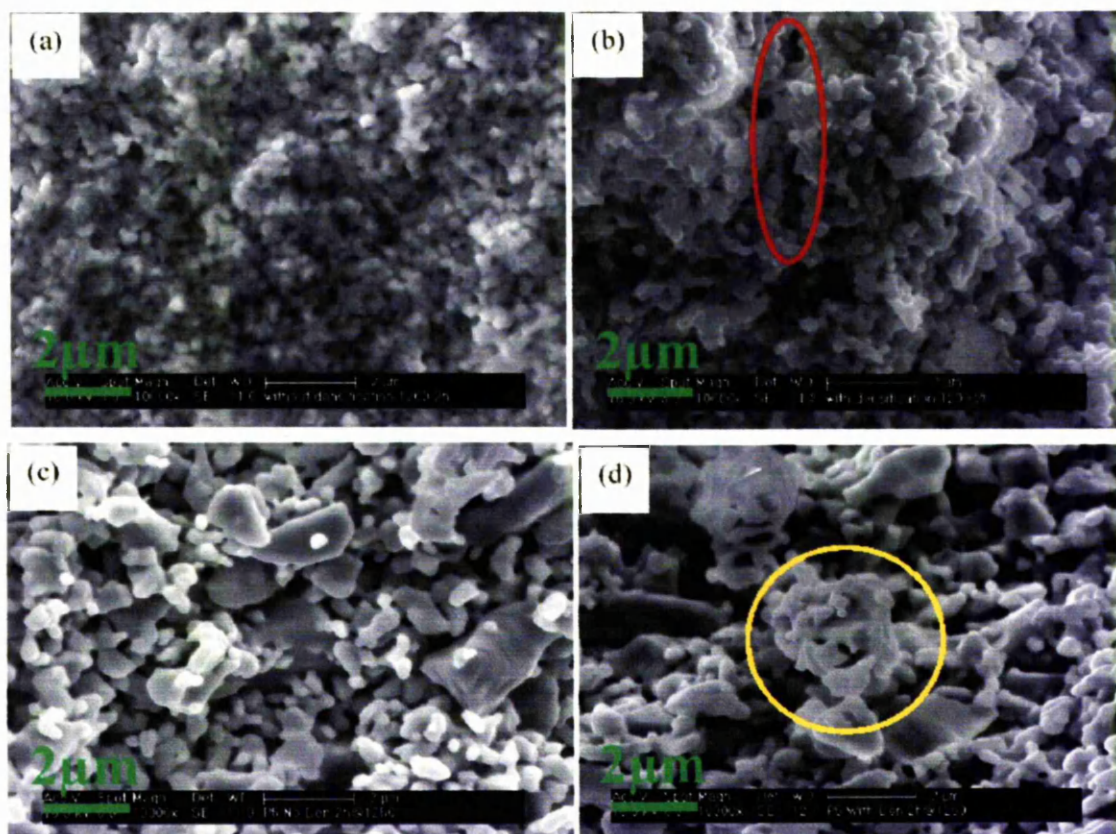


**Figure 5.8 SEM images of fracture surface of sintered coatings (a) P0 without densification, (b) P0 with densification, (c) P5 without densification, (d) P5 with densification**

(The red circle in (b) marking a micro-crack, the yellow circle in (d) marking a specific microstructure of small particles adhering on a large particle)

### §5.2.2.3 Microhardness of freely sintered EPD deposit

The mechanical properties of ceramic products are very important from both the scientific and the applications point of view. In this study, the micro-indentation hardness of freely sintered coatings, under identical sintering conditions, were examined to help understanding the effects of agglomerate sizes on EPD coatings and the microstructural developments in EPD coatings during the electric field densification.



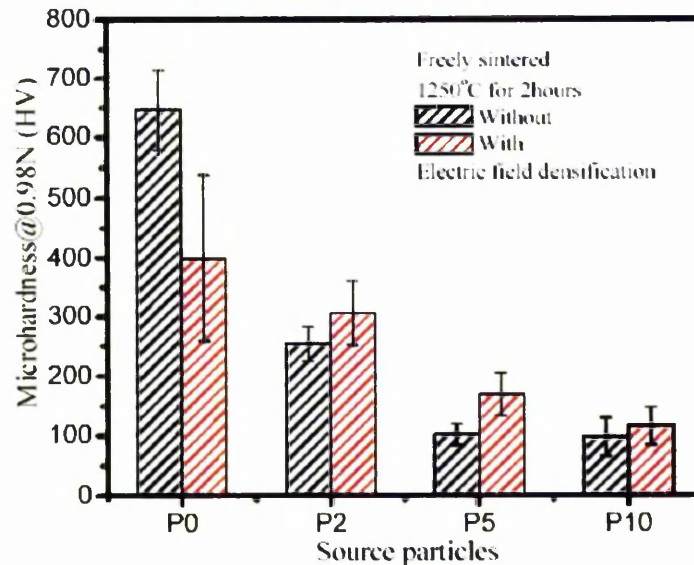


**Figure 5.9 Microhardness of freely sintered EPD coatings fabricated with different sized particles**

Figure 5.9 shows the hardness values of freely sintered EPD coatings fabricated from particles with various agglomerate sizes. It clearly indicated that coatings with larger particles had lower hardness after sintering, which implied that large particles showed lower sinterability than small particles which has been agreed by classic sintering theories [252].

It has been found that the coating densities, either green or sintered, showed negligible difference for EPD coatings with and without the electric field densification (Figure 5.7). However, the hardness of sintered coatings was found to be affected by the electric field densification process. P0 coatings showed lower hardness values ( $\sim 400\text{HV}_{0.08\text{N}}$ ) if they were treated by the electric field densification, than those normal EPD coatings without the electric field densification ( $\sim 650\text{HV}_{0.08\text{N}}$ ). This phenomenon for P0 coatings was attributed to local agglomerates within the coating induced by the electric field densification which then caused uneven shrinkage for intra-agglomerates and inter-agglomerates during sintering<sup>[58]</sup>, and as a consequence it caused uneven microstructures (highlighted by the red circle in Figure 5.8 (b)) between agglomerates to degrade the mechanical hardness of the coatings (Figure 5.9).

It was worth to notice that for P2, P5 and P10 coatings, the densification caused opposite effects on the coating hardness compared to P0 coatings, where the sintered coating hardness was higher for coatings with the electric field densification than without. The phenomena were attributed to the non-uniform agglomerate sizes of those P2, P5 and P10 particles. It has been found (Figure 5.6 (b), (c) and (d)) that coatings fabricated from smaller particles, i.e. P0 coatings, were affected more by the electric field densification than those from larger particles, i.e. P2, P5 and P10 coatings, which implied that smaller particles showed higher responses to the electric field densification than larger particles. So that those relatively small sized particles in P2, P5 and P10 coatings were arranged more during the electric field densification than relatively large sized particles. Those smaller sized particles could form agglomerates in two possible ways, either with other smaller particles or with those particles by attaching to them. From Figure 5.8 (d) it was found that there were certainly some relatively small particles attached on the surfaces of large particles, and such specific microstructures were the possible reason of higher hardness values of the sintered EPD coatings. It is well known that small particles have higher sinterability than large ones, so the position of small particles in the deposits must be one of the determining factors for the hardness of the sintered coatings. If particles were randomly packed in the coating (Figure 5.8 (c)), those contacting points between large particles were hard to be sintered and these contacts were more likely to convert to weak points after sintering which degraded the coating hardness, whereas if there were small particles existing at those large-large connections, those small particles performed as bridges between the two large particles and enhanced the connection as well as the over all hardness of coatings.

The electric field densification process provided not only the driving force, i.e. the electro-osmotic flow, to rearrange the deposited particles in the wet coating, but also a possible solvent environment, i.e. the depression of double-layer thickness around particles by ionic depletion, for gluing small particles onto surfaces of large particles (Figure 5.8 (d) marked in the yellow circle). And moreover, those relatively large particles in P2, P5 and P10 were found to be nearly fully dense (Figure 5.2 (b), (c) and (d)), they shrank little during sintering, so that those relatively small particles between them can finish the formation of bridging during sintering.



## §5.2.3 EPD of centrifuge separated particles

Particles separated in a centrifuge at 800 RPM were employed for EPD study. The nearly equally separated P5 particles, P5- and P5+ particles, show relatively narrow agglomerate size distributions (Figure 5.4 (e) and (f)). By using the centrifuge-treated P5 particles to carry out EPD, the functions of both small sized particles and large sized particles on the microstructural developments of EPD coatings were examined individually and compared to the original P5 coatings for further understanding of the deposition process during EPD, i.e. the deposition weight and the particle packing densities.

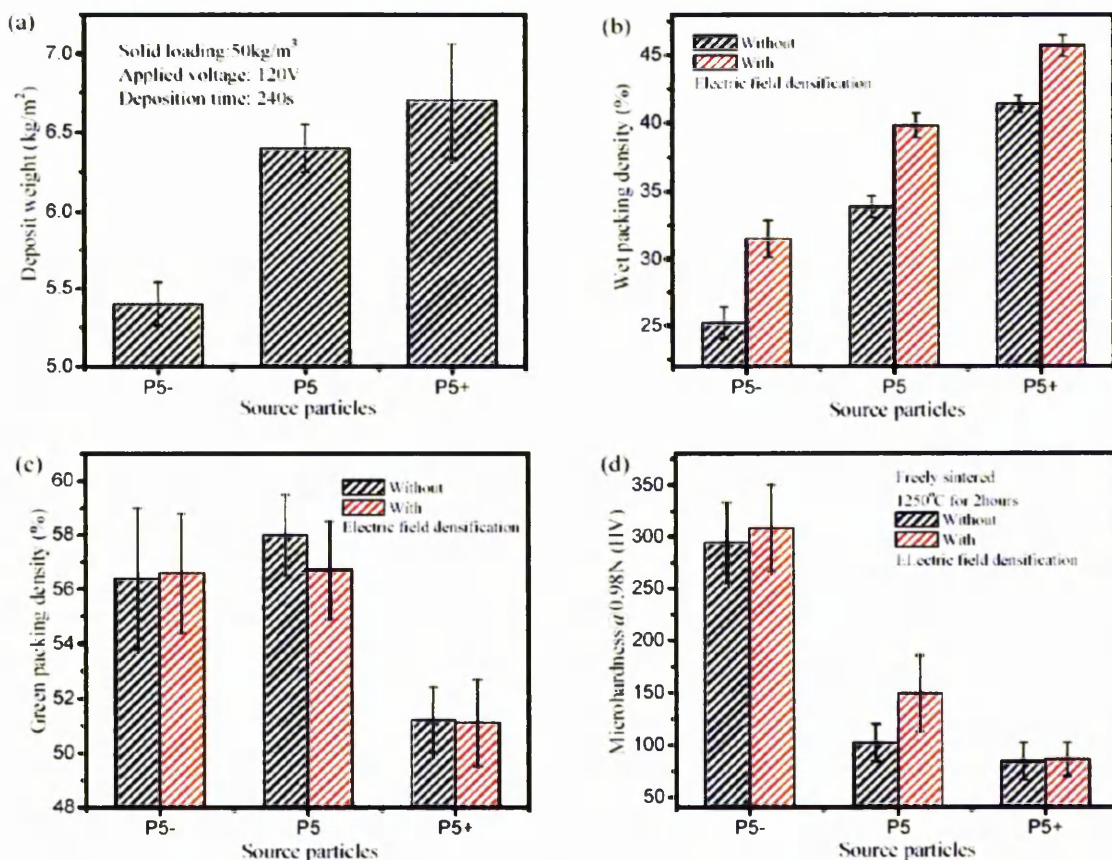


**Figure 5.10 EPD of centrifuge treated P5 particles (a) deposit weight, (b) wet densities, (c) green densities and (d) hardness of  $1250^\circ\text{C}$  2 hours sintered coatings**

Figure 5.10 (a) shows the deposit weight of EPD coatings fabricated from centrifuge treated P5 particles under certain EPD conditions, and it was found that P5- particles showed lower deposition weight than P5+ particles. By comparing P5- and P5+ to P5, it was seen that P5 coatings, i.e. the mixture of small (P5-) and large (P5+) particles, had an intermediate

deposit rate. Figure 5.10 (b) shows the wet packing densities of coatings with centrifuged particles and their responses to the electric field densification. It can be found that P5- showed a lower wet packing density and a more significant difference on wet coating densities caused by the electric field densification than P5+. P5 coatings showed an intermediate wet packing density. Green densities of P5- and P5+ coatings were shown in Figure 5.10 (c). Green densities of coatings with mixed sized particles (P5 coatings) were higher than those of coatings fabricated from centrifuged particles (P5- coatings and P5+ coatings) with relatively narrower size distributions. Studies and researches have been done on effects of mixtures on bulk densities of compacts <sup>[35-39]</sup> and results showed that mixed sized particles tended to give higher green densities, because small particles can fit into the interstices between larger particles. No significant differences were found between coatings with and without the electric field densification on green densities for P5- and P5+ coatings. Figure 5.10 (d) shows the hardness values of freely sintered P5- and P5+ coatings, which indicated that the electric field densification gave less obvious effects on the hardness of sintered coatings for particles with relative uniform sizes (P5- and P5+ particles) than those with broad size distributions (P5 particles). This phenomenon supported the view that the electric field densification had positive effects on the particle packing when there were both large and small particles in coatings.

Figure 5.11 shows SEM images taken from fracture surfaces of P5- and P5+ sintered coatings. Connected networks between small particles were observed in Figure 5.11 (a) and (b), which indicated that P5- particles were small and ready to be sintered under current sintering conditions. So the strength of sintered P5 coatings was mainly attributed to those small sized P5- particles. Whereas there were no such necking networks found in Figure 5.11 (c) and (d), especially around large particles, which meant that large sized P5+ particles were the inert or inactive parts during sintering, and they lowered the hardness of sintered coatings. So the amounts and the positions of small particles in EPD coatings must play important rolls in determining microstructures and mechanical hardness of EPD coatings.

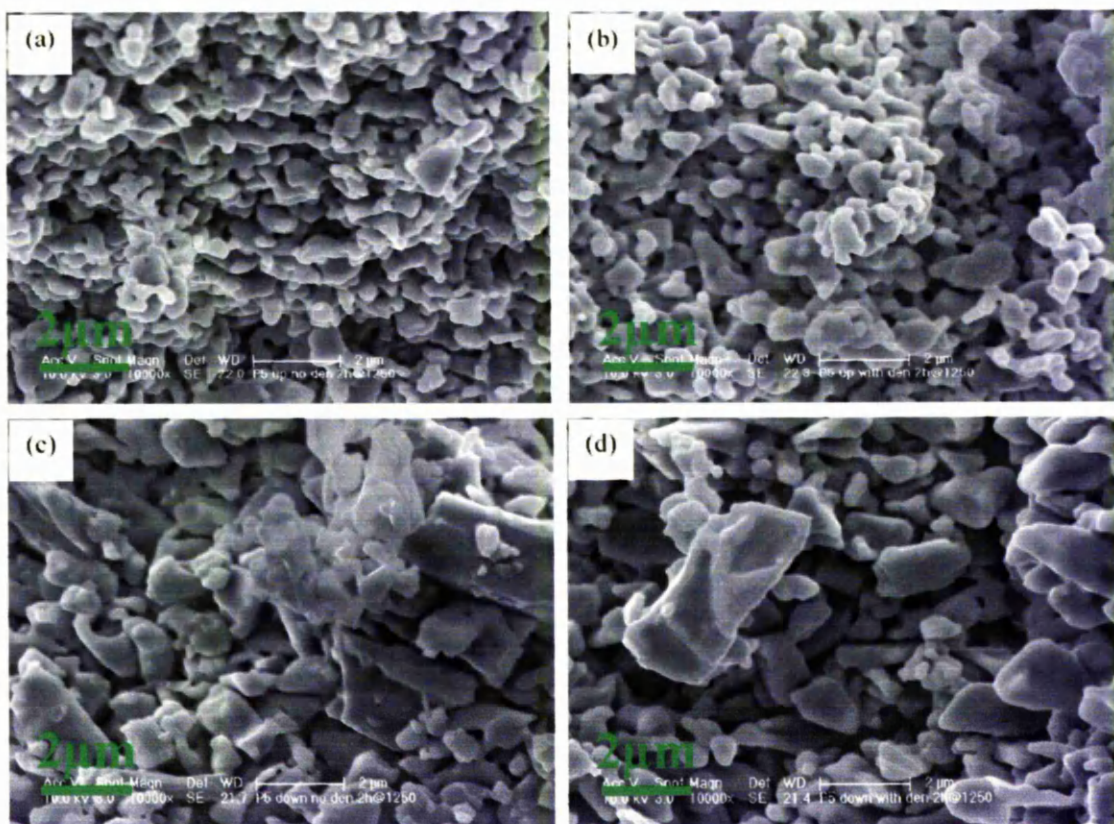


**Figure 5.11 SEM images of fracture surfaces of freely sintered coatings at 1250°C for 2 hours fabricated with centrifuge treated particles: P5- (a) without and (b) with densification; and P5+ (c) without and (d) with densification**

#### §5.2.4 EPD of mixtures of different sized particles

To further understand the effect of the composition of small particles in the EPD coatings on the coating microstructures, P5+ and P0 particles were mixed to prepare suspensions with controlled amounts of small particles (P0) for EPD, because both P5+ and P0 showed similar standard deviation of their size distribution curves and they had significantly different  $a_{50}$  values ( $0.19\mu\text{m}$  for P0 particles and  $1.51\mu\text{m}$  for P5+ particles). The suspensions were prepared for EPD with the same particle concentrations for the three sets of P5+ and P0 mixtures with 25%, 33% and 50% of P0 particles respectively. The results for those EPD coatings from such suspensions are shown in Figure 5.12, and for the point of comparison, corresponding data of coatings fabricated from P5+ suspensions and P0 suspensions were also included in those diagrams.



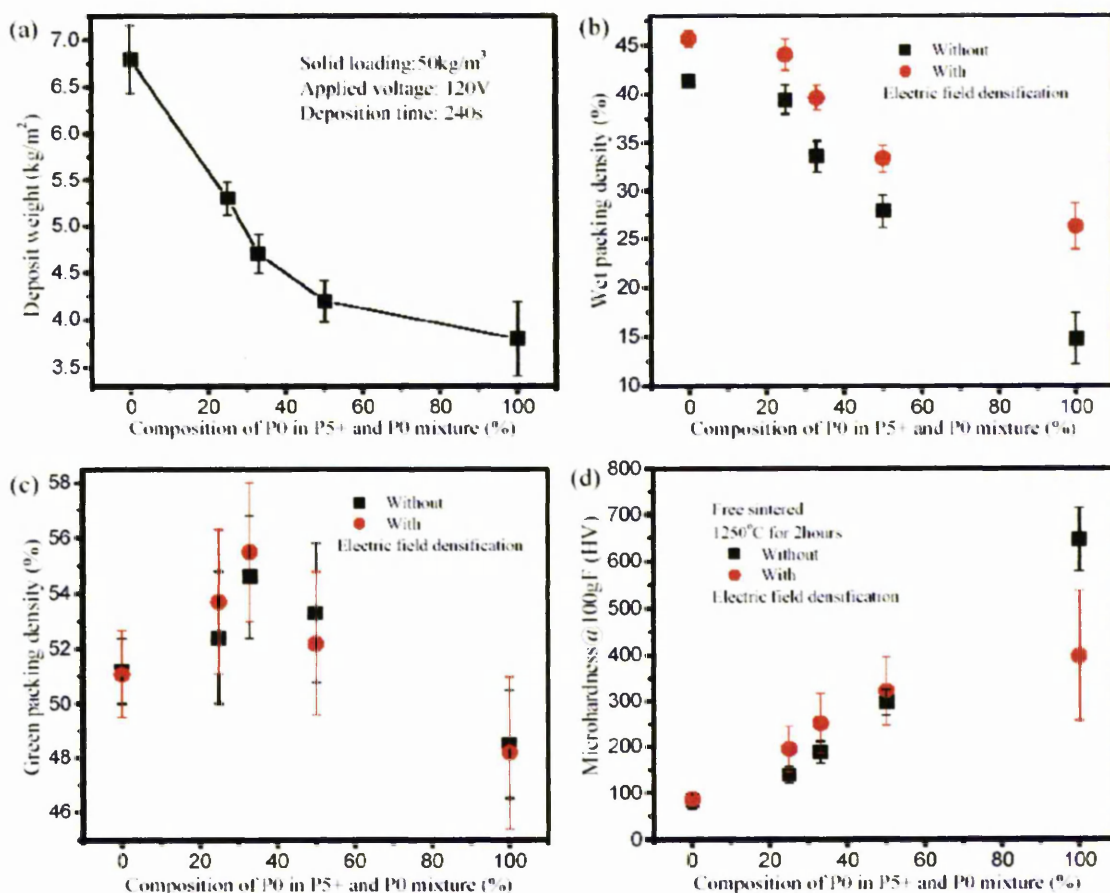
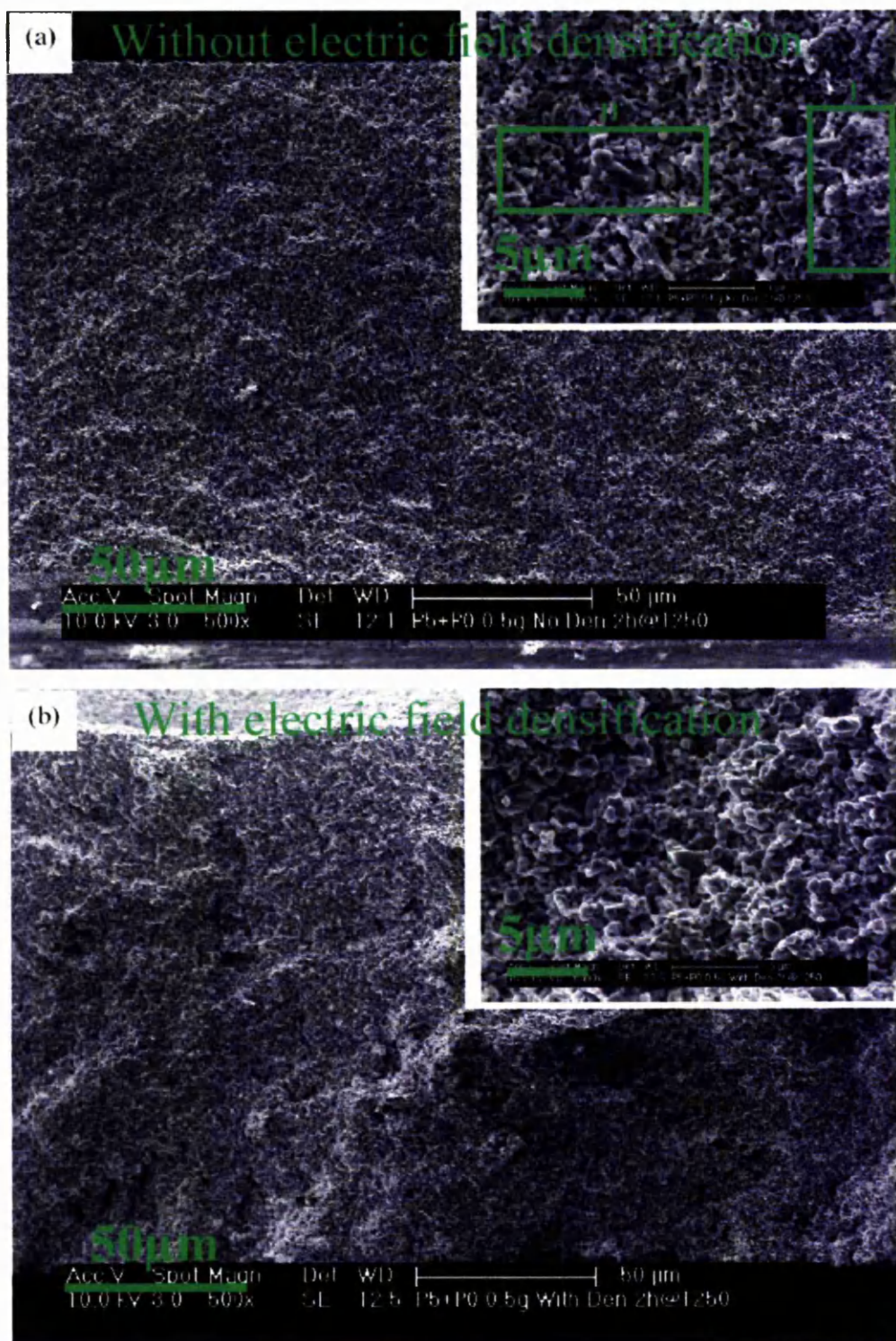


**Figure 5.12 EPD of mixtures of P5+ and P0 particles at various compositions (a) deposit weight, (b) wet density, (c) green density and (d) microhardness of 1250°C 2 hours freely sintered coatings**

Figure 5.12 (a) shows the deposition weight of EPD coatings as a function of the composition of P0 particles in the suspensions, and it was found that by increasing the amount of small particles in the suspensions, the deposition rate decreased, which indicated that small particles lowered the deposition rate during EPD. Figure 5.12 (b) shows the wet packing densities of mixed sized EPD coatings as a function of the composition of P0 particles in the suspensions; the more small particles in the suspension, the lower wet packing densities obtained and the more significant differences on wet packing densities caused by the electric field densification. Figure 5.12 (c) shows variation of green densities of EPD coatings as a function of the fraction of P0 particles in the suspensions. It is worth pointing out again that green densities of EPD coatings fabricated from mixed sized

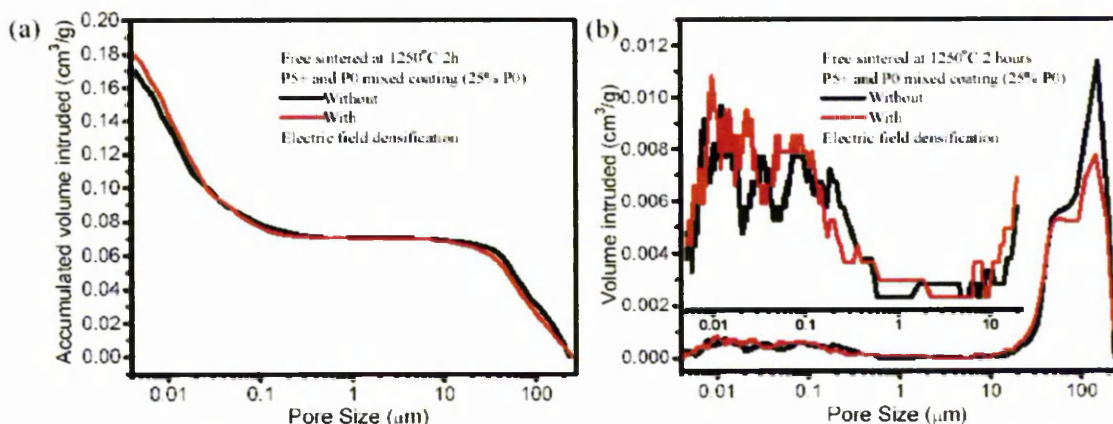
particles were higher than those from uniform sized particles, and when the ratio of the amount of small particles to large particles was 1:2 (33% of P0) in the suspension, the green density of EPD coatings reached the highest value, which implied the most effective particle packing. The electric field densification caused a slight difference in green densities for mixed sized EPD coatings, but no clear trend could be found from the presented green density results. Microhardness of freely sintered coatings was examined to study the function of the amount of small particles in mixed sized EPD coatings. Figure 5.12 (d) shows clearly that microhardness of freely sintered coatings increased with increase of the composition of small particles in suspensions, which indicated that small particles in the coating made the main contribution to the coating hardness after sintering. More small particles provided more connecting necks in the coating and those connecting necks strengthened the coatings and made them show higher hardness values. The electric field densification caused detectable increases of hardness values for freely sintered mixed sized coatings, and the higher hardness of coatings was obtained from the rearrangement of small particles to specific positions (around large particles) in the mixed sized coatings which caused by the electric field densification.

Figure 5.13 show SEM images of fracture surfaces of freely sintered coatings which were fabricated from mixed sized (P5+ and P0 mixture with 25% of P0) suspensions without (a) and with (b) the electric field densification after EPD. A more uniform microstructure with fewer agglomerates was found in Figure 5.13 (a), which represented a normal EPD coating without the electric field densification, than that in Figure 5.13 (b) which reflected the microstructure of coatings with the electric field densification. The uneven microstructures caused by the electric field densification also made relatively large variations of the microhardness values which showed in Figure 5.12 (d).



**Figure 5.13** SEM images taken from fracture surfaces of sintered coatings fabricated from mixture of P5+ and 25% of P0 (a) without the electric field densification and (b) with the electric field densification





**Figure 5.14 Pore size distributions of free sintered P5+ and P0 mixed sized coatings (25% P0) (a) accumulated volume intruded as a function of pore sizes and (b) volume intruded as a function of pore sizes**

More detailed information on the microstructure of coatings was expected from the pore size distribution curves examined by the mercury intrusion method. Figure 5.14 were the measured curves of pore size distributions of freely sintered mixed sized coatings, from P5+ and P0 mixtures with 25% P0, and both normal EPD coatings without the electric field densification and coatings with electric field densification were examined. Figure 5.14 (a) shows the accumulated volume intrusion curves, from which it was found that there were two main intrusion pore size ranges, i.e. pore sizes larger than 10 μm and pore sizes smaller than 1 μm. However, from SEM images, no pores were observed which had sizes larger than 10 μm, so those intrusions were mainly attributed to the gaps between pieces of samples. So only the pore sizes smaller than 1 μm were considered. The total intrusion volumes for both coatings without and with the electric field densification were similar, which represented similar overall porosities in those coatings, which were consistent with the density results shown in Figure 5.12 (c). From the volume intruded curves shown in Figure 5.14 (b), it was found that pores in normal EPD coatings without the electric field densification had three groups of sizes: 1) pores smaller than 0.02 μm, which might represent pores within agglomerates formed by P0 small particles; 2) pores between 0.02 μm and 0.05 μm, which might be formed by those non-agglomerated P0 particles (corresponding to pores in region I highlighted in Figure 5.13 (a)); and 3) pores between 0.05 μm and 1 μm which might be formed around P5+ large particles or inter-agglomerates (corresponding to pores in region II highlighted in Figure 5.13 (a)). Apart from the first

group of pores (smaller than  $0.02\mu\text{m}$ ), the other two groups/peaks of pores shifted to the smaller size direction after the electric field densification, and these pore size changes reflected the rearrangement of particles during the electric field densification.

## §5.3 Discussion

### §5.3.1 Ionic depletion during the electric field densification

The particle packing density of EPD coatings is the most important factor to identify the microstructure of coatings. The results show that the electric field densification after EPD can change the particle packing density of the wet coatings (Figure 5.6 (b), (c) and (d)), and the differences on the particle packing can be detected from the microhardness measurements of freely sintered coatings (Figure 5.9), however no significant changes of the coating densities (Figure 5.7) have been detected. So it is essential to make clear what happened during the electric field densification process.

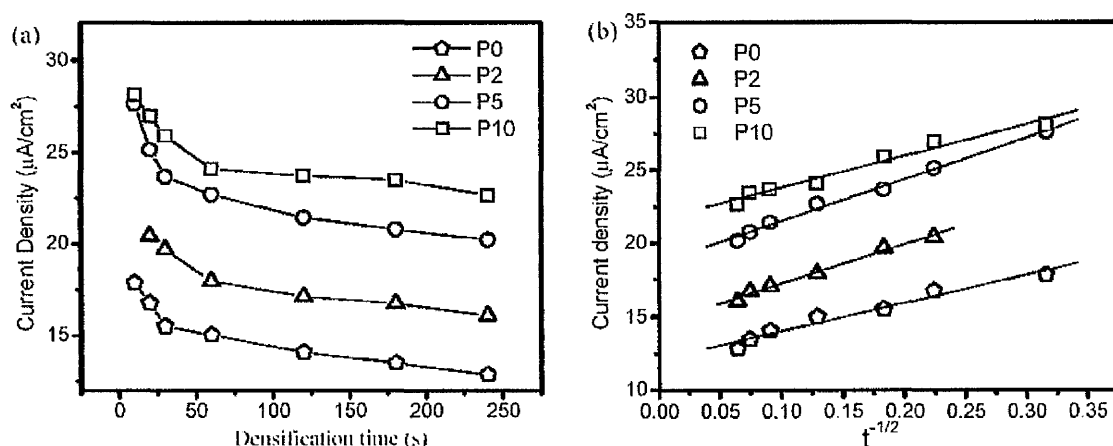


**Figure 5.15** Current densities during electric field densification as a function of (a) densification time and (b) as a function of  $t^{-1/2}$

Changes of the current density during the electric field densification process are recorded to reveal the ionic transportation conditions in the suspensions as well as in the wet EPD coatings. The variations of current density during electric field densification are shown in Figure 5.15 (a). The current density, for all EPD coatings fabricated with four batches of particles, decreased rapidly in the first minute of the electric field densification and after that the current density kept decreasing but with relative lower decreasing rates. Since the



applied voltage (240V) and the electrical conductivity of pure acetylacetone ( $1.95 \times 10^{-5}$  S/m) during the electric field densification are all the same for all those EPD coatings (P0, P2, P5 and P10 coatings), the differences of initial current densities for different coatings are mainly caused by the deposited wet EPD coatings, which may show different electrical conductivity for different sizes. It also reveals that EPD coatings from smaller sized particles, i.e. P0 coatings, have the lowest electrical conductivity, which means that a higher potential drop may be induced by the wet coatings fabricated with smaller sized particles.

The Cottrell equation (Equation 5.1) can be used to explain the current density results. The Cottrell equation is effective when an electrode reaction is diffusion controlled, so if the current density and the electric field densification time obey the equation, it can be determined that the electric field densification process is a diffusion controlled process. The equation can be written as below for a planar electrode <sup>[253]</sup>:

$$i = \frac{NFD_A C_A^0}{(\pi D_A t)^{1/2}} \quad \text{Equation 5.1}$$

where  $i$  is the current density,  $N$  is the number of electrons,  $F$  is the Faraday constant,  $D_A$  is the diffusion coefficient for the species of ion  $A$ ,  $C_A^0$  is the bulk concentration of ion  $A$  and  $t$  is the time in unit "second". For a given system, it can be written as:

$$i = kt^{-1/2} \quad \text{Equation 5.2}$$

where  $k$  is the collection of all constants for a certain system.

The current density showed a linear relation to  $t^{-1/2}$  (Figure 5.15 (b)) which implied that the current flow during the electric field densification is controlled by a diffusion process of the charge carriers in the solvent. It has been discussed in Chapter 4 that the charge carrying ion is  $H^+$  and  $AcAc^-$ . And the cathodic electrode reaction, which maintains the current flow in the EPD cell, is mainly controlled by the local concentration of  $H^+$  near the cathode. The depletion of  $H^+$  at the cathode during the electric field densification process causes the local specific pH increase at the vicinity of the deposition electrode, mainly within the wet

deposit. Particles do not totally lose their surface charges after the deposition, because they are still surrounded by solvent molecules and free ions, and they still have electric double-layers, so the increase of pH within the wet coating during the electric field densification lowers the zeta potential of particles and allow them to further coagulate and cause local agglomeration in the wet deposit.

Particles are not finishing their movements on their first collisions with the electrode or previous deposited particles, but they will rearrange themselves in the deposit under the influence of the electro-osmotic flow induced by the electric field <sup>[27, 28, 41]</sup>. Also the ionic depletion near the electrode (in the deposited wet coating) provides possible conditions, i.e. lowered zeta potential and depressed electric double layer thickness, for particles to approach each other and to form agglomerates. This rearrangement of particles can introduce more contact areas between particles. Small particles are more likely to respond to the electric field densification (Figure 5.6 (b) and (c)), so the particle rearranging processes are schematically illustrated in Figure 5.16.

From another perspective, during the electric field densification, solvation ions can be driven either way in or way out of the wet coatings, to maintain the current flow, i.e. cations ( $H^+$  in this study) move into the coating and anions ( $AcAc^-$  in this study) move out of the coating. The phenomena of the electric field densification also imply that the current transportations in the wet coating by ions are uneven for anions and cations, because less solvent (higher wet coating density) has been detected in the coating after the electric field densification (Figure 5.6 (b), Figure 5.10 (b) and Figure 5.12 (b)), which means that more solvent is driven out than driven into the wet coating during the electric field densification.

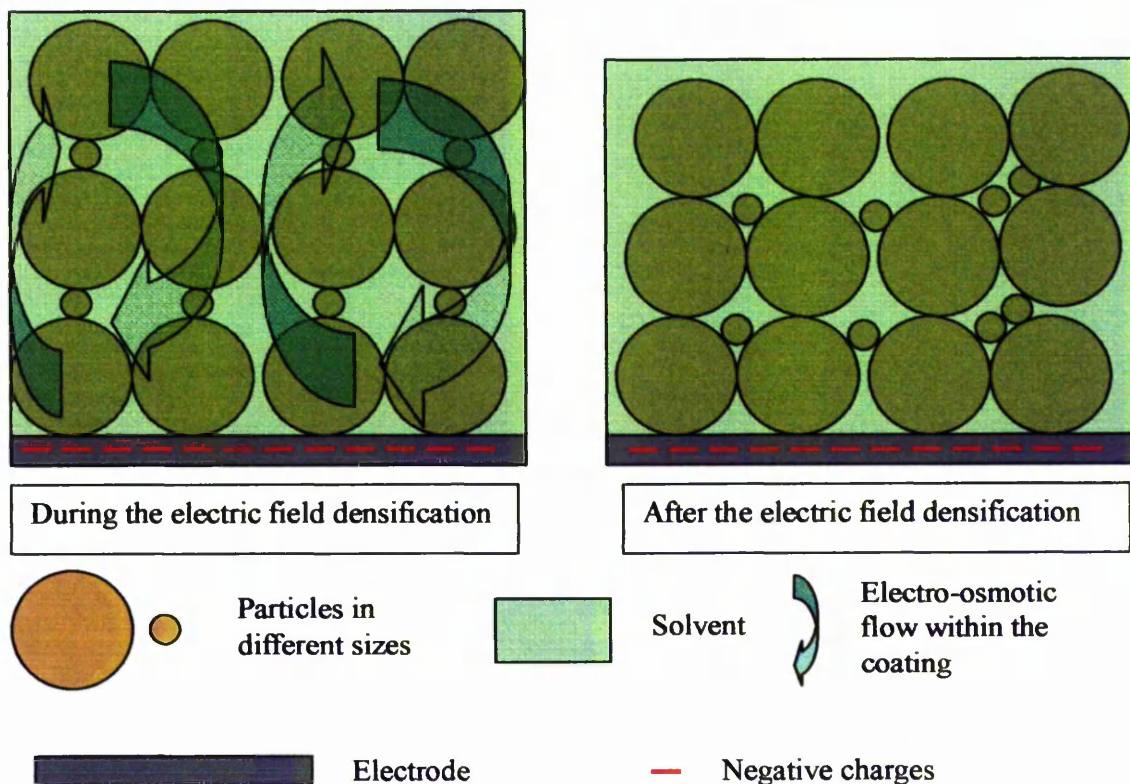


**Figure 5.16 Schematic illustration of the rearrangement of particles within wet EPD coatings during the electric field densification**

### §5.3.2 Particle packing during EPD

Particles in the suspension need to undertake both electrophoresis and deposition to form the EPD coating on the substrate. The velocity  $v$  of the electrophoretic movement in the electric field ( $E_{sus}$ ) is given by <sup>[65]</sup>:

$$v = \mu E_{sus} \quad \text{Equation 5.3}$$

where  $\mu$  is the mobility of suspended particles, which can be described by the Henry equation <sup>[148-152]</sup>:

$$\mu = \frac{2\epsilon_r\epsilon_0\zeta f(\kappa a_p)}{3\eta} \quad \text{Equation 5.4}$$

where  $\eta$  is the viscosity of the solvent,  $\zeta$  is the zeta potential of suspended particles,  $\kappa$  is the Debye constant whose inverse is the Debye length which represents the thickness of the diffuse double layer around the particle,  $a_p$  is the particle size, and the function  $f(\kappa a_p)$  is the Henry's function, which increases from 1.0 at  $\kappa a_p=0$  (Debye-Hückel equation) to 1.5 at  $\kappa a_p=\infty$  (Helmholtz-Smoluchowski equation).  $\kappa$  can be written as:

$$\kappa = \left( \frac{e^2 \sum N_i^0 z_i^2}{\epsilon_r \epsilon_0 k_B T} \right)^{\frac{1}{2}} \quad \text{Equation 5.5}$$

where  $e$  is the electronic charge,  $1.602 \times 10^{-19}$  coulomb,  $N_i^0$  is the bulk concentration of ion species  $i$  having valency  $z_i$ ,  $k_B$  is the Boltzmann constant and  $T$  is the absolute temperature. For specific kind of particles, YSZ in this study, in same solvent (acetylacetone), the value of  $\kappa$  are same for all particles regardless of the particle sizes.  $\zeta$  was measured to be in a quite small range of difference between particles (Figure 5.3 (a)), which can be treated as similar values, so  $\mu$  in Equation 5.4 is only related to  $f(\kappa a_p)$ , which consequently gives higher  $\mu$  values for particles with larger size. This explains the phenomenon of small particles showing lower deposition rate (Figure 5.6 (a), Figure 5.10 (a) and Figure 5.12 (a)).

Studies have been carried on EPD kinetics <sup>[145, 146]</sup> based on Hamaker's initial work, and the particle volume fraction (wet coating density) in the deposit was taken into account by adding a factor  $\left( \frac{\varphi_d}{\varphi_d - \varphi_s} \right)$  into Hamaker's equation <sup>[242]</sup>:

$$\frac{dY}{dt} = \alpha_d \mu E_{sus} C_{sus} S \frac{\varphi_d}{\varphi_d - \varphi_s} \quad \text{Equation 5.6}$$

where  $Y$  is the deposit yield mass in time  $t$ ,  $E_{sus}$  is the electric strength over the suspension,  $C_{sus}$  is the particle concentration in the suspension,  $S$  is the deposit surface area,  $\alpha_d$  is a factor which takes into account that not all of the particles delivered to the electrode are incorporated in the deposit and this factor can only be obtained from a single EPD experiment for each suspension <sup>[242]</sup>,  $\varphi_d$  and  $\varphi_s$  are, the volume fraction of particles in the deposit and in the suspension respectively. For suspensions with same solid loadings ( $\varphi_s$ ), a higher  $\varphi_d$  may cause a lower deposition rate  $dY/dt$ , however, Figure 5.6 (a) shows that

higher deposition rates are observed from larger sized particles, which have higher  $\varphi_d$  values of wet coatings (Figure 5.6 (b)). So it implies that the particle fraction is not the dominant factor for determining the deposition rate for different sized particles.

Charged particles in suspension are surrounded by solvent molecules due to the existence of diffuse double layers, whose thickness is given by  $\kappa^{-1}$  calculated based on the nature of particle surface and the solvent. It has been reported by Sarkar and Nicholson<sup>[13, 243]</sup> that free ions take most of the charge carrying and transporting during EPD and particles perform coagulate on the electrode without necessarily losing all of their surface charges. Particles are still surrounded by double electric layers even after the deposition, though the double electric layers may have been depressed due to surface charge distortion in the electric field<sup>[13]</sup> and the ionic depletion<sup>[243]</sup> in the vicinity of the electrode. The existing double layers around deposited particles in the wet coating build up a potential barrier of the coating<sup>[163]</sup>, which lower the effective electric potential over the suspension ( $E_{sus}$  in Equation 5.6), which is one of the determining factors for the deposition rate. Assuming that both large and small particles have the same double layer thickness, but larger particles tend to build broader channels for the charge transport during EPD because of their geometries, which in turn show a higher electrical conductivity for the wet coatings (Figure 5.15 (a)). So wet deposits fabricated with larger particles have lower potential drops within the deposit ( $E_{dep}$ ), whereas those with smaller particles may form narrower channels for the charge transportation and have higher potential drops across the deposit. So the electric potential drop caused by the deposited wet coating is one of the effective reasons for the difference of deposition rate for different sized particles.

### §5.3.3 Microstructure of freely sintered EPD deposit

EPD coatings show low green density, and the electric field densification process do not give detectable changes on either green or sintered densities (Figure 5.7), whereas the hardness of freely sintered coatings can be affected slightly by the electric field densification (Figure 5.9, Figure 5.10 (d) and Figure 5.12 (d)).

Smaller particles in green compacts sinter more rapidly at a given temperature and can be sintered at lower temperatures than larger particles<sup>[229]</sup>. Positions of small particles in a

green coating with mixed sized particles is one of the factors determining the hardness of sintered coating as proposed in Figure 5.12 (d). Large particles need small particles to bridge them together during sintering to enhance the strength of the overall coating, so it is essential that small particles exist exactly at contacting points between large particles, and the more small particles adhering on large particles the more chances large particles being bridged together and the higher hardness of the overall coating. From the SEM images of those sintered coatings, the micro-packing of small particles adhering on large particles can be found in coatings with densification (Figure 5.8 (d)). A schematic drawing of the particle packing of mixed sized particles in the EPD coating are shown in Figure 5.17, which proposed the possible position arrangements of small particles after the electric field densification.

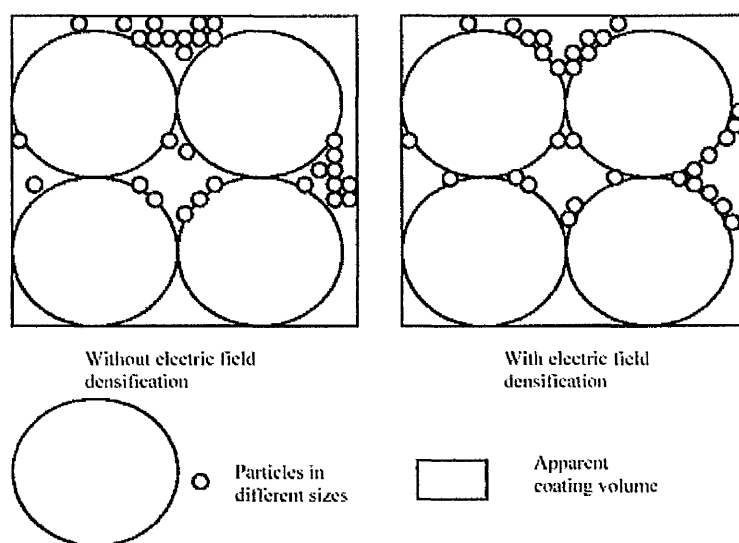


**Figure 5.17 Schematic illustration of green packing of EPD coatings without and with the electric field densification**

The pore size distribution curves (Figure 5.14) provide information on the microstructure of sintered EPD coatings. For coatings fabricated from mixed sized particles, three groups of pores may be formed in the coating: i.e. 1) the pores within the agglomerated small particles (pore sizes  $< 0.02\mu\text{m}$ ); 2) the pores enclosed by well dispersed (non-agglomerated) small particles ( $0.02\mu\text{m} < \text{pore sizes} < 0.05\mu\text{m}$ ), and 3) the pores formed by large particles or between agglomerates ( $0.05\mu\text{m} < \text{pore sizes} < 1.0\mu\text{m}$ ). The electric field densification drives

those non-agglomerate small particles to move either approaching other small particles to form agglomerates or approaching large particles to adhere on their surfaces. Information about these arrangements of non-agglomerate small particles can both be found in the pore size distribution curves (Figure 5.14 (b)). The middle peak of pore sizes ( $0.02\mu\text{m} < \text{pore sizes} < 0.05\mu\text{m}$ ) which represents the pores formed in the coatings produced from EPD without electrical field densification disappears in the coatings produced with application of the electric field densification. Moreover, a group of pores with smaller sizes ( $0.015\mu\text{m} < \text{pore sizes} < 0.035\mu\text{m}$ ) is observed in the coatings produced with the electric field densification, which implies the rearrangement of small particles. In addition, a group of pores between large particles ( $0.05\mu\text{m} < \text{pore sizes} < 1.0\mu\text{m}$ ) in the EPD coating without the electric field densification became smaller ( $0.035\mu\text{m} < \text{pore sizes} < 0.6\mu\text{m}$ ) in the coatings produced with the electric field densification, which suggests that adhesion of small particles onto the surfaces of large particles so that the pore between large particles decreased due to sintering.

### §5.4 Summary

Suspensions of YSZ particles with various particle size distributions in acetylacetone were prepared to study the particle size effects on the microstructural developments of EPD coatings. The pre-treatment of the suspension is essential for preparing well dispersed suspensions, and 5 minutes of ultrasonic treatment is necessary for breaking second-ordered soft agglomerates, which cannot be broken by the mechanical stirring treatment, in suspensions. The YSZ particles with relatively small sizes ( $< 5\mu\text{m}$ ) can be suspended stably in acetylacetone, however, relatively large sized particles ( $> 5\mu\text{m}$ ) are not stable in the suspension. Particles with non-uniform sizes can be separated by centrifuge treatment of the suspension, and particles with relatively uniform sizes can be obtained.

The deposition rate, coating packing densities, including the wet density, green density and freely sintered density, and the hardness of freely sintered coatings showed direct dependence on the particle sizes. Suspensions with smaller particles have lower deposition rates due to the higher potential drop caused by the deposited wet coatings, which lowers the effective electric field strength in the suspension. Mixed sized particles provide higher

green density of EPD coatings than uniform sized particles. The density of EPD coatings after free-standing sintering without substrate constraint is determined by particle size, and the coatings fabricated from smaller particles have higher density. Similarly, the hardness of coatings fabricated from smaller particles is higher than that from larger particles.

The electric field densification in pure solvent after EPD increases the wet coating density due to the electro-osmotic flow within the coating and the ionic depletion in the vicinity of the deposited electrode. The electric field densification is more effective for rearranging of smaller sized particles within the wet EPD coatings. The electric field densification can change the particle packing behaviour, i.e. the positions of small particles in the EPD coating, but have little effect on both green and sintered coating densities. The differences of particle packing caused by the electric field densification are detectable by examining the hardness of sintered coatings. The coating with mono-sized small particles (P0) had lower hardness after the electric field densification because of agglomeration of particles induced by the electric field densification. However, when both small (P0 or P5-) and large (P5+) particles were used to produce the EPD coatings, the electric field densification increased the hardness of sintered coatings by arranging small particles to bridge large particles, therefore promoting sintering.



## Chapter 6 Sintering of EPD Coatings on Metallic Substrates

### §6.1 Introduction

In Chapter 5, EPD coatings have been fabricated using various particles with different size distributions. The particle packing conditions of those coatings have been examined at three main stages during coating formation, i.e. the as-deposited wet coating, the dried green coating and the freely (without substrate) sintered coating. Examining freely sintered coatings may provide a direct reflection on the particle packing and help to identify significant factors during the deposit formation. However, in most real applications EPD coatings need to undergo sintering, whilst attached to their metallic substrates, which may produce significant modifications to the coatings. The effect of this substrate is mainly to retard the densification process of EPD coatings, which originates from two aspects: 1) the difference of thermal expansion coefficient between the substrates ( $11.1 \times 10^{-6} \text{K}^{-1}$  for FeCrAlloy) and the ceramic coatings ( $7.7\text{-}9.6 \times 10^{-6} \text{K}^{-1}$  for YSZ), this difference mainly affects the heating up period due to the mismatch of volume expansion of the coating and the substrate; 2) the rigidity of substrates during sintering, which may constrain the in-plane shrinkage of ceramic coatings and leave only one direction, the thickness, free to shrink. Defects such as cracks and delamination may also occur in the ceramic coating due to the tensile stresses exerted by the substrate during sintering <sup>[254-257]</sup>.

Bordia and Raj <sup>[53]</sup> presented an extreme example of constrained sintering, assuming the substrate perfectly rigid and the coating remaining securely attached to the substrate during sintering. Their analysis showed that the film developed a tensile stress very early in the sintering process. Even though the magnitude of the tensile stress is small (less than a few MPa <sup>[254]</sup>), it may cause cracks to form near pre-existing defects since the stress develops in the early stage of sintering when the coating is porous and weak. These cracks then may either exist as macro pores or some of them may propagate and grow to form failure cracks <sup>[51-53]</sup>. It has been reported that constrained sintered alumina films had limited achievable densities under certain sintering temperatures <sup>[258]</sup>. Pores in constrained sintered films tend to develop anisotropic shapes which have thickness-dependent orientations, and also a

graded pore structure has been observed along the thickness <sup>[46, 239, 258]</sup>. Indentation hardness of constrained sintered YSZ/Al<sub>2</sub>O<sub>3</sub> composite coatings have been measured <sup>[259]</sup> across the coating thickness (up to 120µm thick), and the results revealed a thickness-dependent hardness gradient within the coating, i.e. lower hardness near (within ~30µm range) the coating/substrate interface and higher hardness near the top surface.

In the present chapter, the sintering behaviour, i.e. the mechanisms and the kinetics, of EPD YSZ coatings were studied. The constraint effects of the metallic substrate on the YSZ coating were examined on the coating density, indentation hardness and pore size distribution. The responses of different particle sizes to the substrate constraint during sintering were also identified.

## §6.2 Results

### §6.2.1 Effects of sintering temperature

Sintering temperature is one of the most important conditions for the fabrication of ceramic coatings, especially for coatings on metallic substrates which cannot sustain high temperatures (melting point 1380°C for FeCrAlloy). So it is very important to identify the sintering behaviour of EPD coatings at different temperatures. EPD coatings were isothermally treated, both free and with substrate constraint, and the properties of sintered coatings, i.e. the coating shrinkage, coating density and mechanical hardness were examined.

#### §6.2.1.1 Free sintering shrinkage

The linear sintering shrinkage  $\frac{\Delta L}{L_0}$  is defined as:

$$\frac{\Delta L}{L_0} = \frac{L_0 - L_s}{L_0} \quad \text{Equation 6.1}$$

where  $L_0$  and  $L_s$  are the lengths of the green coating and the sintered coating respectively as shown in Figure 6.1.

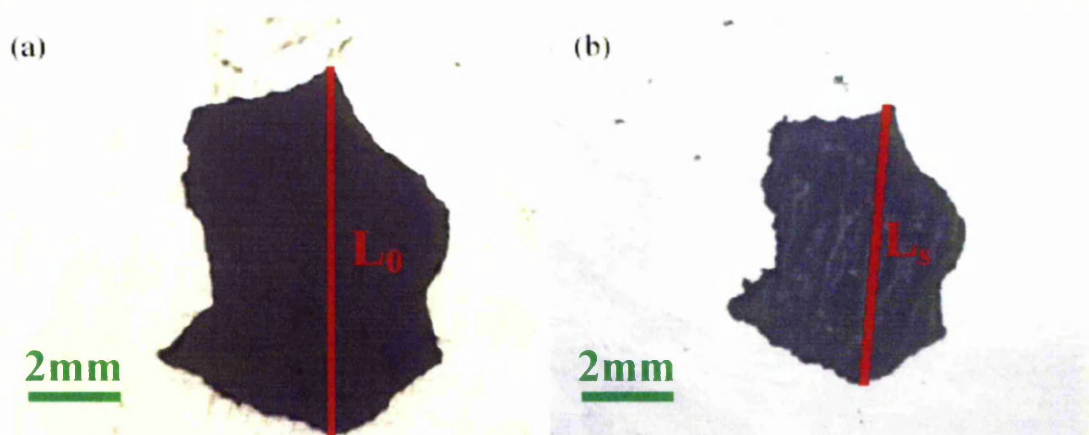


**Figure 6.1** Optical microscope images used to measure the sintering shrinkage of EPD coatings, (a) green coating and (b) freely sintered coating

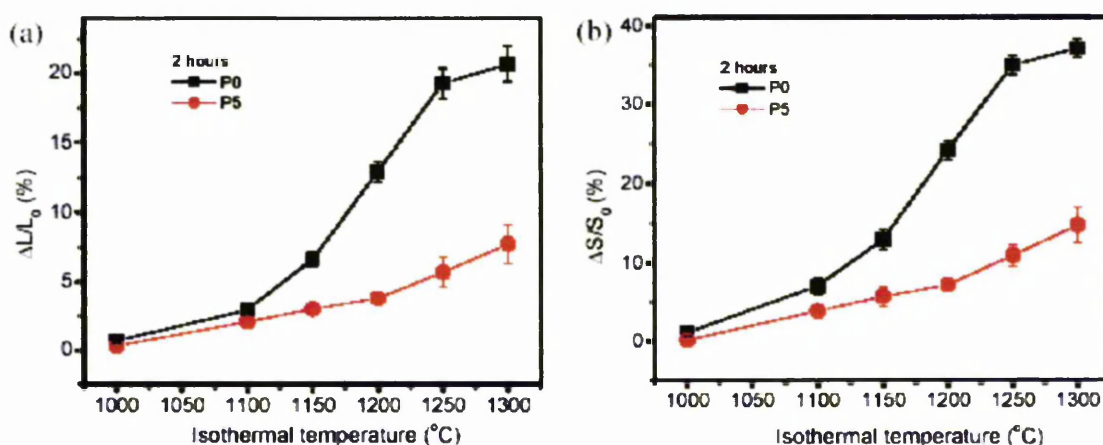


**Figure 6.2** Free sintering (a) linear and (b) in-plane area shrinkages of EPD coatings with P0 and P5 as a function of isothermal temperature.

Figure 6.2 shows the sintering shrinkages of EPD coatings fabricated with P0 and P5 respectively as a function of sintering temperature. It was found from Figure 6.2 (a) that for

P0 coatings,  $\frac{\Delta L}{L_0}$  increased from less than 0.69% at 1000°C to 20.68% at 1300°C. A

significant shrinkage burst was found between 1100°C ( $\frac{\Delta L}{L_0} = 2.94\%$ ) and 1250°C

( $\frac{\Delta L}{L_0} = 19.26\%$ ), which indicated a substantial porosity decrease. When the sintering

temperature increased from 1250°C to 1300°C,  $\frac{\Delta L}{L_0}$  increased from 19.26% to 20.68%, which implied the coating had reached a final sintering stage with very low porosity and pores closing and disappearing. For P5 coatings,  $\frac{\Delta L}{L_0}$  was found to be 0.31% after 2 hours sintering at 1000°C, and it increased almost linearly to 7.76% when the sintering temperature was 1300°C. There was no obvious shrinkage burst for P5 particles observed up to 1300°C unlike P0 particles. This was due to the large particle size of P5, which limited the sintering shrinkage, and temperatures higher than 1300°C were out of the scope of the current study considering of the melting point of Fecralloy substrates.

Apart from  $\frac{\Delta L}{L_0}$ , the in-plane surface area shrinkage  $\frac{\Delta S}{S_0}$  were also measured:

$$\frac{\Delta S}{S_0} = \frac{S_0 - S_s}{S_0} \quad \text{Equation 6.2}$$

where  $S_0$  and  $S_s$  are respectively the surface areas of the green coating and the sintered coating, which are measured from image analyzing of pictures shown as in Figure 6.1.

Figure 6.2 (b) shows the results of  $\frac{\Delta S}{S_0}$  as a function of sintering temperature. By comparing the two diagrams, Figure 6.2 (a) and (b), it can be found that the trends were quite similar for corresponding plots, and the values followed the relationship:

$$1 - \frac{\Delta S}{S_0} \approx \left(1 - \frac{\Delta L}{L_0}\right)^2 \quad \text{Equation 6.3}$$

which indicated that the coating shrinkage was isotropic for the in-plane directions, and more over it reflected a uniform particle packing of the EPD coatings.

To investigate the sintering time effect on the coating shrinkage, longer isothermal sintering experiments, up to 40 hours, were carried out at 1100°C and 1150°C, since the transition from initial to intermediate stage sintering accompanied by a significant sintering rate

difference was expected around these temperatures for P0 coatings. Figure 6.3 shows the sintering time effect on coating shrinkage for P0 and P5 coatings, and also the shrinkage rates evaluated from these results using:

$$K_s = \frac{\left(\frac{\Delta L}{L_0}\right)_{40h} - \left(\frac{\Delta L}{L_0}\right)_{2h}}{40 - 2} \quad \text{Equation 6.4}$$

where  $K_s$  is the linear shrinkage rate at certain temperatures.

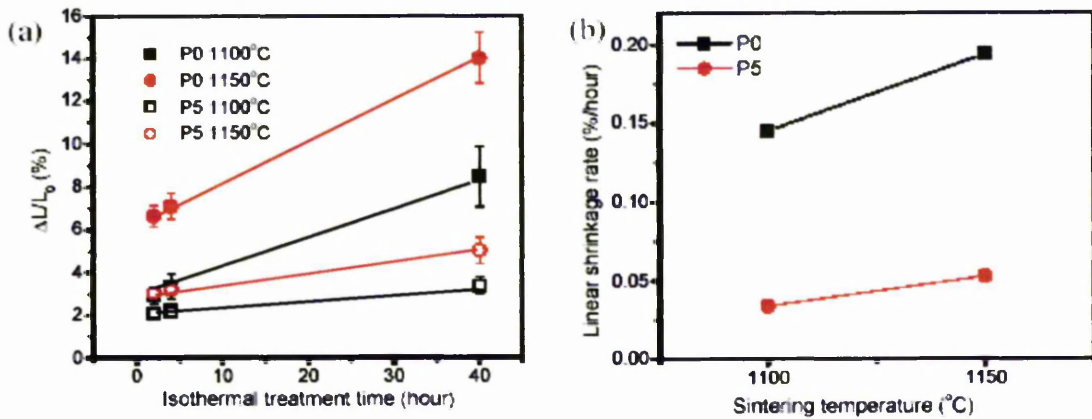


**Figure 6.3 Effect of sintering time on the linear shrinkage (a) of EPD coatings with P0 and P5 and (b) the shrinkage rate change with temperature.**

Figure 6.3 (a) shows a linear increase of  $\frac{\Delta L}{L_0}$  as a function of sintering time, where indicated that when coatings were sintered for long time (up to 40h in this study) they shrink at a constant rate ( $K_s$ ). Figure 6.3 (b) shows  $K_s$  values as a function of sintering temperature. It can be found that  $K_s$  increases with increase of sintering temperature. Higher temperatures and smaller particle sizes gave higher  $K_s$ .

#### §6.2.1.2 Sintered coating density

The coating shrinkage ( $\frac{\Delta L}{L_0}$ ) provides basic information on the sintering kinetics of EPD coatings, but for more detailed understanding of the microstructure of the sintered coating,

the sintered density should be known. Densities of both freely and constrained sintered coatings were measured and calculated following the method described in section 3.6.1 and using the Equations 3.6 and 3.7.

Figure 6.4 shows the densities of freely and constrained sintered coatings with P0 and P5 as a function of the sintering temperature. By comparing the density values of freely and constrained sintered EPD coatings, the substrate constraint effect on the coating sintering process can be identified.

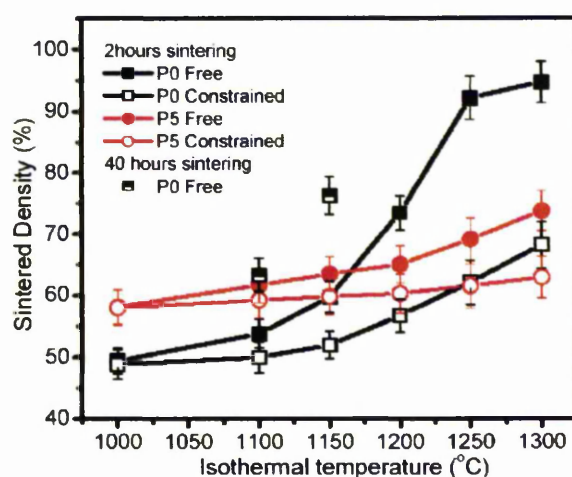


**Figure 6.4 Sintered densities of EPD coatings fabricated with P0 and P5 as a function of sintering temperature (solid dots-freely sintered for 2 hours, hollow dots-constrained sintered for 2 hours, half hollow dots-free sintered for 40 hours).**

In Figure 6.4, for P0 coatings, the green density was 48.5%, and after sintering at 1300°C for 2 hours, the density increased to 94.7% for free sintering, but only 73.8% for constrained sintering, nearly 21% density difference caused by the constraint. However, the most significant density difference between freely and constrained sintering was approximately 30% (92.2% freely and 62.1% constrained) at 1250°C. When the coating was freely sintered at 1250°C for 2 hours, the coating density reached a relative high value (92.2%) due to the high densification/shrinkage rate at that temperature in 3-dimensions, while when the coating was constrained sintered at 1250°C for 2 hours, the coating density was only 62.1% due to the restriction of in-plane shrinkage by the substrate. When the sintering temperature was increased to 1300°C, the densification/shrinkage rate should be

higher than that at 1250°C (derived from Figure 6.3 (b)). The freely sintered density was already high at 1250°C for 2 hours, so the density increase for the freely sintered coating was limited when the sintering temperature increased to 1300°C. However, for constrained sintered coatings, the densification can only proceed in the thickness direction, and the density (62.1%) after 2 hours sintering at 1250°C was still far from the density cap (100%), so when the sintering temperature increased to 1300°C the high densification/shrinkage rate can be fully reflected in the density increase. The densities of long time (40h) sintered P0 coatings are also shown in the diagram, which revealed that after 40 hours sintering at 1100°C and 1150°C, the P0 coatings reached 63.2% and 76.3% relative densities respectively.

For P5 coatings, the green density was 58%, while the freely sintered and constrained sintered densities were 68.1% and 62.9% respectively after sintered at 1300°C for 2 hours. The reduced shrinkage during sintering for larger P5 particles caused a smaller substrate constraint effect. The higher green density for P5 coatings also decreased the possible shrinkage and caused a smaller substrate constraint effect.

### §6.2.1.3 Microhardness

The mechanical hardness of sintered coatings was measured to evaluate the sintering condition and the microstructure of the sintered coatings. Figure 6.5 shows microhardness of P0 and P5 coatings sintered with and without substrates at different temperatures. Very low hardness values (for P0 coatings) or no values (for P5 coatings) were obtained when the sintering temperature was lower than 1150°C. Although sintering shrinkages were observed after 2 hours at 1000°C, 1100°C and 1150°C, which indicated neck formation between particles, the coatings were still very porous and were too weak to withstand the stress of the indentation. With increased sintering time or temperatures higher than 1150°C, coatings began to gain strength and higher hardness values were obtained.

For freely sintered P0 coatings, the hardness increased significantly, from ~40HV<sub>0.98N</sub> to ~780HV<sub>0.98N</sub> when the sintering temperature was increased from 1150°C to 1300°C and it could be attributed to the density increase, from 59.7% at 1150°C to 94.7% at 1300°C. The



freely sintered P0 coatings showed much higher hardness than constrained sintered coatings. Substrate constraint hinders densification during sintering and leaves a more porous coating on the substrate than the freely sintered coating. When the P0 coatings were sintered at 1100°C for 40 hours, the coating hardness was  $\sim 30\text{HV}_{0.98\text{N}}$  (63.2% density), and when the P0 coatings were sintered at 1150°C for 40 hours, the hardness of the coating was  $\sim 114\text{HV}_{0.98\text{N}}$  (76.3% density).

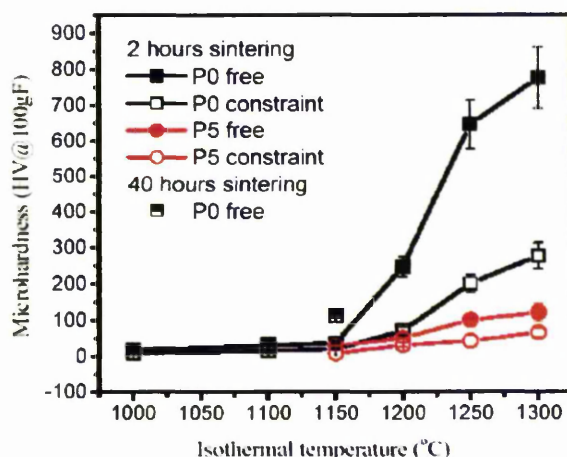


**Figure 6.5 Microhardness of freely and constrained sintered coatings fabricated with P0 and P5 particles as a function of sintering temperature (solid dots-free sintered for 2 hours, hollow dots-constrained sintered for 2 hours, half hollow dots-freely sintered for 40 hours).**

For freely sintered P5 coatings, the hardness increased from  $\sim 30\text{HV}_{0.98\text{N}}$  at 1150°C with density 63.5% to  $\sim 120\text{HV}_{0.98\text{N}}$  with density 73.8% at 1300°C, whereas for constrained sintered P5 coatings, when the sintering temperature increased from 1150°C to 1300°C, the hardness increased from  $\sim 10\text{HV}_{0.98\text{N}}$  to  $\sim 67\text{HV}_{0.98\text{N}}$  with the density varying only from 59.8% to 62.9%. If we compare the freely sintered P5 coating at 1300°C (density 73.8%, hardness  $\sim 120\text{HV}_{0.98\text{N}}$ ) and the freely sintered P0 coating at 1200°C (density 73.4%, hardness  $\sim 250\text{HV}_{0.98\text{N}}$ ), it can be found that when the coating densities were similar, coatings with smaller particle size showed higher hardness after sintering.

The above results imply that apart from the coating densities, other factors such as particle size, necking between particles and coating microstructures also strongly affected the mechanical hardness of the coating.



### §6.2.1.4 Microstructures

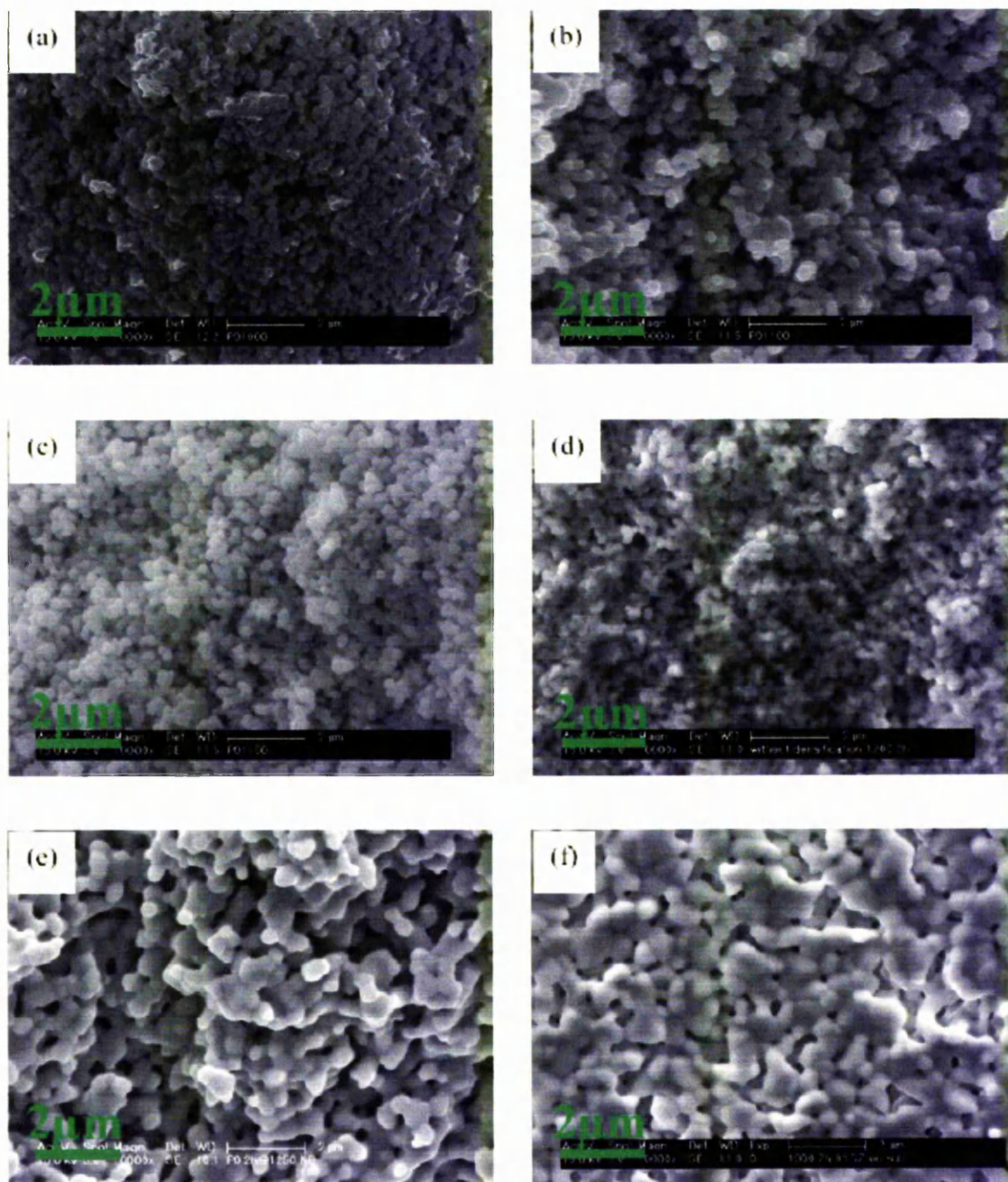


**Figure 6.6 SEM images of fracture surfaces of P0 coatings freely sintered 2 hours at (a) 1000°C, (b) 1100°C, (c) 1150°C, (d) 1200°C, (e) 1250°C and (f) 1300°C.**

Figure 6.6 shows the microstructural development of freely sintered P0 coatings from 1000°C to 1300°C. Up to 1150°C it can be observed that the particle size remained the same

as raw particles, slight necking existed between particles, and there were no significant changes in microstructure of the coatings. At 1200°C, the necking between particles developed extensively, surface smoothing occurred for particles, but no grain growth was observed. When the temperature increased to 1250°C, networks between particles formed and grain growth occurred throughout the coating, and small pores were eliminated. At 1300°C, significant grain growth was observed, and a highly densified structure formed in the coating.

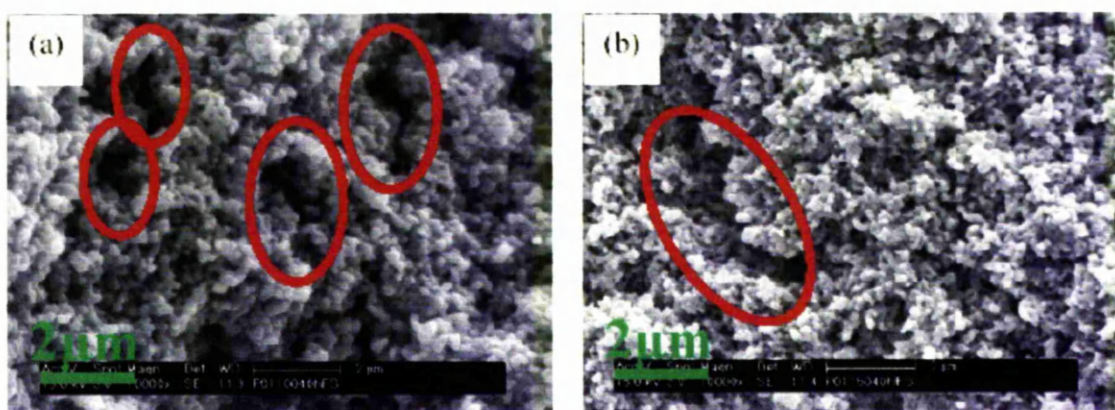


**Figure 6.7 SEM images of fracture surfaces of P0 coatings freely sintered 40 hours at (a) 1100°C and (b) 1150°C.**

Figure 6.7 reveals the microstructures of extended time sintered coatings by observation of the fracture surfaces of the coatings. It can be seen that uneven microstructures developed in the coating when it experiences extended time sintering at a relative low temperature. Specifically micro-crack-like pores (in red circles) implied that there was some inhomogeneous particle packing in the coatings, which was formed during either the deposition or the drying. It was noteworthy that the micro-crack-like pores in coatings after 40 hours sintering at 1100°C were smaller than those in coatings sintered at 1150°C. This is thought to be because the coatings were weaker when sintered at 1100°C than sintered at 1150°C and coatings were likely to form cracks between regions of different sintering rate if they were weak enough.



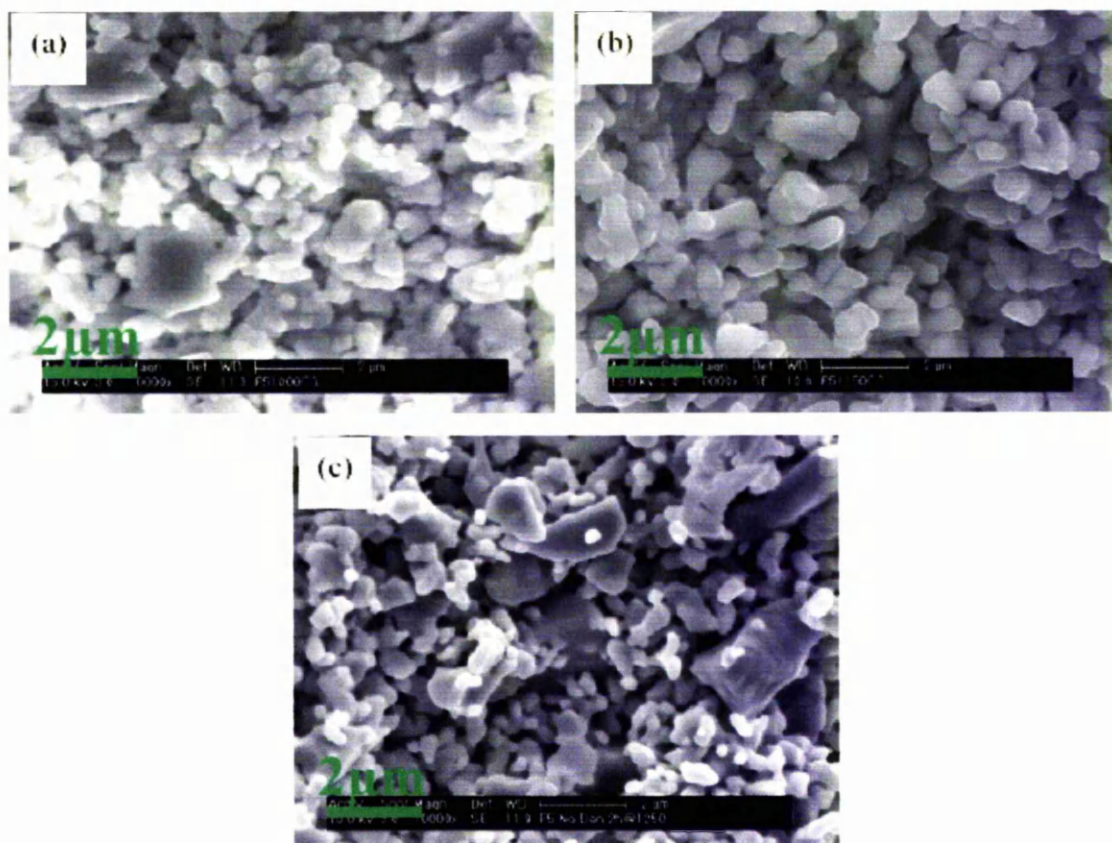


**Figure 6.8 SEM images of fracture surfaces of P5 coatings freely sintered 2 hours at (a) 1000°C, (b) 1150°C and (c) 1250°C.**

Figure 6.8 shows SEM pictures of P5 coating cross-sections after sintering at different temperatures. From the previous shrinkage, density and hardness studies, smaller differences were detected for P5 coatings than for P0 coatings. Response to the sintering temperature was less for P5 than P0 in the range studied (1000°C to 1300°C), and the SEM pictures also showed that in the current temperature range P5 coatings were not sintered significantly. From Figure 6.8 (c), it can be found that smaller particles had formed necks together and also networks of small particles around large particles had formed. Local shrinkage of these networks caused small pores in the coating.

#### §6.2.2 Effects of particle size

The effect of particle size on EPD packing has been investigated in Chapter 5. Particle packing densities were examined in both the wet and green state, and the hardness of freely

sintered coatings was examined to help understand the particle packing mechanism during EPD. This section describes a systematic study into the particle size effects on both the freely and constrained sintering processes. The isothermal temperature was chosen as 1250°C in this section, because at this temperature coatings showed a sensitive response to particle size and sintered coatings attained sufficient strength for the hardness testing.

### §6.2.2.1 Coating density

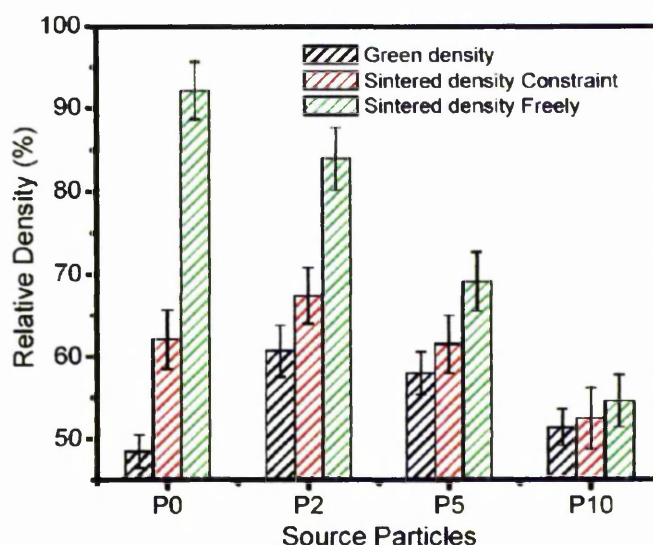


**Figure 6.9 Densities of EPD coatings (green, freely sintered and constrained sintered) fabricated with P0, P2, P5 and P10 particles.**

Figure 6.9 shows the green, freely sintered and constrained sintered densities, of EPD coatings fabricated with various sized particles. Densities of freely sintered coatings showed a large dependence on particle size, the increase of particle size caused a significant decrease of the freely sintered density. If we take the smallest and largest particles as examples, when the average particle size ( $a_{50}$ ) increased from 0.19 $\mu\text{m}$  (P0) to 1.23 $\mu\text{m}$  (P10), the freely sintered density decreased from 92.2% to 54.6%. When the coatings were sintered on the substrates, the sintered densities showed more dependence on the green density. For instance, P0 coating presented 62.1% constrained sintered density because of its low green density (48.5%), whereas P2 coatings showed 67.4% constrained sintered density due to its high green density (60.7%).



§6.2.2.2 Microstructures

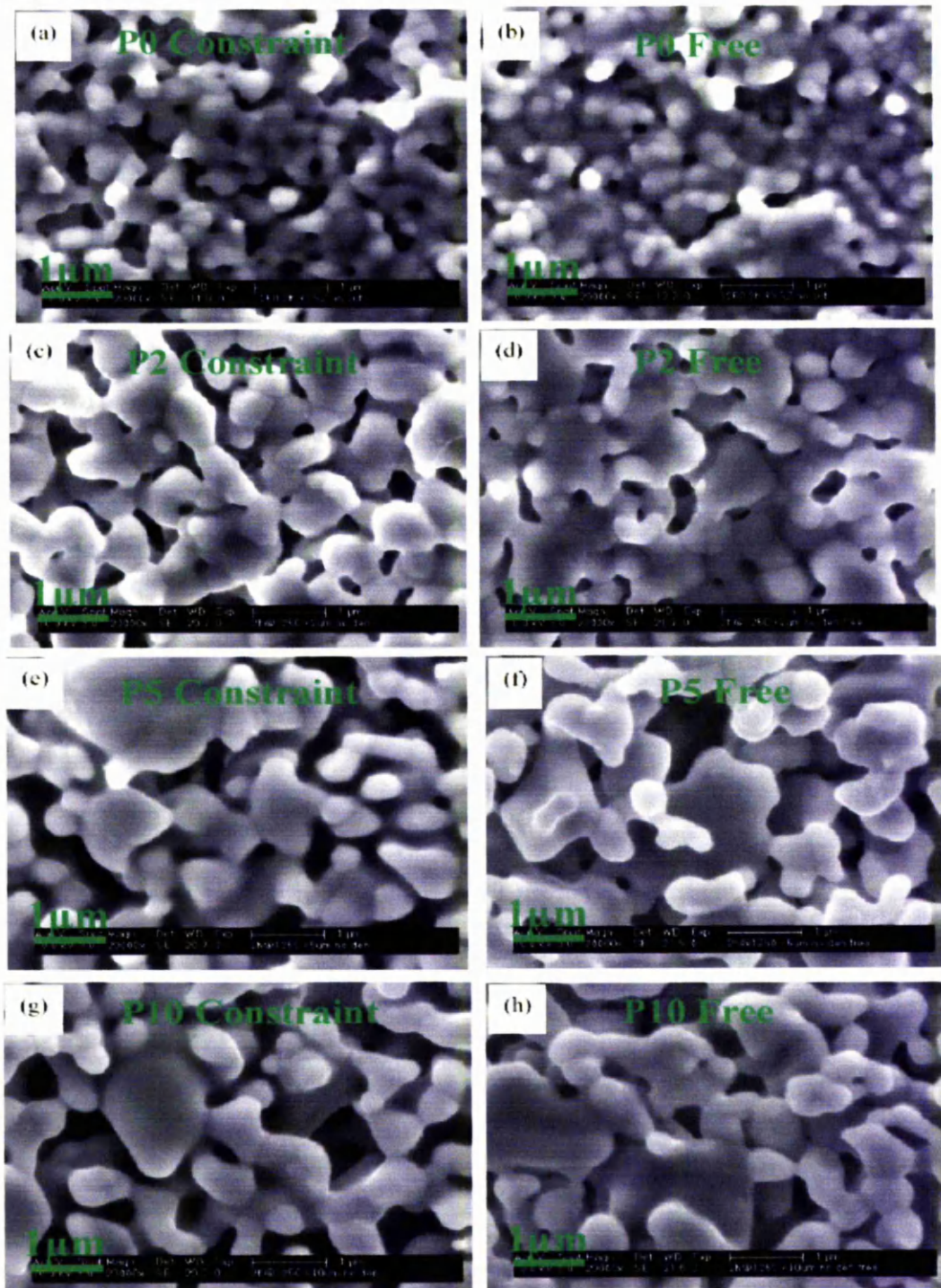


**Figure 6.10 SEM images from top surfaces of sintered (1250°C for 2 hours) EPD coatings fabricated with different sized particles, comparison of constrained sintered coatings (a), (c), (e) and (g), and freely sintered coatings (b), (d), (f) and (h).**

Figure 6.10 shows direct observations of the top surfaces of sintered EPD coatings, the freely and constrained sintered coatings were compared for coatings fabricated with various sized particles. Quite obvious microstructural differences were found for P0 and P2 coatings, in which the freely sintered coatings showed significantly denser structures than the constrained sintered coatings. For P5 and P10 coatings there was no obvious difference between freely and constrained sintered coatings from the SEM pictures, because all of these coatings appeared quite porous. This indicated that less sintering was achieved in coatings fabricated from relatively large particles. Necking between particles was formed in all the coatings, and bridging around large particles was set up by small particles after sintering.

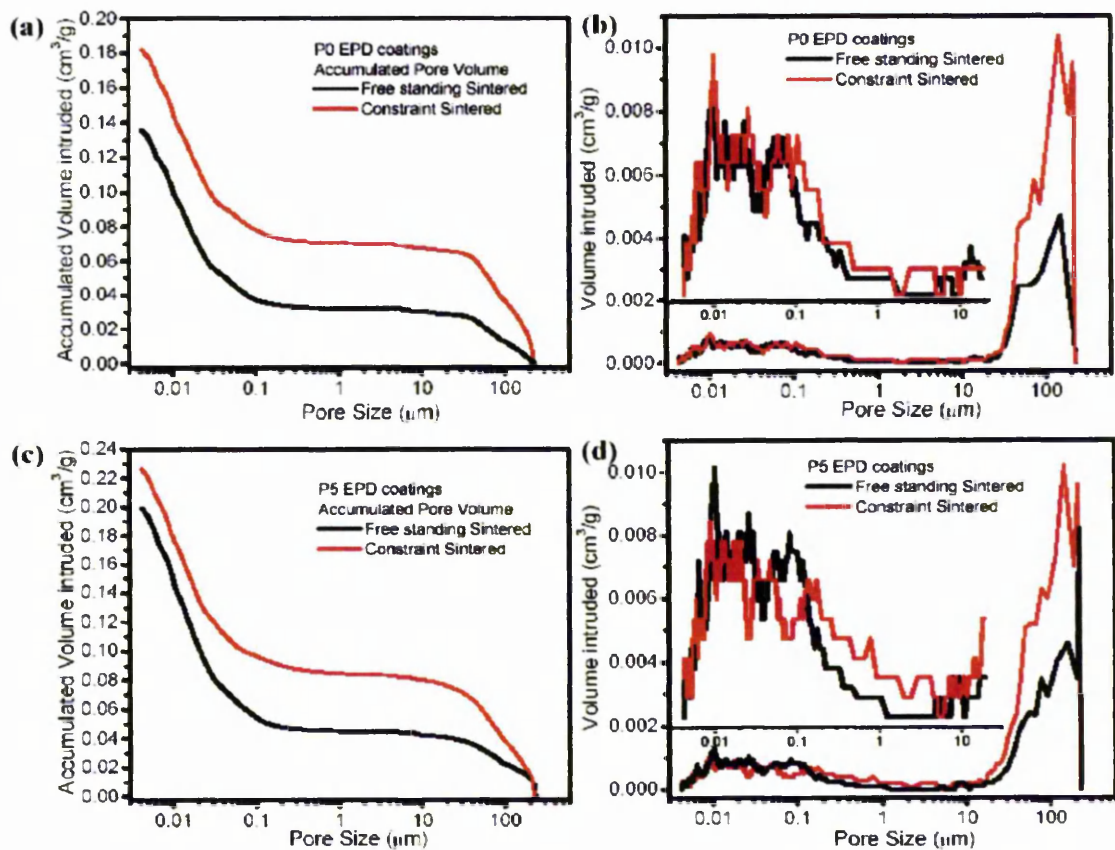


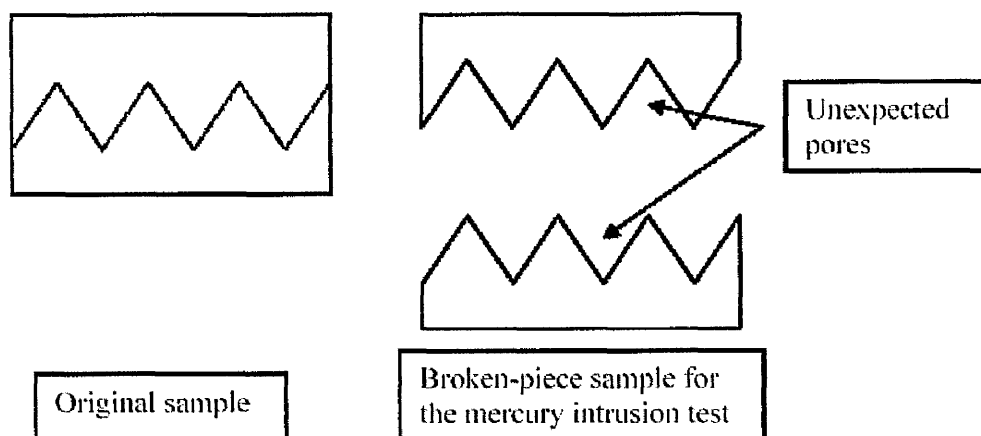
**Figure 6.11** Pore size distributions of constrained and freely sintered EPD coatings: (a) P0 and (c) P5 are accumulated pore volumes as a function of pore size; (b) P0 and (d) P5 are pore volume intruded as a function of pore size.

Pore size was quantified by mercury intrusion of sintered coatings, and the results are presented in Figure 6.11. From the accumulated volume intruded value (Figure 6.11 (a) and (c)), the coating densities were calculated and the results are shown in Table 6.1.

**Table 6.1 Densities of freely and constrained sintered coatings via different methods**

Density (%)	P0		P5	
	Freely	Constrained	Freely	Constrained
Mass & Volume	92.2	62.1	69.1	61.5
Mercury intrusion	54.9	47.6	45.3	42.2

The mercury intrusion measured density appeared to be much lower than the mass and volume values. The values measured by mercury intrusion were not consistent with shrinkage results, hardness and SEM observations, so there may be some unexpected factors affecting the mercury intrusion measurement. We attributed the lower density measured to the samples prepared for mercury intrusion which consisted of small flakes. Such samples may introduce extra gaps between pieces, which may be detected as pores by the equipment or surface roughness may be detected by the equipment as pores (Figure 6.12).



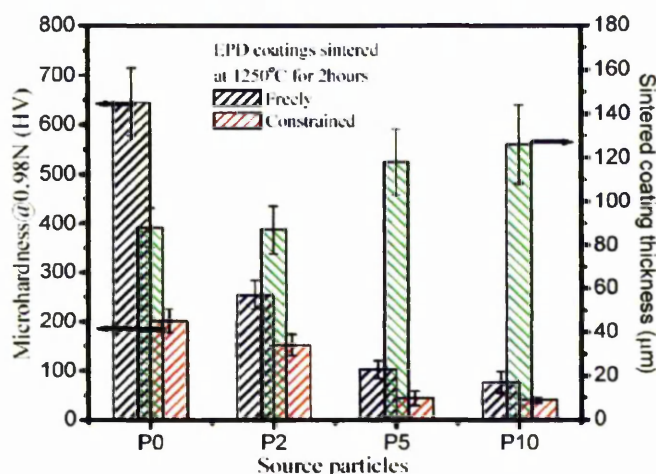
**Figure 6.12 Schematic illustration for the unexpected pores detected during the mercury intrusion density measurement.**

Figure 6.11 (b) and (d) revealed the pore size distributions of freely and constrained sintered P0 and P5 coatings. From the enlarged diagram showing the pore size distributions in the pore range from 0.001-10 $\mu$ m, three groups of peaks can be found: 1) the first group is



pores less than  $0.03\mu\text{m}$  which may be formed by the sintering of particles within agglomerates and the necking joints between particles; 2) the second group of pores is larger than  $0.03$  and smaller than  $1\mu\text{m}$ , this group pore sizes are comparable to the particle size, which may be formed by the packing of dispersed non-agglomerated particles; 3) the third group pores with size larger than  $1\mu\text{m}$  should be treated as micro-cracks. In Figure 6.11 (b), which shows the pore size distributions for P0 coatings, it can be seen that the first two groups of pore size peaks for constrained sintered coatings showed a shift to larger pore sizes compared to those for the freely sintered coatings, which meant a larger pore size in the constrained sintered coatings. This can be attributed to the retardation of sintering caused by the substrate constraint. A small amount of micro-cracks were detected for constrained sintered coatings, shown by a small peak between  $2\mu\text{m}$ - $5\mu\text{m}$ . In Figure 6.11 (d), which shows the pore size distributions of P5 coatings, an interesting 3-peak pore size distribution can be found, which in turn from left to right was attributed to: the nano-pores in the sintered agglomerates formed by the necking joints between small particles; the pores formed between other non-agglomerated relatively small particles; and the pores formed around relatively large particles. In all, the 3-peak distribution can be considered to arise from the broad size distribution of P5 particles.

### §6.2.2.3 Microhardness



**Figure 6.13 Mechanical hardness of constraint sintered EPD coatings with different sized particles, and comparison to freely standing sintered coatings**



Mechanical hardness is a characteristic of solid material expressing its resistance to permanent deformation. For sintered coatings, necks formed between particles during sintering increases the coating hardness. In Chapter 5 hardness of freely sintered coatings was measured to evaluate the particle size effect on particle packing in EPD coatings. However, only freely sintered coatings were considered in Chapter 5, so the response of various particle sizes to sintering constraint was quantified by hardness values in this section.

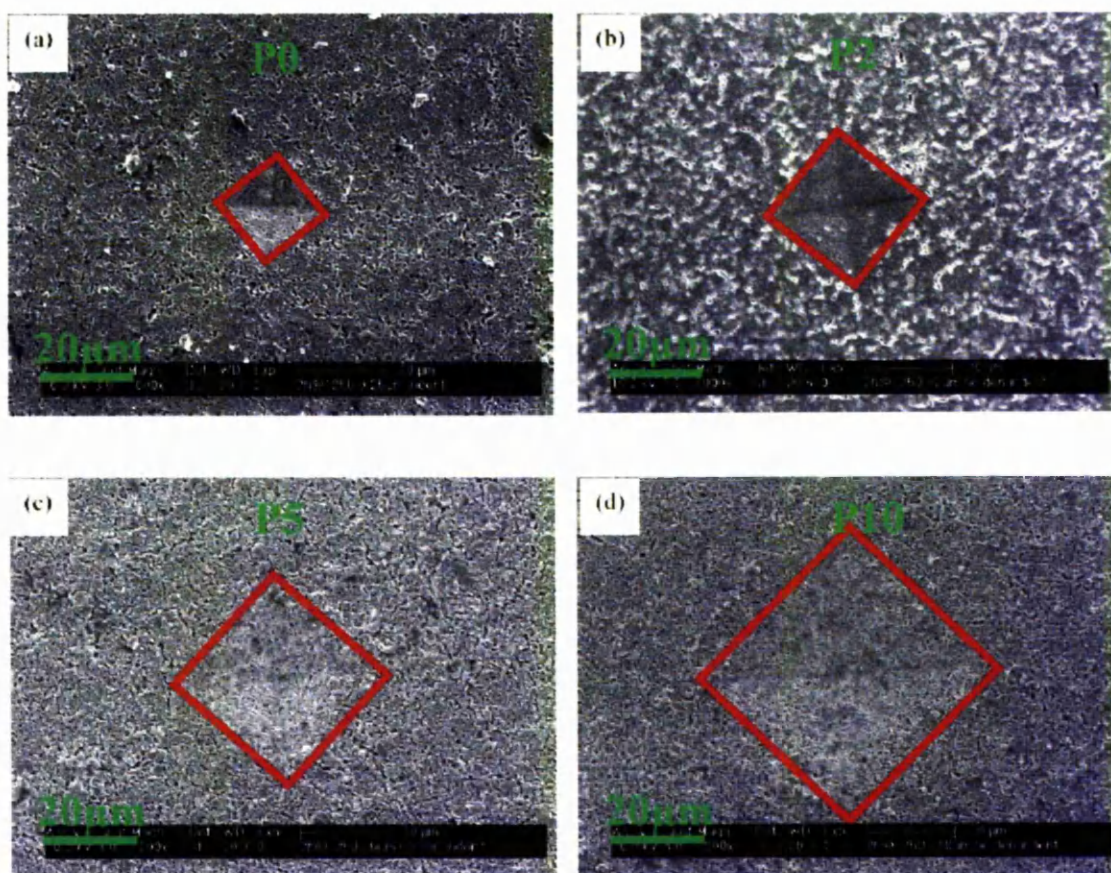


**Figure 6.14 SEM images of micro-indentations (@0.98N load) on top surfaces of constraint sintered EPD coatings fabricated from various particles**

Figure 6.13 plots the hardness value of freely and constrained sintered coatings with different sized particles. The hardness decreased when particle sizes increased for both sintering approaches, which indicated that large particles were hard to sinter and impart poor mechanical hardness to the coatings. The substrate constraint effect on hardness

decreased with increasing particle size, which is shown by the difference in hardness value between freely and constrained sintered coatings. For example, if we take the two extreme cases examined in this study, P0 (smallest) and P10 (largest), the hardness decreased significantly from  $\sim 650\text{HV}_{0.98\text{N}}$  when freely sintered to  $\sim 200\text{HV}_{0.98\text{N}}$  when constrained sintered for P0 coatings. However, for P10 coatings the hardness changed only slightly from  $\sim 76\text{HV}_{0.98\text{N}}$  to  $\sim 40\text{HV}_{0.98\text{N}}$  when the sintering was switched from freely to constrained.

The typical appearances of indentations on the coatings after testing are shown in Figure 6.14. The size of the indentation was the variable used to calculate the hardness of the coating, large indentation reflects low hardness.

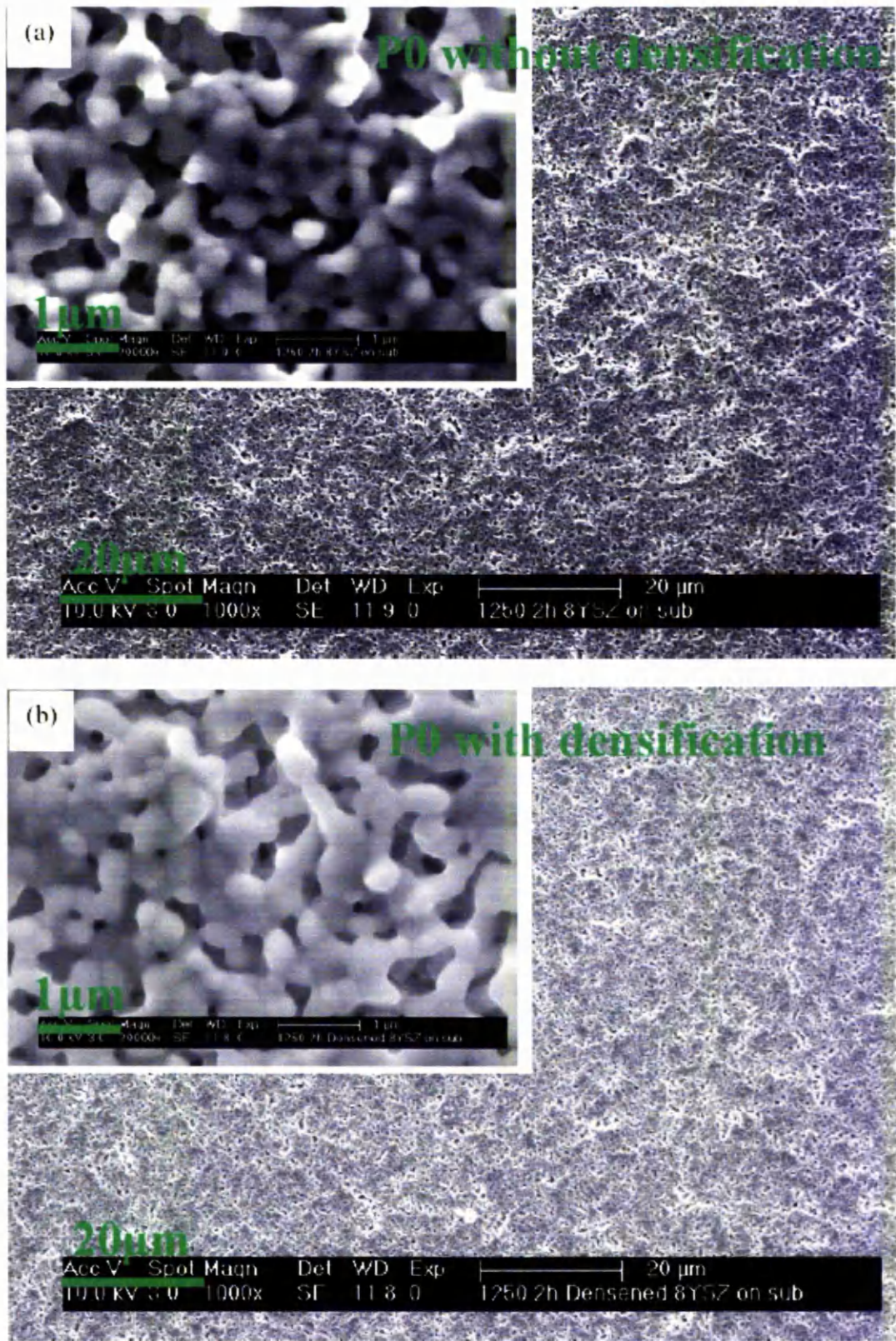
### §6.2.3 Effects of the electric field densification

The electric field densification has been found to be effective at improving particle packing for EPD coatings, when there were both large and small particles in the coatings. How the particle packing changes induced by the electric field densification process will affect constrained sintering has both scientific and applied significance. EPD coatings fabricated with various sized particles were prepared and the electric field densification process was performed immediately after EPD and the coatings subsequently sintered on their substrates at  $1250^{\circ}\text{C}$  for 2 hours. The sintered coatings were characterised by microstructural analysis, pore structure analysis and mechanical hardness measurements. The electric field densification effects were singled out by comparison to identically produced coatings without the electric field densification treatment.

#### §6.2.3.1 Microstructures

SEM images were taken of the top surface of the constrained sintered coatings (P0 and P5) to assess the microstructure (Figure 6.15).







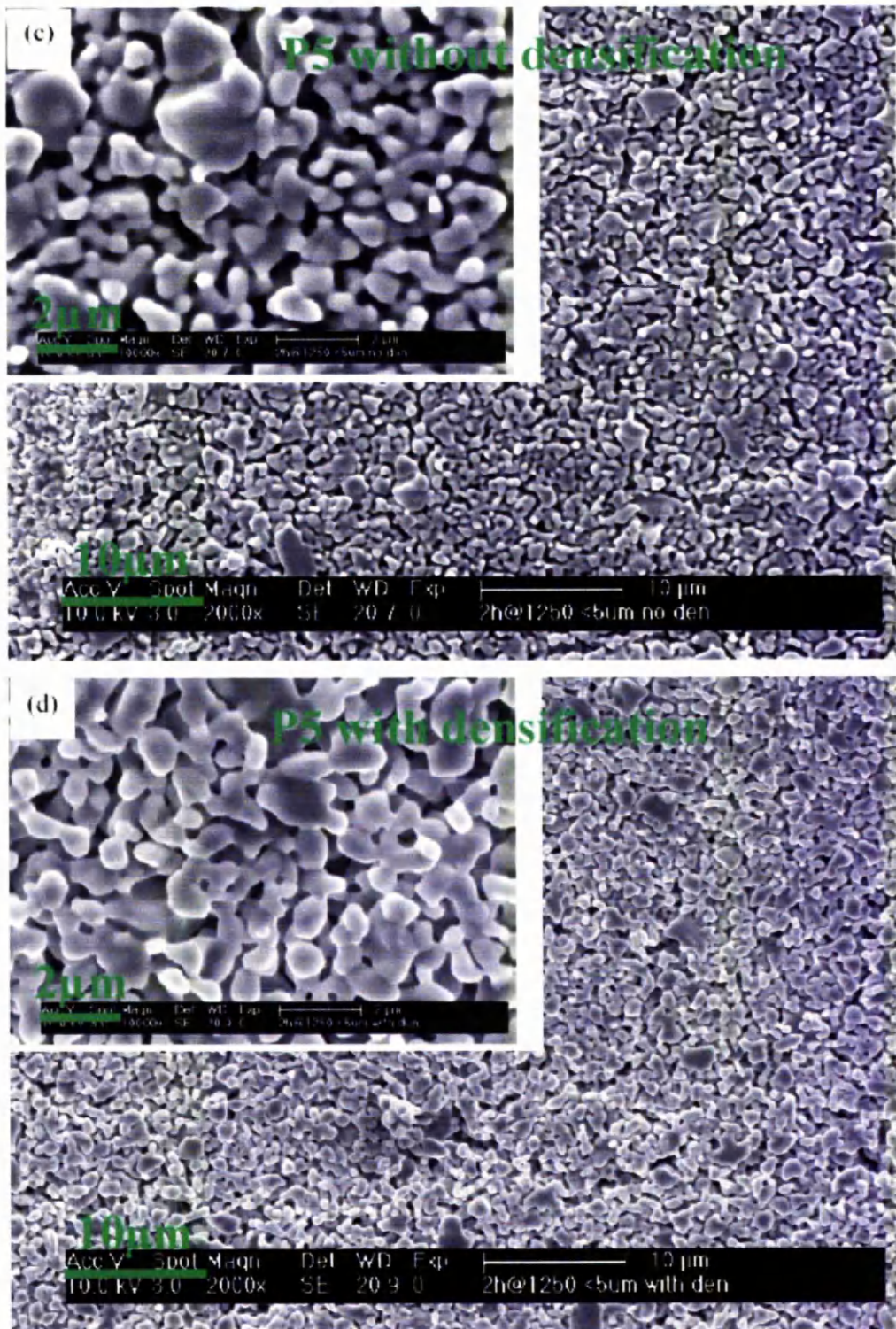
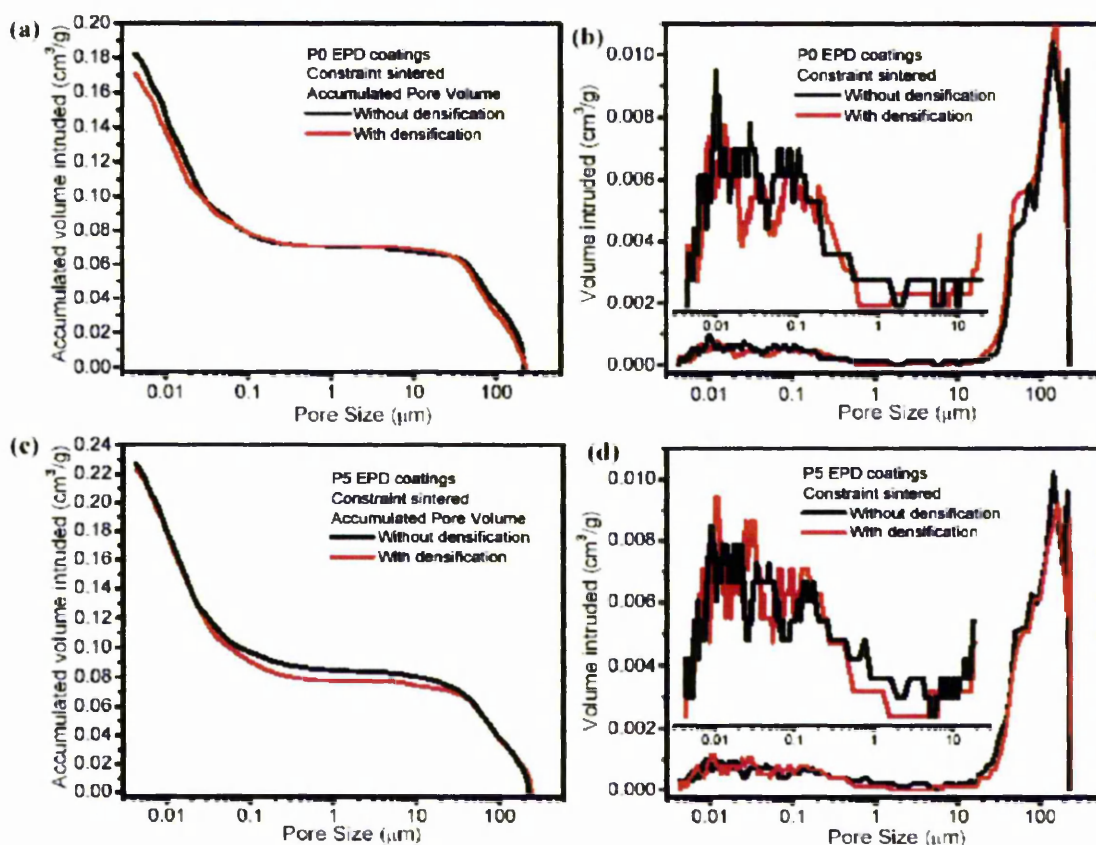


Figure 6.15 SEM images taken from top surfaces of constraint sintered P0 ((a) and (b)) and P5 ((c) and (d)) EPD coatings without and with electric field densification.

By carefully comparing the pictures in Figure 6.15, a slightly less uniform but denser structure can be found for coatings with the electric field densification, although the difference may not be significant. Hence mercury intrusion tests were carried out to examine the detailed pore structure after constrained sintering to confirm the existence of a slight difference caused by the electric field densification process.



**Figure 6.16 Pore size distributions of constraint sintered EPD coatings with and without densification: (a) P0 and (c) P5 are accumulated pore volumes as a function of pore size; (b) P0 and (d) P5 are pore volume intruded as a function of pore size.**

Figure 6.16 shows the mercury intrusion results for constrained sintered coatings with and without the electric field densification treatment. For both P0 and P5 coatings, little difference was detected from the accumulated mercury volume intruded curves (Figure 6.16 (a) and (c)). This indicates that the electric field densification process did not affect the coating porosity much which supports previous measurements on densities of the green and freely sintered coatings.



For constrained sintered P0 coatings, the pore size distributions shown in Figure 6.16 (b) revealed that the electric field densification induced a clear pore peak shifts to larger sizes for pores in the range  $0.01\mu\text{m}$  to  $1\mu\text{m}$ . This implies that the electric field densification process drove small particles to form agglomerates either between individual particles or between individual particles and pre-existing agglomerates in the coating, which explains why the sizes of pores were larger in coatings with the electric field densification than those without.

For P5 coatings, as analyzed in previous sections, three sets of pores were observed: pores smaller than  $0.03\mu\text{m}$  which represented intra-agglomerate pores and joints between particles; pores between  $0.03\mu\text{m}$  and  $0.1\mu\text{m}$  which represented pores formed by relatively small particles; and pores larger than  $0.1\mu\text{m}$  but smaller than  $1\mu\text{m}$  which represented pores around those relative large particles. If taking the pore size distribution of coatings without densification as standard curves, the effect of the electric field densification on the pore structures is described by comparing those specific groups of pores. The main effect of the electric field densification on the pore size distribution can be explained as follows: that the middle group of peaks was split into two parts, with one part shifting to the left and the other to the right. These changes reflected the two main functions of the electric field densification: one was to make small particles unite together to form agglomerates; the other was to make small particles approach the surfaces of large particles. In Chapter 5 it has been found that the electric field densification process affected small sized particles more than large particles. So the pore peak splitting was explained by pores between small particles either getting smaller because of the agglomeration of small particles, which caused the middle peak shift to the left, or rearranging around a large particle and leaving larger gaps behind, which caused the broadening of the third group of peaks.

### §6.2.3.2 Microhardness

Hardness was measured on the top surfaces of the constrained sintered coatings both with and without electric field densification. Coatings made with four types of particle, P0, P2, P5 and P10 were all examined.

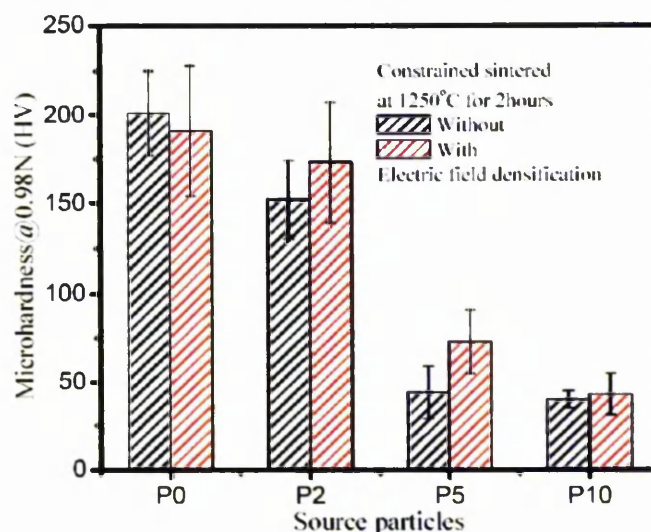


**Figure 6.17 Microhardness of constrained sintered EPD coatings fabricated from different sized particles with the electric field densification.**

The hardness values of constrained sintered coatings with electric field densification are shown in Figure 6.17, and as a comparison, the values of coatings without the densification are also shown. It can be found that how the densification affects the constrained sintered coatings is quite different for different particles.

For P0 coatings, the densification made the coatings weaker than normal EPD coatings as was discovered in chapter 5 for freely sintered coatings, but when the coatings were sintered under constraint, the degrading effect caused by the densification was impaired. This was because the uneven microstructure introduced by the densification of P0 coatings was the dominant factor for the final structure when the coatings were freely sintered, whereas when the coatings were sintered under constraint, the substrate constraint was the dominant factor. Hence the uneven packing caused by the densification caused was overwhelmed by the uneven structure caused by the constraint.

For P2 and P5 coatings, the densification benefited the particle packing and improved the hardness of constrained sintered coatings. For low density coatings made with small and large particles packing together, the coating hardness was mainly determined by the necking formed between particles during sintering, and small particles contribute more neck formation than larger particles, so the position of small particles dominates the final

hardness of the sintered coatings. In Chapter 5, it has been found that for P2 and P5 coatings the densification may form special microstructures with small particles adhered to the surface of large particles which increased the hardness of freely sintered coatings. Here, the densification also increased the coating hardness of constrained sintered P2 and P5 coatings, because the necking was even more important in determining the hardness for the porous constrained sintered coatings.

The electric field densification had little effect on the hardness of P10 coatings, because these particles were so large that no matter what the particle packing little sintering occurred.

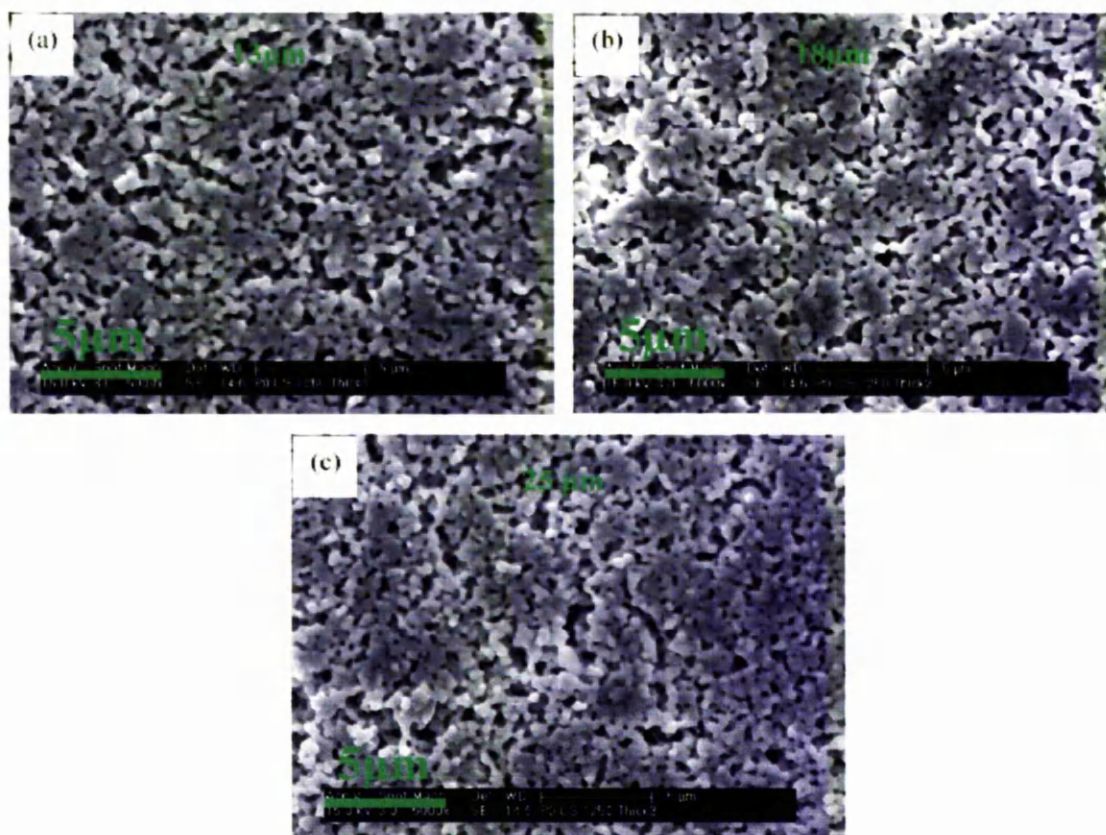
### **§6.2.4 Effects of coating thickness**

Thickness dependent structures of constrained sintered coatings/films have been reported in previous works <sup>[239, 259]</sup>. In this section, a brief examination of the coating thickness effects on constrained sintered coatings was made using microstructure and the mechanical hardness.

#### **§6.2.4.1 Microstructures**

Based on previous results on the constrained sintered coatings, P0 coatings were selected for this investigation, because the microstructural effect of the substrate constraint was largest for P0 particles. To avoid unexpected effects on the microstructures caused by polishing of the cross-sections, the microstructures along the thickness of constrained sintered coatings examined by observing the top surfaces of coatings with stepped increases in thickness using SEM.





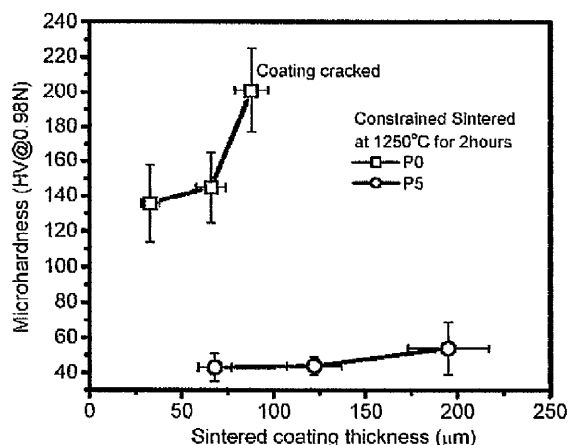
**Figure 6.18 SEM images from top surfaces of constrained sintered P0 coatings with various thicknesses (a) 13μm, (b) 18 μm and (c) 25μm at 1250°C for 2 hours**

Figure 6.18 shows the top surface observations of constrained sintered P0 coatings with the coating thicknesses of 13μm, 18μm and 25μm, which were assumed to briefly reflect the possible microstructure development along the coating thickness. It was found that the coating microstructures of thinner coatings (representing coating structure closer to the substrate) (Figure 6.18 (a)) appeared to be slightly more porous. This agrees with previous reports on the constrained sintering <sup>[46, 239, 259]</sup>.

#### §6.2.4.2 Microhardness

Mechanical hardness of constrained sintered coatings was measured in the same way as the microstructures were examined. Both P0 and P5 coatings with various thicknesses were fabricated and constrained sintered before they were indented from the top surface to test the hardness.

The hard substrates ( $\sim 500\text{HV}_{0.98\text{N}}$  for Fecralloy) could affect the hardness measurements when the coating thicknesses were less than 10 times of the indentation depth (1/7 of the diagonal length) [260]. By referring to the diagonal sizes shown in Figure 6.14, measurements were only made when this criterion was met, i.e. for P0 coatings thicker than  $30\mu\text{m}$  and P5 coatings thicker than  $60\mu\text{m}$ . The hardness values are presented in Figure 6.19.



**Figure 6.19 Microhardness of constrained sintered P0 and P5 coatings as a function of sintered coating thickness.**

For P0 coatings, the hardness increased from  $\sim 136\text{HV}_{0.98\text{N}}$  to  $\sim 145\text{HV}_{0.98\text{N}}$  when the coating thickness increased from  $33\mu\text{m}$  to  $66\mu\text{m}$ . When the coating thickness was further increased to approximately  $88\mu\text{m}$ , the hardness value was measured as  $\sim 200\text{HV}_{0.98\text{N}}$ . Observable cracks were formed for thick coatings ( $>80\mu\text{m}$ ) after sintering, which could be the reason for the abnormal increase of the hardness for thick coatings as less constraint is applied with formation of cracks in the coating.

For P5 coatings, the trend of increasing hardness with thickness was still detectable, though it was less significant than for P0 coatings. The hardness slightly increased from  $\sim 43\text{HV}_{0.98\text{N}}$  measured from around  $70\mu\text{m}$  thick coatings to  $\sim 54\text{HV}_{0.98\text{N}}$  for coatings with thickness of about  $200\mu\text{m}$ .

### §6.3 Discussion

#### §6.3.1 Sintering mechanisms determination and sintering kinetics

For P0 coatings, the observations representing the three sintering stages, i.e. the initial stage, the intermediate stage and the final stage (described in Table 2.3), can be identified from Figure 6.4 and Figure 6.6. The temperature ranges for each stage can be roughly defined as, initial sintering stage from 1000°C to 1150°C, intermediate stage from 1150°C to 1250°C, and final stage from 1250°C to 1300°C, though there may not be sharp transitions between each stage. For P5 coatings, only features representing the initial stage sintering can be identified in the temperature range studied, due to the larger particle sizes.

If it is assumed that the particles are uniform in chemical components and are spherical with unique sizes, the linear shrinkage of the compact during the initial stage sintering is given by <sup>[31]</sup>:

$$\frac{\Delta L}{L_0} = C_j \frac{t^n}{a^m} \quad \text{Equation 6.5}$$

where  $C_j$  is a temperature dependent constant,  $t$  is the isothermal treatment time and  $a$  is the particle size.  $C_j$ ,  $m$  and  $n$  are determined by the sintering mechanisms which are given in Table 6.2:

**Table 6.2 Initial stage sintering parameters for Equation 6.5**

Mechanism	$n$	$m$	$C_j$
Lattice diffusion <sup>[205]</sup>	$\frac{2}{5}$	$\frac{6}{5}$	$\left(\frac{10\gamma_{sv}\Omega D^*}{k_B T}\right)^{\frac{2}{5}}$
Lattice diffusion <sup>[261]</sup>	$\frac{1}{2}$	$\frac{3}{2}$	$\left(\frac{2\gamma_{sv}\Omega D^*}{k_B T}\right)^{\frac{1}{2}}$
Grain-boundary diffusion <sup>[261]</sup>	$\frac{1}{3}$	$\frac{4}{3}$	$\left(\frac{3\gamma_{sv}\Omega D^*}{k_B T}\right)^{\frac{1}{3}}$

where  $\gamma_{sv}$  is the interfacial energy of the solid,  $\Omega$  is the atomic volume of the diffusing species,  $D^*$  is the self-diffusion coefficient for the rate determining species which can be written as <sup>[31]</sup>:

$$D^* = D_0 \exp\left(-\frac{E_{act}}{k_B T}\right) \quad \text{Equation 6.6}$$

where  $D_0$  is the maximum diffusion coefficient at infinite temperature,  $E_{act}$  is the activation energy,  $k_B$  is the Boltzmann constant and  $T$  is the absolute temperature.

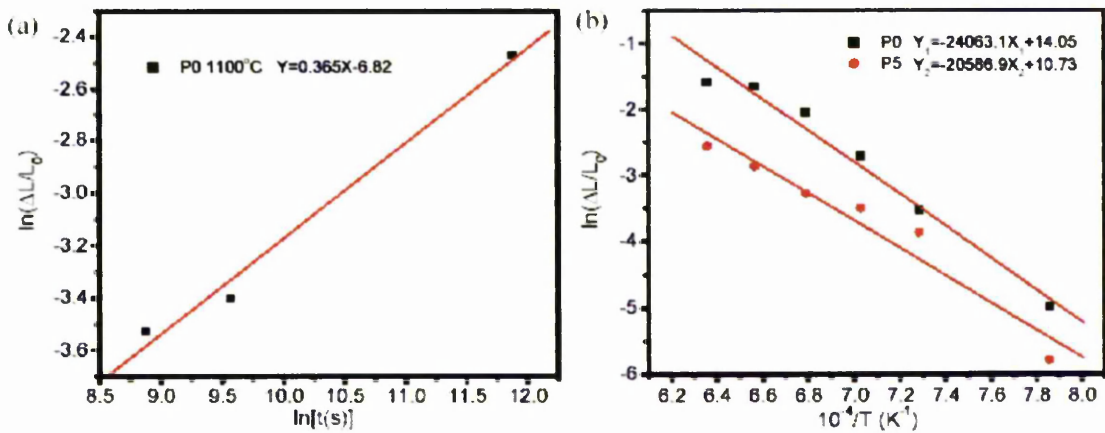


**Figure 6.20 Linear fit of (a) logarithm shrinkage-logarithm time of P0 coatings sintering at 1100°C, and Arrhenius plots of (b) logarithm shrinkage-1/T(K) of both P0 and P5 coatings**

To evaluate the sintering mechanisms of YSZ EPD coatings, the experimental data for P0 coatings at 1100°C for different sintering time (Figure 6.3 (a)) were replotted with logarithmic scales ( $\ln(\frac{\Delta L}{L_0})$ ) in Figure 6.20 (a). Data obtained from P0 coatings was chosen

for the sintering mechanism evaluation rather than those from P5 coatings because the equations are derived with the assumption of uniformly sized spherical particles, which is a closer assumption for P0 rather than P5 particles. The equations are also derived for the initial sintering stage, so the sintering temperature was selected as 1100°C.

The slope of the linear fit of the experimental results of  $\ln(\frac{\Delta L}{L_0})$  against logarithm sintering time,  $\ln t(s)$ , gives the value of  $n$  in Equation 6.5:

$$\ln\left(\frac{\Delta L}{L_0}\right) = n \ln t + (\ln C_j - m \ln a) = n \ln t + C_s \quad \text{Equation 6.7}$$

where  $C_s$  is a constant for a certain system.

By comparing the obtained  $n$ , 0.365 in Figure 6.20 (a), to the values in Table 6.2, the sintering mechanism of P0 coatings can be attributed to grain-boundary diffusion with  $n$  close to  $1/3$ . Once the sintering mechanism has been determined, the appropriate constants in Table 6.2 and together with Equation 6.6 can be substituted into Equation 6.5:

$$\frac{\Delta L}{L_0} = \left( \frac{3\gamma_{sv}\Omega D_0 \exp(-\frac{E_{act}}{k_B T})}{k_B T} \right)^{\frac{1}{3}} t^{\frac{1}{3}} \quad \text{Equation 6.8}$$

Equation 6.8 can be rearranged to form an expression for  $\ln(\frac{\Delta L}{L_0})$ :

$$\ln\left(\frac{\Delta L}{L_0}\right) = \frac{1}{3} \left( -\frac{E_{act}}{k_B T} \right) + \ln(3\gamma_{sv}\Omega D_0) - \ln(k_B T) + \frac{1}{3} \ln t - \frac{4}{3} \ln a \quad \text{Equation 6.9}$$

For a certain system:

$$\ln\left(\frac{\Delta L}{L_0}\right) = -\frac{E_{act}}{3k_B T} + C_s \quad \text{Equation 6.10}$$

where  $C_s$  is a constant not dependent on temperature.

From Equation 6.10, it can be derived that when  $\ln(\frac{\Delta L}{L_0})$  is plotted against inverse temperature the data lies along a straight line which has an absolute gradient related to the activation energy ( $E_{act}$ ).

Figure 6.20 (b) shows the replotted curves of experimental data of sintering shrinkage (Figure 6.2 (a)). The apparent activation energy ( $E_{act}$ ) was calculated as 600kJ/mol for P0 and 514kJ/mol for P5. The difference may be caused by the random shapes and sizes for P5

which caused a poor fit between the data and Equation 6.5. Previous reported  $E_{act}$  values for sintering of YSZ were in a wide range of between 500kJ/mol-800kJ/mol <sup>[262-265]</sup>, and the  $E_{act}$  value calculated in this work falls into this range.

### §6.3.2 Microhardness

The mechanical hardness of heat treated coatings reflects the degree of sintering, where a higher hardness value represents a better sintered coating. The isothermal sintering temperature is one of the most important factors determining the coating hardness, a higher temperature can induce a higher coating hardness (Figure 6.5). By considering the neck formation between particles, the strength of the coating can be related to the variables in the following equation <sup>[31]</sup>.

$$\frac{x}{a} = \left( \frac{40\gamma_{sv}\Omega D^*}{k_B T} \right)^{\frac{1}{5}} a^{-\frac{3}{5}} t^{\frac{1}{5}} \quad \text{Equation 6.11}$$

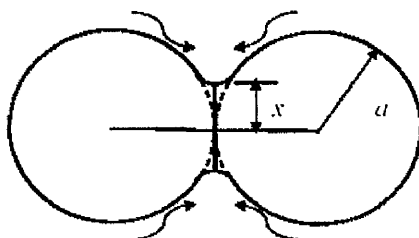


**Figure 6.21 Schematic representation of the contact area between two sintered particles**

where  $x$  is the neck length formed between particles as shown in Figure 6.21, and  $a$  is the particle radius, and others are same as introduced previously. The sintering temperature is crucial because the diffusion coefficient  $D^*$  shows an exponential relation to temperature (Equation 6.6). The particle size is another important factor for the formation of necks between particles and hence the hardness of the coatings (Figure 6.13). Particles with smaller sizes show a higher tendency to form necks. From Equation 6.11, it can be derived that the neck formation shows a reciprocal relation to the three fifth power of particle sizes. Comparing the effects of sintering temperature and particle sizes, the sintering time shows less effect on the neck formation between particles according to Equation 6.11. The

mechanical hardness results shown in Figure 6.5 also indicated that the increase of mechanical hardness by elongating the sintering time from 2 hours to 40 hours were not significant.

For constrained sintered coatings, (because of the substrate,) the densification process is retarded in the in-plane directions, so that the densification rate can be written as <sup>[257]</sup>:

$$\frac{\dot{\rho}}{\rho} = \frac{\sigma_s}{K_v} \left[ 1 - \frac{4G_v}{4G_v + 3K_v} \exp\left(\frac{-\beta d}{l}\right) \right] \quad \text{Equation 6.12}$$

$$\beta = \left( \frac{72K_v}{4G_v + 3K_v} \right)^{\frac{1}{2}} \quad \text{Equation 6.13}$$

where  $\frac{\dot{\rho}}{\rho}$  refers to the densification rate,  $K_v$  and  $G_v$  are the bulk modulus and shear modulus of the coating compact respectively, and  $\beta$  is a constant given by Equation 6.13, and  $d$  and  $l$  are the thickness and the length of the coating respectively, and  $\sigma_s$  is the intrinsic sintering stress which can be given by:

$$\sigma_s = \frac{2\gamma_{sv}}{r_p} + \frac{2\gamma_b}{a_g} \quad \text{Equation 6.14}$$

where  $\gamma_{sv}$  and  $\gamma_b$  are the surface energy and grain boundary energy of particles respectively, and  $r_p$  and  $a_g$  are the pore radius and the grain size respectively.

When  $d \rightarrow \infty$  (for coating far away from the substrate in an extremely thick coating), Equation 6.12 is reduced to  $\frac{\dot{\rho}}{\rho} = \frac{\sigma_s}{K_v}$ , which refers to the densification rate of a freely sintered coating. When  $d=0$  (for coating close to the substrate or for very thin film), and if substituting  $K_v$  and  $G_v$  is following <sup>[257]</sup>:

$$K_v = \frac{E_v}{3(1-2\nu_v)} \quad \text{Equation 6.15}$$



$$G_v = \frac{E_v}{2(1+\nu_v)} \quad \text{Equation 6.16}$$

where  $E_v$  and  $\nu_v$  are the Young's modulus and Poisson's ratio of the coating compacts, then Equation 6.12 can be simplified to:

$$\frac{\dot{\rho}}{\rho} = \frac{\sigma_s}{K_v} \cdot \frac{1+\nu_v}{3(1-\nu_v)} \quad \text{Equation 6.17}$$

So the densification rate for the coatings near the substrate is lower than that for freely sintered coatings (Figure 6.4 and Figure 6.9), and the mechanical properties i.e. the hardness of the constrained sintered coatings showed lower values than the freely sintered ones (Figure 6.5 and Figure 6.13). Also from the Equation 6.12, the densification rate of the constrained sintered coatings is a function of the coating thickness,  $d$ , the thicker the coating is, the less difference appears between constrained and freely sintered coatings (Figure 6.18 and Figure 6.19).

### §6.3.3 Electric field densification

The microstructural difference induced by the electric field densification indicated in Figure 6.16 illustrates that slight agglomeration of the particles is introduced by the electric field densification of the coatings. These agglomerates were formed because the small individual P0 particles in the coatings may approach each other under the effects of the electric field densification. Agglomerates in the coating reduced the hardness of the coatings which have undergone electric field densification (Figure 6.17, P0). When there are larger particles existing in the coating, i.e. in P2 and P5 coatings, relatively small particles have chances to approach and adhere to the surface of larger particles during the electric field densification process. This kind of microstructural change can be identified from Figure 6.16 (d), in which the middle peak (pore sizes from 0.02 $\mu\text{m}$  to 0.08 $\mu\text{m}$ ) separated into two parts after the densification process. The improvement in hardness values for P2 and P5 coatings comes from the specific microstructure of the small particles glued onto large particles, because small particles have a greater tendency to form necks during sintering, which can bridge large particles together and leave fewer weak

connections (large to large joints) so that the coating strength is improved (Figure 6.17 P2 and P5).

### §6.4 Summary

The sintering mechanism of YSZ EPD coatings was evaluated from the sintering data, and was determined as grain-boundary diffusion. The experimental activation energy for diffusion of ionic species in YSZ particles was calculated to be approximately 600kJ/mol from the sintering data.

Constrained sintered coatings had lower density and hardness than freely sintered coatings. Smaller particles were affected more by the substrate constraint during sintering because they had higher tendencies to shrink than larger particles. The microstructure and mechanical properties of constrained sintered coatings depended on the coating thickness (from  $\sim 10\mu\text{m}$ – $\sim 60\mu\text{m}$  for P0 coatings, and from  $\sim 60\mu\text{m}$  to  $\sim 200\mu\text{m}$  for P5 coatings), thicker coatings had denser microstructures and higher hardness. Electric field densification induced microstructural differences that did affect the mechanical hardness of constrained sintered coatings, i.e., increased the hardness of coatings with mixed sized particles, and lowered the hardness of coatings with mono-sized small particles. However, the electric field densification had little effect for coatings with mono-sized large particles.

## Chapter 7 Conclusions

EPD is a facile technique for fabrication of ceramic coatings, whose forte is the controllability. Rates and extents of deposition are governed by deposition conditions, i.e. applied voltage and deposition time etc. Microstructures of EPD coatings can be manipulated both by tailoring the natures of raw particles including the chemical composition, crystallinity and the agglomerate size/distribution etc., and by controlling the processing conditions, i.e. EPD conditions (packing particles in wet deposits), drying conditions (forming green coatings), and sintering conditions (consolidating particle compacts). In this study, EPD has been used to fabricate YSZ coatings on FeCrAlloy substrates. Deposition kinetics, particle packing mechanisms during deposition, and microstructural developments from wet EPD deposits to sintered coatings have been discussed.

From EPD of submicrometre sized particles, the deposition kinetics were discussed based on Hamaker's equation, and the deposition rate was determined to be proportional to the applied voltage, particle concentration, and zeta-potential of particles. The particle packing density in wet EPD deposits was examined to vary with deposition conditions, i.e. the deposition time, applied voltage, and the electrical conductivity of the suspension, etc. The rearrangement of deposited particles in the wet EPD coating was experimentally proved by the electric field densification of as-deposited EPD coatings in pure solvent by the application of a constant electric field. The particle packing mechanism during deposition was proposed to be the electro-osmotic flow in the wet deposit induced by the applied electric field. The particle packing condition of wet EPD coatings was found to be effective on the microstructure and hardness of sintered coatings. However, little effect of wet coating density has been detected on the densities of dry and sintered coatings.

The agglomerate size of raw particles influences not only the deposition process, i.e. the deposition rate and the particle packing density, but also the microstructure and hardness of sintered coatings. Small particles are preferable for sintering, because free sintered coatings fabricated from small particles have higher densities and higher hardness values than large particles. However, EPD of small particles has a lower deposition rate and EPD coatings

fabricated with small particles have lower particle packing densities. EPD of mixed sized particles has a higher green density than that of mono-sized particles. For EPD coatings fabricated by mixed sized particles the positions of small particles in the coating are important in determining the hardness of sintered coatings. Higher hardness values were detected for coatings with structures of small particles adhered on surfaces of large particles. The electric field densification of as-deposited mixed sized EPD coatings can produce such structures by rearrangement of small particles.

From the sintering study of YSZ EPD coatings, it was determined that the sintering mechanism was grain boundary diffusion controlled, and the activation energy for the diffusion of ionic species in YSZ particles was calculated to be  $\sim 600\text{kJ/mol}$ . The substrate constraint effect during sintering has been studied by comparison to free sintered coatings. A coating with greater shrinkage during free sintering can be affected more by the substrate constraint. EPD coatings fabricated from small particles shrink more during free sintering than those fabricated from large particles, so differences in coating density and hardness are more significant between free and constrained sintered coatings when fabricated from small particles. The specific particle packing arrangement of small particles on the surfaces of large particles can still induce higher hardness values for constrained sintered coatings than for arrangements of mono-sized particles.

In general, EPD is a promising technique for fabrication of ceramic coatings with tailored microstructures by properly manipulating the processing conditions.

## Chapter 8 Suggestions for Future Work

Based on the understanding gained from the current research, directions for further studies may include the following:

- It has been found that the positions of small particles in a mixed sized EPD coating are effective on the hardness of sintered coating, and a structure with small particles attached on surfaces of large particles is preferred for sintering to gain higher hardness. Developing a pre-treatment of raw particles that specifically obtains small particles glued on large particles is worthwhile to improve the sinterability of large particles. Alternatively, a particle synthesis method which can control the size and surface morphology of particles, i.e., micro-sized particles with rough surfaces, is desirably to supply raw particles for EPD.
- The aim of using mixed sized particles to fabricate EPD coatings is to achieve a high particle packing density, which is based on the assumption that small particles fill the gaps between large particles. EPD from suspensions with mixed sized particles can result in a random packing of large and small particles which may compromise the original aim. A layered structural EPD coating from two individual suspensions, i.e. one suspension with mono-sized large particles and the other suspension with mono-sized small particles, is expected to offer further control on particle packing. A carefully built-up layered EPD coating with large particles performing as “bricks” and small particles acting as “mortar” may provide both high particle packing density and high sinterability.
- The tensile stresses within the EPD coating that are applied by the substrate during the constrained drying and sintering may cause cracks in the coating. It is very important to avoid or control the formation of cracks to make EPD coatings practically applicable for protective-coatings. In chapter 6, it has been reported that long time (40 hours) sintering under a relative low temperature (1100°C) resulted in the formation of micro-cracks due to the differential sintering in the EPD coating. It is worthwhile to carry out further research on controlling the formation of cracks to release the tensile stresses in

the coating during constrained sintering by forming micro-cracks rather than large cracks.

- During EPD, not only particles in the suspension but particles in the deposit are moving and rearranging under the influence of the applied electric field. It is still not quite clear what the mechanism by which particles in the suspension form a deposit on the surface of electrode is. For further understanding the packing behaviour of particles during EPD it is essential to improve experimental techniques to allow accurate measurement of the travelling speeds of particles or a direct in-situ observation of particle movements throughout the entire EPD process. Computer modelling of particle movements from the beginning of application of the electric field to the end of deposition may also help to fundamentally understand the EPD process.

### References:

- [1] Clarke D. R. and Levi C. G., "Materials Design for the Next Generation Thermal Barrier Coatings", *Ann. Rev. Mater. Sci.*, 33, 383-417, 2003
- [2] Evans A. G., Mumm D. R., Hutchinson J. W., Meier G.H. and Pettit F.S., "Mechanisms Controlling the Durability of Thermal Barrier Coatings", *Prog. Mater. Sci.*, 46, 505-553, 2001
- [3] Padture N. P., Gell M. and Jordan E. H., "Thermal Barrier Coatings for Gas-Turbine Engine Applications", *Science*, 296, 280-284, 2002
- [4] Mayrhofer P. H., Mitterer C., Hultman L. and Clemens H., "Microstructural Design of Hard Coatings", *Prog. Mater. Sci.*, 51, 1032-1114, 2006
- [5] Choy K. L., "Chemical Vapour Deposition of Coatings", *Prog. Mater. Sci.*, 48, 57-170, 2003
- [6] Mattox D.M., "Physical Vapor Deposition Processes", *Products Finishing*, 65[12], 72-82, 2001
- [7] Lan W. H., Wang X. and Xiao P., "Agglomeration Effect on Drying of Yttria-Stabilised-Zirconia Slurry on A Metal Substrate", *J. Euro. Ceram. Soc.*, 26[16], 3599-3606, 2006
- [8] Lan W. H. and Xiao P., "Constrained Drying Behaviour of Yttria-Stabilised-Zirconia Slurry on A Substrate: I. Drying Mechanism", *J. Am. Ceram. Soc.*, 89, 1518-1522, 2006
- [9] Lan W. H. and Xiao P., "Drying Stress of Yttria-Stabilised-Zirconia Slurry on Metal Substrate", *J. Euro. Ceram. Soc.*, 27, 3117-3125, 2007
- [10] Besra L. and Liu M., "A Review on Fundamentals and Applications of Electrophoretic Deposition (EPD)", *Prog. Mater. Sci.* 52, 1-61, 2007
- [11] Corni I., Ryan M. P., and Boccaccini A. R., "Electrophoretic Deposition: From Traditional Ceramics to Nanotechnology", *J. Euro. Ceram. Soc.*, 28[7], 1353-67, 2008
- [12] Van der Biest O.O. and Vandeperre L. J., "Electrophoretic Deposition of Materials", *Annu. Rev. Mater. Sci.*, 29, 327-52, 1999
- [13] Sarkar P. and Nicholson P. S., "Electrophoretic Deposition (EPD): Mechanisms, Kinetics and Application to Ceramics", *J. Am. Ceram. Soc.*, 79, 1987-2002, 1996
- [14] Boccaccini A. R. and Zhitomirsky I., "Application of Electrophoretic and Electrolytic Deposition Techniques in Ceramics Processing", *Current Opinion in Solid State & Materials Science*, 6[3], 251-60, 2002



## References

---

- [15] Kaya C., Kaya F., Su B., Thomas B., and Boccaccini A. R., "Structural and Functional Thick Ceramic Coatings by Electrophoretic Deposition", *Surface & Coating Technology*, 191[2-3], 303-10, 2005
- [16] Sarkar P., Datta S., and Nicholson P. S., "A Functionally Graded Ceramic/Ceramic and Metal/Ceramic Composites by Electrophoretic Deposition," *Composites, Part B*, 28B, 49, 1997
- [17] Ferrari B., Sanchez-Herencia A. J., Moreno R., "Aqueous Electrophoretic Deposition of  $\text{Al}_2\text{O}_3/\text{ZrO}_2$  Layered Ceramics", *Mater. Lett.*, 35[5-6], 370-4, 1998
- [18] Hecht M., Renk K. F., Reimann C., and Waldmann O. "Preparation of (Ti, Pb)-1233 Multilayer Tapes by Use of an Electrophoretic Technique", *Supercond. Sci. Technol.*, 11, 227-30, 1998
- [19] Singh I., Kaya C., Shaffer M. S. P., Thomas B. C., and Boccaccini A. R., "Bioactive Ceramic Coatings Containing Carbon Nanotubes on Metallic Substrates by Electrophoretic Deposition", *J. Mater. Sci.*, 41[24], 8144-51, 2006
- [20] Chandrasekharan N., Kamat P. V., "Assembling Gold Nanoparticle as Nanostructured Films Using An Electrophoretic Deposition Approach", *Nano Letters*, 1[2], 67-70, 2001
- [21] Boccaccini A. R., MacLaren I., Lewis M. H., and Ponton C. B., "Electrophoretic Deposition Infiltration of 2-D Woven SiC Fibre Mats with Mixed Sols of Mullite Composition", *J. Euro. Ceram. Soc.*, 17[13], 1545-50, 1997
- [22] Greil P., Cordelair J., and Bezold A., "Discrete Element Simulation of Ceramic Powder Processing", *Z Metallk.*, 92, 682-9, 2000
- [23] Koelmans H. and J. Overbeek Th. G., "Stability and Electrophoretic Deposition of Suspensions in Non-Aqueous Media", *Discuss. Faraday Soc.*, 18, 52-63, 1954
- [24] Zhitomirsky I., "Cathodic Electrodeposition of Ceramic and Organoceramic Materials: Fundamental Aspects", *Advances in Colloid and Interface Science*, 97, 279-317, 2002
- [25] Van der Biest O. O., Joos E., Vleugels J., and Baufeld B., "Electrophoretic Deposition of Zirconia Layers for Thermal Barrier Coatings," *J. Mater. Sci.*, 41, 8086-92, 2006
- [26] Wang Z. C., Schemilt J., and Xiao P., "Fabrication of Ceramic Composite Coatings Using Electrophoretic Deposition, Reaction Bonding and Low Temperature Sintering," *J. Euro. Ceram. Soc.*, 22[2], 183-9, 2002
- [27] Solomentsev, Y., Guelcher, S. A., Bevan, M. and Anderson, J. L., "Aggregation Dynamics for Two Particles during Electrophoretic Deposition under Steady Fields", *Langmuir*, 16, 9208-16, 2000
- [28] Hoggard J. D., Sides P. J., and Prieve D. C., "Electrolyte-dependent Multiparticle Motion near Electrodes in Oscillating Electric Fields", *Langmuir*, 24[7], 2977-82, 2008

## References

---

- [29] Yeh S. R., Seul M., and Shaiman B.I., "Assembly of Ordered Colloidal Aggregates by Electric-Field-Induced Flow", *Nature*, 386, 57-59, 1997
- [30] Trau M., Saville D. A. and Aksay I. A., "Field-Induced Layering of Colloidal Crystals", *Science*, 272, 706-709, 1996
- [31] Ring T. A. *Fundamentals Ceramic Powder Processing and Synthesis*, Academic Press, London, 1996
- [32] Lewis J. A., "Colloidal Processing of Ceramics", *J. Am. Ceram. Soc.*, 83[10], 2341-59, 2000
- [33] Lange F. F., "Powder Processing Science and Technology for Increased Reliability", *J. Am. Ceram. Soc.*, 72[1], 3-15, 1989
- [34] Milne S. J., Patel M. and Dickinson E., "Experimental Studies of Particle Packing and Sintering Behaviour of Monosize and Bimodal Spherical Particles", *J. Euro. Ceram. Soc.*, 11, 1-7, 1993
- [35] Hellmig R. J. and Ferkel H., "Using Nanoscaled Powder as an Additive in Coarse-Grained Powder," *J. Am. Ceram. Soc.*, 84[2], 261-66, 2001
- [36] Messing G. L. and Jr. Onoda G. Y., "Inhomogeneity-Packing Density Relations in Binary Powders," *J. Am. Ceram. Soc.*, 66 [1-2], 1-5, 1978
- [37] Westman A. E. R. and Hugill H. R., "Packing of Particles." *J. Am. Ceram. Soc.*, 13[10], 767-79, 1930
- [38] McGeary R. K., "Mechanical Packing of Spherical Particles," *J. Am. Ceram. Soc.*, 44[10], 513-22, 1961
- [39] C. M. Kong and J. J. Lannutti, "Agglomerate Size Distribution on Loose Packing Fraction," *J. Am. Ceram. Soc.*, 83[9], 2183-88, 2000
- [40] Hyam R. S., Subhedar K. M., and Pawar S. H., "Effect of Particle Size Distribution and Zeta Potential on the Electrophoretic Deposition of Boron Films", *Colloids and Surfaces A*, 315[1-3], 61-65, 2008
- [41] Guelcher S. A., Solomentsev Y., and Anderson J. L., "Aggregation of Pairs of Particles on Electrodes during Electrophoretic Deposition", *Powder Technology*, 110, 90-97, 2000
- [42] Sato N., Kawachi M., Noto K., Yoshimoto N., and Yoshizawa M., "Effect of Particle Size Reduction on Crack Formation in Electrophoretically Deposited YBCO Films", *Physica C*, 357-360, 1019-22, 2001
- [43] Scherer G. W. and Garino T., "Viscous Sintering on a Rigid Substrate", *J. Am. Ceram. Soc.*, 68 [4], 216-20, 1985

## References

---

- [44] Bordia R. K. and Scherer G.W., "On Constrained Sintering-II. Comparison of Constitutive Models", *Acta Metall.*, 36 [9], 2399-409, 1988
- [45] Rahaman M. N., *Ceramics Processing and Sintering*, pp. 624-32. Marcel Dekker, New York, 1995
- [46] Guillon O., Weiler L., and Rodel J., "Anisotropic Microstructural Development during the Constrained Sintering of Dip-Coated Alumina Thin Films", *J. Am. Ceram. Soc.*, 90 [5], 1394-1400, 2007
- [47] Garino T. J. and Bwoen H. K., "Kinetics of Constrained Film Sintering". *J. Am. Ceram. Soc.*, 73[2], 251-57, 1990
- [48] Reed J. S. *Principles of Ceramics Processing (Second Edition)*, John Wiley & Sons, New York, 1995
- [49] Yang R. Y., Zou R. P., and Yu A. B., "Computer Simulation of the Packing of Fine Particles", *Physical Review E*, 62 [3], 3900-08, 2000
- [50] Smith D. M., Scherer G. W., and Anderson J. M., "Shrinkage during Drying of Silica Gel", *J. Non-Cryst. Solids*, 188, 191-206, 1995
- [51] Scherer G. W., "Fundamentals of Drying and Shrinkage"; pp. 199-211 in *Science of Whitewares*. Edited by V. E. Henkes, G. Y. Onoda, and W. M. Carty. American Ceramic Society, Westerville, OH, 1997
- [52] Bordia R. K. and Jagota A., "Crack Growth and Damage in Constrained Sintering Films", *J. Am. Ceram. Soc.*, 76[10], 2475-85, 1993
- [53] Bordia R. K. and Raj R., "Sintering Behaviour of Ceramic Films Constrained by a Rigid Substrate", *J. Am. Ceram. Soc.*, 68[6], 287-92, 1985
- [54] Bordia R. K. and Scherer G. W., "On Constrained Sintering: I. Constitutive Model for a Sintering Body, II. Comparison of Constitutive Models, III. Rigid Inclusions", *Acta Metall.*, 36[9], 2393-16, 1988
- [55] Graham T., *Phil. Trans. Roy. Soc.* 151, Part I, 183-224, 1861
- [56] Aksay I. A., "Microstructure Control through Colloidal Consolidation", *Forming of Ceramics*, American Ceramic Society, Columbus, OH, 1984
- [57] Guo J. and Lewis J. A., "Aggregation Effects on Compressive Flow Properties and Drying Behavior of Colloidal Silica Suspensions", *J. Am. Ceram. Soc.*, 82[9], 2345-58, 1999
- [58] Rhodes W. H., "Agglomerate and Particle Size Effects on Sintering Ytria-Stabilized-Zirconia", *J. Am. Ceram. Soc.*, 64[1], 19-22, 1981

## References

---

- [59] Terpstra R. A., Pex P. P. A. C., and De Vries A. H., *Ceramic Processing*, Chapman & Hall, London, 1995
- [60] Overbeek, J. T. G., *Colloid Science*, Vol. 1, Elsevier, Amsterdam, 1952
- [61] Hamaker H. C., "The London-vdW Attraction between Spherical Particles", *Physica* (Amsterdam), 4 [10], 1058-72, 1937
- [62] Xu R. L., Wu C. F., and Xu H. Y., "Particle Size and Zeta Potential of Carbon Black in Liquid Media", *Carbon*, 45[14], 2806-09, 2007
- [63] Gupta S. D. and Bhagwat S. S., "Adsorption of Surfactants on Carbon Black-Water Interface", *Journal of Dispersion Science and Technology*, 26[1], 111-20, 2005
- [64] Israelachvili J. N. *Intermolecular and Surface Forces* (Second Edition), Academic Press, London, 1991
- [65] Hunter R. J. *Foundations of Colloid Science*, Vol. 1, Oxford University Press, Oxford, 1987
- [66] Russel W. B., Saville D. A. and Schowalter W. R., *Colloidal Dispersions*, Cambridge University Press, Cambridge, 1989
- [67] Derjaguin, B. V., "Untersuchungen über die Reibung und Adhäsion, IV", *Kolloid-Zeitschrift*, 69[2], 155-64, 1934
- [68] Hogg R., Healy T. W. and Fuerstenau D. W., "Mutual Coagulation of Colloidal Dispersions", *Transactions of the Faraday Society*, 62, 1638-51, 1966
- [69] Hidalgo-Alvarez R., "On the Conversion of Experimental Electrokinetic Data into Double Layer Characteristics in Solid-Liquid Interfaces", *Adv. Colloid Interfaces Sci.*, 34, 217-341, 1991
- [70] Greenwood R., "Review of the Measurement of Zeta Potentials in Concentrated Aqueous Suspensions Using Electroacoustics", *Adv. Colloid Interfaces Sci.*, 106, 55-81, 2003
- [71] Kimura T., Kaneko Y. and Yamaguchi T., "Consolidation of Alumina-Zirconia Mixtures by A Colloid Process", *J. Am. Ceram. Soc.*, 74[3], 625-32, 1991
- [72] Wei W. C. J., Wang S. C. and Ho F. Y., "Electrokinetic Properties of Colloidal Zirconia Powders in Aqueous Suspension", *J. Am. Ceram. Soc.*, 82[12], 3385-92, 1999
- [73] Moreno R., Requena J., and Moya J. S., "Slip Casting of Ytria-Stabilized Tetragonal Zirconia Polycrystals", *J. Am. Ceram. Soc.*, 71[12], 1036-40, 1988
- [74] Wernet J. and Feke D. L., "Effects of Solids Loading and Dispersion Schedule on the State of Aqueous Alumina/Zirconia Dispersions", *J. Am. Ceram. Soc.*, 77[10], 2693-98, 1994

## References

---

- [75] Paik U. and Hackley V. A., "Influence of Solids Concentration on the Isoelectric Point of Aqueous Barium Titanate", *J. Am. Ceram. Soc.*, 83[10], 2381-84, 2000
- [76] Leong Y. K., Scales P. J., Healy T. W., and Boger D. V., "Effect of Particle Size on Colloidal Zirconia Rheology at the Isoelectric Point", *J. Am. Ceram. Soc.*, 78[8], 2209-12, 1995
- [77] Kagawa M., Omori M. and Syono Y., "Surface Characterization of Zirconia after Reaction with Water", *J. Am. Ceram. Soc.*, 70[9], C212 -213, 1987
- [78] De Faria L. A., Boodts J. F. C., and Trasatti S., "Effect of Composition on the Point of Zero Charge of  $\text{RuO}_2+\text{TiO}_2+\text{CeO}_2$  Mixed Oxides", *Colloids and Surfaces A: Physicochemical and Engineering Aspects*, 132[1], 53-59, 1998
- [79] Guldberg-pedersen H. and Bergstrom L., "Forces Measurement between Zirconia Surfaces in Poly (acrylic acid) Solutions", *J. Am. Ceram. Soc.*, 82[5], 1137-45, 1999
- [80] Aksay I. A., "Microstructure Control through Colloidal Consolidation", *Advances in Ceramics*, Vol.9, Forming of Ceramics, American Ceramic Society, Columbus, OH, 1984
- [81] Sato T. and Ruch R., *Stabilization of Colloidal Dispersions by Polymer Adsorption*, Vol. 9 New York, 1980
- [82] Napper D. H., *Polymeric Stabilization of Colloidal Dispersions*, Academic Press, London, 1983
- [83] Vincent B., Edwards J., Emmett S. and Jones A., "Depletion Flocculation in Dispersion of Sterically Stabilised Particles (soft spheres)", *Colloids Surf.*, 18, 261-81, 1986
- [84] Derjaguin V. V. and Landau L. D., "Theory of Stability of Highly Charged Lyophobic Sols and Adhesion of Highly Charged Particles in Solutions of Electrolytes", *Acta Physicochim, URSS*, 14, 633-52, 1941
- [85] Verwey E.J.W. and Overbeek J.Th.G., *Theory of Stability of Lyophobic Colloids*. Elsevier, Amsterdam, Netherlands, 1948
- [86] Sigmund W. A., Bell N. S., and Bergstrom L., "Novel Powder-Processing Methods for Advanced Ceramics", *J. Am. Ceram. Soc.*, 83[7], 1557-74, 2000
- [87] Lange F. F., "Shape Forming of Ceramic Powders by Manipulating the Interparticle Pair Potential", *Chem. Eng. Sci.*, 56, 3011-20, 2001
- [88] Velamakanni B. V., Chang J. C., Lange F. F., and Pearson D. S., "New Method for Efficient Colloidal Particle Packing via Modulation of Repulsive Lubricating Hydration Forces", *Langmuir*, 6, 1323-25, 1990

## References

---

- [89] Chang J. C., Lange F. F., and Pearson D. S., "Viscosity and Yield Stress of  $\text{Al}_2\text{O}_3$  Slurries Containing Large Concentrations of Electrolyte", *J. Am. Ceram. Soc.*, 77[1], 19-26, 1994
- [90] Bergstrom L., Schilling C. H., and Aksay I. A., "Consolidation Behaviour of Flocculated Alumina Suspensions", *J. Am. Ceram. Soc.*, 75[12], 3305-14, 1992
- [91] Chang J. C., Velamakanni B. V., Lange F. F., and Pearson D. S., "Centrifugal Consolidation of  $\text{Al}_2\text{O}_3$  and  $\text{Al}_2\text{O}_3/\text{ZrO}_2$  Composite Slurries vs Interparticle Potentials: Particle Packing and Mass Segregation", *J. Am. Ceram. Soc.*, 74[9], 2201-04, 1991
- [92] Velamakanni B. V. and Lange F. F., "Effect of Interparticle Potential and Sedimentation on Particle Packing Density of Bimodal Particle Distributions during Pressure Filtration", *J. Am. Ceram. Soc.*, 74[1], 166-72, 1991
- [93] Sinha R., "A Treatment of the Viscosity of Concentrated Suspensions", *J. Appl. Phys.*, 23, 1020, 1952
- [94] Voyutsky S., (translated by Bobrov N.), "Colloid Chemistry", Mir Publishers, Moscow, 1978
- [95] Kosmulski M., Gustafsson J., and Rosenholm J. B., "Correlation between the Zeta Potential and Rheological Properties of Anatase Dispersions", *J. Colloid and Interface Sci.*, 209, 200-06, 1999
- [96] Zaman A. A. and Dutcher C. S., "Viscosity of Electrostatically Stabilized Dispersions of Monodispersed Bimodal and Trimodal Silica Particles", *J. Am. Ceram. Soc.*, 89[2], 422-30, 2006
- [97] Rodriguez B.E., Kaler E.W. and Wolfe M.S., "Binary Mixtures of Monodisperse Latex Dispersions: II. Viscosity", *Langmuir*, 8, 2382-89, 1992
- [98] Luckham P.F. and Ukeje M.A., "Effect of Particle Size Distribution on the Rheology of Dispersed Systems", *J. Colloid and Interface Sci.*, 220, 347-56, 1999
- [99] Lange F. F. and Miller K. T., "Pressure Filtration: Kinetics and Mechanics", *Am. Ceram. Soc. Bull.*, 66[10], 1498-504, 1987
- [100] Fennelly T. J. and Reed J. S., "Mechanics of Pressure Casting", *J. Am. Ceram. Soc.*, 55[5], 264-68, 1972
- [101] Adcock D. S. and McDowall I. C., "The Mechanism of Filter Pressing and Slip Casting", *J. Am. Ceram. Soc.*, 40[10], 355-60, 1957
- [102] Rowlands R. R., "A Review of the Slip Casting Process", *Am. Ceram. Soc. Bull.*, 45[1], 16-19, 1966

## References

---

- [103] Aksay I. A. and Schilling C. H., "Mechanics of Colloidal Filtration", Forming of Ceramics. Edited by Mangels J. A. and Messing G. L., American Ceramic Society, pp. 85-93. Columbus, OH, 1984
- [104] Howatt G. N., Breckenridge R. G., and Brownlow J. M., "Fabrication of Thin Sheets for Capacitors", J. Am. Ceram. Soc., 30[8], 237-42, 1947
- [105] Shanefield D. J. and Mistler R. E., "Fine-Grained Alumina Substrates: I, The Manufacturing Process", Am. Ceram. Soc. Bull., 53[5], 416-20, 1974
- [106] Mistler R. E., "Tape Casting: The Basic Process for Meeting the Needs of the Electronic Industry", Am. Ceram. Soc. Bull., 69[6], 1022-26, 1990
- [107] Miller K. T., Melant R. M., and Zukoski C. F., "Comparison of the Compressive Yield Response of Aggregated Suspensions: Pressure Filtration, Centrifugation, and Osmotic Consolidation," J. Am. Ceram. Soc., 79[10], 2545-56, 1996
- [108] Miller K. T. and Zukoski C. F., "Osmotic Consolidation of Suspensions and Gels", J. Am. Ceram. Soc., 77[9], 2473-78, 1994
- [109] Allain C., Cloitre M., and Wafra M., "Aggregation and Sedimentation in Colloidal Suspensions", Phys. Rev. Lett., 74[8], 1478-81, 1995
- [110] Buscall R., "The Sedimentation of Concentrated Colloidal Suspensions", Colloids Surf., 43, 33-53, 1990
- [111] Okubo T., "Sedimentation Velocity of Colloidal Spheres in Deionized Suspension", J. Phys. Chem., 98, 1472-74, 1994
- [112] Batchelor G. K., "Sedimentation in a Dilute Dispersion of Spheres", J. Fluid Mech., 52[2], 245-68, 1972
- [113] Philipse A. P., Bonekamp B. C., and Veringa H. J., "Colloidal Filtration and (Simultaneous) Sedimentation of Alumina and Silica Suspensions: Influence of Aggregates", J. Am. Ceram. Soc., 73[9], 2720-27, 1990
- [114] Richardson J. F. and Zaki W. N., "The Sedimentation of a Suspension of Uniform Spheres Under Conditions of Viscous Flow", Chem. Eng. Sci., 8, 65-78, 1954
- [115] Lange F. F., "Forming a Ceramic by Flocculation and Centrifugal Casting", U.S. Pat. No. 4624808, 1986
- [116] Beylier E., Pober R. L., and Cima M. J., "Centrifugal Casting of Ceramic Components", pp. 529-36 in Ceramic Transactions, Vol. 12, Ceramic Powder Science III. Edited by Messing G. L., Hirano S., and Hausner H., American Ceramic Society, Westerville, OH, 1990



## References

- [117] Chang J. C., Lange F. F., and Pearson D. S., "Centrifugal Consolidation of  $\text{Al}_2\text{O}_3$  and  $\text{Al}_2\text{O}_3/\text{ZrO}_2$  Composite Slurries vs Interparticle Potentials: Particle Packing and Mass Segregation", *J. Am. Ceram. Soc.*, 74[9], 2201-04, 1991
- [118] Rivers R. D., "Method of Injection Molding Powder Metal Parts", U.S. Pat. No. 41134180, 1978
- [119] Fanelli A. J., Silvers R. D., and Frei W. S., "New Aqueous Injection Molding Process for Ceramic Powders", *J. Am. Ceram. Soc.*, 72[10], 1833-36, 1989
- [120] Omatete O. O., Janney M. A., and Strehlow R. A., "Gelcasting-A New Ceramic Forming Process", *Am. Ceram. Soc. Bull.*, 70[10], 1641-49, 1991
- [121] Young A. C., Omatete O. O., Janney M. A., and Menchhofer P. A., "Gelcasting of Alumina", *J. Am. Ceram. Soc.*, 74[3], 612-18, 1991
- [122] Morissette S. and Lewis J. A., "Chemorheology of Aqueous Alumina-Poly(vinylalcohol) Gelcasting Suspensions", *J. Am. Ceram. Soc.*, 82[3], 521-28, 1999
- [123] Gaukler L. J., Graule Th., and Baader F., "Ceramic Forming Using Enzyme Catalyzed Reactions", *Mater. Chem. Phys.*, 61, 78-102, 1999
- [124] Shaw T. M., "Drying as an Immiscible Displacement Process with Fluid Counterflow", *Phys. Rev. Lett.*, 59[15], 1671-74, 1987
- [125] Scherer G. W., "Drying Gels, VIII. Revision and Review", *J. Non-Cryst. Solids*, 109, 171-82, 1991
- [126] Descamps M., Mascart M. and Thierry B., "How to Control Cracking of Tape-Cast Sheets", *Am. Ceram. Soc. Bull.*, 74[3], 89-92, 1995
- [127] Streicher E. and Chartier T., "Study of Cracking and Microstructural Evolution during Drying of Tape-Cast Aluminum Nitride Sheets", *J. Mater. Sci.*, 26, 1659-65, 1991
- [128] Chiu R. C. and Cima M. J., "Drying of Granular Ceramic Films: I, Effects of Process Variables on Cracking Behavior", *J. Am. Ceram. Soc.*, 76[9], 2257-64, 1993
- [129] Chiu R. C. and Cima M. J., "Drying of Granular Ceramic Films: II, Drying Stress and Saturation Uniformity", *J. Am. Ceram. Soc.*, 76[11], 2769-77, 1993
- [130] Lewis J. A., Blackman K. A., Ogden A. L., Payne J. A., and Francis L. F., "Rheological Properties and Stress Development during Drying of Tape-Cast Ceramic Layers", *J. Am. Ceram. Soc.*, 79[12], 3225-34, 1993
- [131] Scherer G. W., "Theory of Drying", *J. Am. Ceram. Soc.*, 73[1], 3-14, 1990
- [132] Lange F. F., "Chemical Solution Routes to Single-Crystal Thin Films", *Science*, 273, 903-09, 1996

## References

---

- [133] Hutchinson J. W. and Suo Z., in *Advances in Applied Mechanics*. J.W. Hutchinson and Wu T.Y., Eds PP. 63-191 Academic Press, New York, 1991
- [134] Bohn S., Platkiewicz J., Andreotti B., Adda-Bedia M. and Couder Y., "Hierarchical Crack Pattern as Formed by Successive Domain Divisions. II. From Disordered to Deterministic Behaviour", *Physical Review E*, 71, 046215-17, 2005
- [135] Mal D., Sinha S., Mitra S., and Tarafdar S., "Formation of Crack Networks in Drying Laponite Films", *Physic A*, 346, 110-15, 2005
- [136] De Bozes, Baker and Ellis, "Abstract of a Letter from Monsieur De Bozes, Professor of Experimental Philosophy, at the Academy of Wirtemberg, to Monsieur DeMaizau. Communicated by Mr. Baker from Mr. Ellis, and Tanslated out of the Latin by Mr. Baker", *Philosophical Transactions*, 43, 419-21, 1745
- [137] Harsanyi E., "Method of Coating Radiant Bodies", U. S. Patent No. 1897902, 1933
- [138] Pickard W. F., "Remarks on the Theory of Electrophoretic Deposition", *Journal of the Electrochemical Society*, 115m, 105c-108c, 1968
- [139] Heavens S. N., "Electrophoretic Deposition as A Processing Route for Ceramics", *Advanced Ceramic Processing and Technology*, Noyes Publications, New Jersey, 255-83, 1990
- [140] Gani M. S. J., "Electrophoretic Deposition. A Review", *Ind. Ceram.*, 14, 163-174, 1994
- [141] Boccaccini A. R., Roether J. A., Thomas B. J. C., Shaffer M. S. P., et al., "The Electrophoretic Depositon of Inorganic Nanoscaled Materials", *J. Ceram. Soc. Jpn.*, 114, 1-14, 2006
- [142] Boccaccini A. R. Cho J., Roether J. A., Thomas B. J. C., et al., "Electrophoretic Deposition of Carbon Nanotubes", *Carbon*, 44, 3149-60, 2006
- [143] Avgustinik A. I., Vigdergauz V. S., and Zhuravlev G. I., "Electrophoretic Deposition of Ceramic Masses from Suspensions and Calculation of Deposit Yields", *J. Appl. Chem. USSR (Engl. Transl.)*, 35, 2090-93, 1962
- [144] Krishna Rao D. U. and Subbarao E. C., "Electrophoretic Deposition of Magnesia", *Am. Ceram. Soc. Bull.*, 58[4], 467-69, 1979
- [145] Krishna Rao D. U., Malage A. B., Baral D., and Subbarao E. C., "Kinetics of Electrophoretic Deposition of  $\beta$ -Alumina", *Bull. Mater. Sci.*, 8[1], 1-11, 1986
- [146] Ciou S. J., Fung K. Z., and Chiang K. W., "The Mathematical Expression for Kinetics of Electrophoretic Deposition and the Effects of Applied Voltage", *Journal of Power Sources*, 172[1], 358-62, 2007

## References

---

- [147] Hamaker H. C., "Formation of Deposition by Electrophoresis", *Trans. Farad. Soc.*, 36, 279-83, 1940
- [148] Biesheuvel P. M. and Verweij H., "Theory of Cast Formation in Electrophoretic Deposition", *J. Am. Ceram. Soc.*, 82[6], 1451-55, 1999
- [149] Probstein R. F., *Physicochemical Hydrodynamics, An Introduction* pp. 214-33, Butterworths, Boston, MA, 1989
- [150] Russel W. B., Saville D. A., and Schowalter W. R., *Colloidal Dispersions*; pp. 411-14. Cambridge University Press, Cambridge, U.K., 1989
- [151] Hiemenz P. C. and Rajagopalan R., *Principles of Colloid and Surface Chemistry*, 3rd ed.; pp. 537-48. Marcel Dekker, New York, 1997
- [152] Hirata Y., Nishimoto A., and Ishihara Y., "Forming of Alumina Powder by Electrophoretic Deposition", *J. Ceram. Soc. Jpn., Int. Ed.*, 99, 105-109, 1991
- [153] Ishihara T., Sato K., and Takita Y., "Electrophoretic Deposition of  $Y_2O_3$ -Stabilized  $ZrO_2$  Electrolyte Films in Solid Oxide Fuel Cells", *J. Am. Ceram. Soc.*, 79[4], 913-19, 1996
- [154] Lindner F. and Feltz A., "Thin Layer NTC Semiconductor Ceramics Based on  $NiMn_2O_4$  and  $Zn_zNiMn_{2-z}O_4$  ( $z=1/3, 2/3$ )", *J. Euro. Ceram. Soc.*, 11, 269-74, 1993
- [155] Lindner F. and Feltz A., "Electrophoretic Deposition-A Method for Preparation of Semiconducting Oxide Ceramic Layers", *Solid State Ionics*, 63-65, 13-17, 1993
- [156] Powers R. W., "Ceramic Aspects of Forming Beta-Alumina by Electrophoretic Deposition", *American Ceramic Society Bulletin*, 65[9], 1270-77, 1986
- [157] Negishi H., Sakai N., Yamaji K., Horita T., and Yokokawa H., "Application of Electrophoretic Deposition Technique to Solid Oxide Fuel Cells", *J. Electrochem. Soc.* 147, 1682-87, 2000
- [158] Gutierrez C. P., Wallace T. C., and Mosley J. R., "Electrophoretic Deposition: A Versatile Coating Method", *J. Electrochem. Soc.*, 109[10], 923-27, 1962
- [159] Kawai C. and Wakamatsu S., "Fabrication of C/SiC Composites by An Electrodeposition/Sintering Method and the Control of the Properties", *J. Mater. Sci.*, 31, 2165-70, 1996
- [160] Zhang Z., Huang Y. and Jiang Z., "Electrophoretic Deposition Forming of SiC-TZP Composites in A Nonaqueous Sol Media", *J. Am. Ceram. Soc.*, 77, 1946, 1994
- [161] Sarkar P. and Nicholson P. S., "Comments on 'Electrophoretic Deposition Forming of SiC-TZP Composites in A Nonaqueous Sol Media'", *J. Am. Ceram. Soc.*, 78[11], 3165-66, 1995

## References

---

- [162] Zhang. Z., "Reply to 'Comments on Electrophoretic Deposition Forming of SiC-TZP Composites in A Nonaqueous Sol Media'", J. Am. Ceram. Soc., 78[11], 3167-68, 1995
- [163] Anne G., Neirinck B., Vanmeensel K., Van der Biest O.O., and Vleugels J., "Origin of the Potential Drop over the Deposit during Electrophoretic Deposition", J. Am. Ceram. Soc., 89[3], 823-28, 2006
- [164] Sarkar P., Huang X., and Nicholson P. S., "Electrophoretic Deposition and Its Use to Synthesize YSZ/Al<sub>2</sub>O<sub>3</sub> Microlaminates Ceramic/Ceramic Composites", Ceram. Eng. Sci. Proc., 14, 707-17, 1993
- [165] Sarkar P., Prakash O., Wang G., and Nicholson P. S., "Microlaminate Ceramic/Ceramic Composites (YSZ/Al<sub>2</sub>O<sub>3</sub>) by Electrophoretic Deposition", Ceram. Eng. Sci. Proc., 15, 1019, 1994
- [166] Sarkar P., Huang X., and Nicholson P. S., "Structural Ceramic Microlaminates by Electrophoretic Deposition", J. Am. Ceram. Soc., 75, 2907, 1992
- [167] Sussman A. and Ward T. J., "Electrophoretic Deposition of Coatings from Glass-Isopropanol Slurries", RCA Review, 42[2], 178-97, 1981
- [168] Hamaker H. C. and Verwey E. J. W., "The Role of the Forces between the Particles in Electrodeposition and Other Phenomena", Trans. Farad. Soc., 36, 180-85, 1940
- [169] Grillon F. Fayeulle D. and Jeandin M., "Quantitative Image-Analysis of Electrophoretic Coatings", J. Mater. Sci. Lett., 11, 272-75, 1992
- [170] Brown D. R. and Salt F. W., "The Mechanism of Electrophoretic Deposition under Steady Fields", Langmuir, 16, 9208-16, 2000
- [171] Fukada Y., Nagarajan N., Mekky W., and Bao Y., "Electrophoretic deposition Mechanisms, Myths and Materials", J. Mater. Sci., 39, 787-801, 2004
- [172] Sides, P. J., "Electrodynamically Particle Aggregation on An Electrode Driven by An Alternating Electric Field Normal to It", Langmuir, 17, 5791-800, 2001
- [173] Perez, A. T., Saville, D. and Soria, C., "Modeling the Electrophoretic Deposition of Colloidal Particles", Europhys. Lett., 55, 425-431, 2001
- [174] Greil, P., Cordelair, J., and Bezold, A., "Discrete Element Simulation of Ceramic Powder Pprocessing", Z. Metallk., 92, 682-689, 2001
- [175] Hoggard J. D., Sides P. J., and Prieve D. C., "Electrolyte-Dependent Pairwise Particle Motion near Electrodes at Frequencies below 1kHz", Langmuir, 23, 6983-90, 2007
- [176] Ristenpart W. D., Aksay I. A. and Saville D. A., "Electrohydrodynamic Flow around a Colloidal Particle near an Electrode with an Oscillating Potential", Journal of Fluid Mechanics, 575, 83-109, 2007

## References

---

- [177] Ristenpart, W. D., Aksay, I. A. and Saville, D. A., "Electrically Driven Flow near a Colloidal Particle Close to an Electrode with a Faradaic Current", *Langmuir*, 23, 4071-80, 2007
- [178] Giersig M. and Mulvaney P., "Formation of Ordered Two-Dimensional Gold Colloid Lattices by Electrophoretic Deposition", *J. Phys. Chem.*, 97, 6334-6, 1993
- [179] Giersig M. and Mulvaney P., "Preparation of Ordered Colloid Monolayers by Electrophoretic Deposition", *Langmuir*, 9, 3408-13, 1993
- [180] Trau M., Saville D. A., and Aksay I. A., "Assembly of Colloidal Crystals at Electrode Interfaces", *Langmuir*, 13, 6375-81, 1997
- [181] Bohmer M., "In Situ Observation of Two-Dimensional Clustering during Electrophoretic Deposition", *Langmuir*, 12, 5747-50, 1996
- [182] Solomentsev Y., Bohmer M., and Anderson J. L., "Particle Clustering and Pattern Formation during Electrophoretic Deposition: a Hydrodynamic Model", *Langmuir*, 13, 6058-68, 1997
- [183] Bailey R. C., Stevenson K. J, and Hupp J. T., "Assembly of Micropatterned Colloidal Gold Thin Film via Microtransfer Molding and Electrophoretic Deposition", *Adv. Mater.*, 12[24], 1930-4, 2002
- [184] Nicholson P. S., Sarkar P., Prakash O., and Wang G., "Mimicking Nature's Ceramic/Ceramic Laminar Composites by Electrophoretic Deposition", *Ceram. Trans.*, 46, 533-41, 1994
- [185] You Ch., Jiang D. L., and Tan S. H., "SiC/TiC Laminated Structure Shaped by Electrophoretic Deposition", *Ceram. Int.*, 30, 813-5, 2004
- [186] Sarkar P., Datta S., and Nicholson P. S., "Functionally Graded Ceramic/Ceramic and Metal/Ceramic Composites by Electrophoretic Deposition", *Composites Part B: Engineering*, 28B[1-2], 49-56, 1998
- [187] Sarkar P., Datta S., and Nicholson P. S., "Electrophoretic Forming of Functionally-Graded Materials", *Ceram. Trans.*, 76, 15-30, 1997
- [188] Zhao C., Vleugels J., Vandeperre L., Basu B., and Van der Biest O. O., "Y-TZP/Ce-TZP Functionally Graded Composite", *J. Mater. Sci. Lett.*, 17[17], 1453-5, 1998
- [189] Yamada N., Shoji H., Kubo Y., and Katayama S., "Preparation of Inorganic-Organic Hybrid Films Containing Particles Using Electrophoretic Deposition Method", *J. Mater. Sci.*, 37, 2071-6, 2002
- [190] Yamada N., Yoshinaga I., and Katayama S., "Synthesis and Dynamic Mechanical Behaviour of Inorganic-Organic Hybrids Containing Various Inorganic Components", *J. Mater. Chem.*, 7, 1491-6, 1997

## References

---

- [191] Boccaccini A. R., Kaya C., and Chawla K. K., "Use of Electrophoretic Deposition in the Processing of Fiber Reinforced Ceramic and Glass Matrix Composites: A Review", *Composites Part A: Appl. Sci. Eng.*, 32, 997-1006, 2001
- [192] Kaya C., Kaya F., Boccaccini A. R., and Chawla K. K., "Fabrication and Characterisation of Ni-Coated Carbon Fiber Reinforced Alumina Ceramic Matrix Composites Using Electrophoretic Deposition", *Acta Mater.*, 49, 1189-97, 2001
- [193] Mahajan S. V., Hasan S. A., Cho J., Shaffer M. S. P., Boccaccini A. R., and Dicherson J. H., "Carbon Nanotube-Nanocrystal Heterostructures Fabricated by Electrophoretic Deposition", *Nanotechnology*, 19[19], 2008
- [194] Li H. X., Lin M. Z., and Hou J.G., "Electrophoretic Deposition of Ligand-Stabilized Silver Nanoparticles Synthesized by the Process of Photochemical Reduction", *J. Cryst. Growth*, 212, 222-6, 2000
- [195] Sarkar P., De D., Yamashita K., Nicholson P. S., and Umegaki T., "Mimicking Nanometer Atomic Processes on A Micrometer Scale via Electrophoretic Deposition", *J. Am. Ceram. Soc.*, 83, 1399-401, 2000
- [196] Perez A. T., Saville D., and Soria C., "Modeling the Electrophoretic Deposition of Colloidal Particles", *Europhys. Lett.*, 55, 425-31, 2001
- [197] Hayashi K. and Furuya N., "Preparation of Gas Diffusion Electrodes by Electrophoretic Deposition", *J. Electrochem. Soc.*, 151[3], A354-7, 2004
- [198] Dougami N. and Takada T., "Modification of Metal Oxide Semiconductor Gas Sensor by Electrophoretic Deposition", *Sens. Actuators B*, 93, 316-20, 2003
- [199] Stambouli A. B. and Traversa E., "Solid oxide fuel cells (SOFCs): A Review of An Environmentally Clean and Efficient Source of Energy", *Renew Sustainable Energy Rev.*, 6, 433-55, 2002
- [200] Ishihara T., Sato K., Mizuhara Y., and Takita Y., "Preparation of Ytria Stabilized Zirconia Films for Solid Oxide Fuel Cells by Electrophoretic Deposition Method", *Chem. Lett.*, 943-6, 1992
- [201] Ishihara T., Shimose K., Shiomitsu T., and Takita Y., "Electrophoretic Deposition of  $Y_2O_3$ -Stabilized  $ZrO_2$  on the Porous  $La_{0.8}Sr_{0.2}MnO_3$  Cathode Substrate for SOFC", In: Dokiya M., Yamamoto O., Tagawa H., Singhal S. C., editor. *Proceedings of the Fourth International Symposium on Solid Oxide Fuel Cells (SOFC-IV)* p.334-43, 1995
- [202] Zhitomirsky I., and Petric A., "Electrophoretic Deposition of Ceramic Materials for Fuel Cell Applications", *J. Euro. Ceram. Soc.*, 20, 2055-61, 2002
- [203] Zhitomirsky I., and Petric A., "Electrophoretic Deposition of Electrolyte Materials for Solid Oxide Fuel Cell", *J. Mater. Sci.*, 39, 825-31, 2004

## References

- [204] Lee J. H., Hyun K. H., Paik U., Jung Y. G., Lee J. H., Lee K. S., and Lee H. S., "Effect of Hydroxyl Groups in PVB on the Microstructure of Electrophoretically Deposited Green Bodies for Thermal Barrier Coatings", *Colloids Surf. A: Physicochem. Eng. Aspects*, 13-14, 23-6, 2008
- [205] Kingery W. D., *Introduction to Ceramics (Second Edition)*, John Wiley & Sons, Inc. New York, 1976
- [206] Stech M., Reynder P., and Rodel J., "Constrained Film Sintering of Nanocrystalline  $\text{TiO}_2$ ", *J. Am. Ceram. Soc.*, 83[8], 1889-96, 2000
- [207] Lu G. Q., Sutterlin R. C. and Gupta T. K., "Effect of Mismatched Sintering Kinetics on Camber in A Low-Temperature Cofired Ceramic Package", *J. Am. Ceram. Soc.*, 76[8], 1907-14, 1993
- [208] Scherer G. W. and Garino T. J., "Viscous Sintering on a Rigid Substrate", *J. Am. Ceram. Soc.*, 68[4], 216-20, 1985
- [209] Scherer G. W., "Sintering with Rigid Inclusions", *J. Am. Ceram. Soc.*, 70[10], 719-25, 1987
- [210] Raj R., "Analysis of the Sintering Pressure", *J. Am. Ceram. Soc.*, 70[9], C210-C211, 1987
- [211] Cocks A. C. F., "Constitutive Modelling of Powder Compaction and Sintering", *Prog. Mater. Sci.*, 46, 201-229, 2001
- [212] Johnson D. L. and Cutler I. B., "Diffusion Sintering: I, Initial Stage Sintering Models and Their Application to Shrinkage of Powder Compacts", *J. Am. Ceram. Soc.*, 45[11], 541-45, 1963
- [213] Herring C., "Effect of Change of Scale on Sintering Phenomena", *J. Appl. Phys.*, 21[4], 301-03, 1950
- [214] Bannister M. J., "Shape Sensitivity of Initial Sintering Equations", *J. Am. Ceram. Soc.*, 51[10], 548-53, 1968
- [215] Johnson D. L., "A General Model for the Intermediate Stage of Sintering", *J. Am. Ceram. Soc.*, 53[10], 574-77, 1970
- [216] Coble R. L., "Sintering Crystalline Solids. I. Intermediate and Final State Diffusion Models", *J. Appl. Phys.*, 32[5], 787-92, 1961
- [217] Coble R. L., "Sintering Crystalline Solids. II. Experimental Test of Diffusion Models in Powder Compacts", 32[5], 793-99, 1961
- [218] Coble R. L., and Gupta T. K., in "Sintering and Related Phenomena", (Kuczynski G. C., Hooton N. A., and Gibbon C. F., eds.), p 423. Gordon & Breach, New York, 1967



## References

- [219] Kuczynski G. C., "Self-Diffusion in Sintering of Metallic Particles", Transactions of the American Institute of Mining and Metallurgical Engineers, 185[2], 169-78, 1949
- [220] Kuczynski G. C., "Mechanism of Densification during Sintering of Metallic Particles," Acta Metall., 4[1], 58-61, 1956
- [221] Johnson D. L., in "Ultrafine-Grain Ceramics" (J. J. Burke, N. L. Reed, and V. Weiss, eds.), p. 173, Syracuse Univ. Press, Syracuse, New York, 1970
- [222] Kellett B. J. and Lange F. F., "Thermodynamics of Densification: I, Sintering of Simple Particles Arrays, Equilibrium Configurations, Pore Stability, and Shrinkage", J. Am. Ceram. Soc., 72[5], 725-34, 1989
- [223] Johnson D. L., "New Method of Obtaining Volume, Grain-Boundary, and Surface Diffusion Coefficients from Sintering Data", J. Appl. Phys., 40[1], 192-200, 1969
- [224] Coble R. L., A Model for Boundary Diffusion Controlled Creep in Polycrystalline Materials", J. Appl. Phys., 34[6], 1679-82, 1963
- [225] Rhodes W. H., "Agglomerate and Particle Size Effects on Sintering Yttria-Stabilized-Zirconia". J. Am. Ceram. Soc., 64[1], 19-22, 1981
- [226] Liu D.M., Influence of Pore Structure in Green Compacts on Densification of SiC- $\text{Al}_2\text{O}_3$ - $\text{Y}_2\text{O}_3$ ", Ceram. Int., 22, 403-06, 1996
- [227] Furnas C. C., "Relations between Specific Volume, Voids, and Size Composition in Systems of Broken Solids of Mixed Sizes", U. S. Bur. Mines Rep. Invest., No. 2894, 1928
- [228] Furnas C. C., "Grading Aggregates, I. Mathematical Relations for Bed of Broken Solids of Maximum Density", Ind. Eng. Chem, 23[9], 1052-58, 1931
- [229] O'Hara M. J. and Cutler I. B., "Sintering Kinetics of Binary Mixtures of Alumina Powders", Proc. Brit. Ceram. Soc., 12, 145-54, 1969
- [230] Kuczynski G. C., "Measurement of Self-Diffusion in Silver without Radioactive Tracers", J. Appl. Phys., 21[7], 632-37, 1950
- [231] Coble R. L., "Effects of Particle Size Distribution on Initial-Stage Sintering", J. Am. Ceram. Soc., 56[9], 461-66, 1973
- [232] Evans A. G., "Considerations of Inhomogeneity Effects in Sintering", J. Am. Ceram. Soc., 65[10], 497-501, 1982
- [233] Venkatachari K. R. and Raj R., "Shear Deformation and Densification of Powder Compacts", J. Am. Ceram. Soc., 69[6], 499-506, 1986
- [234] Rahaman M. N. and De Jongher L. C., Creep-Sintering of Zinc Oxide", J. Mater.Sci., 22, 4326-30, 1987

## References

---

- [235] Rahaman M. N., De Jonghe L. C., and Brook R. J., "Effect of Shear Stress on Sintering", *J. Am. Ceram. Soc.*, 69[1], 53-58, 1986
- [236] Rahaman M. N., De Jonghe L. C., and Chu M. Y., "Effect of Green Density on Densification and Creep during Sintering", *J. Am. Ceram. Soc.*, 74[3], 514-19, 1991
- [237] Calata J. N., Matthys A., and Lu G. Q., "Constrained-Film Sintering of Cordierite Glass-Ceramic on Silicon Substrate", *J. Mater. Res.*, 13[8], 2234-341, 1998
- [238] Choe J. W., Calata J. N., and Lu G. Q., "Constrained-Film Sintering of a Gold Circuit Paste", *J. Mater. Res.*, 10[4], 986-94, 1995
- [239] Guillon O., Kraub S. and Rodel J., "Influence of Thickness on the Constrained Sintering of Alumina Films", *J. Euro. Ceram. Soc.*, 27, 2623-27, 2007
- [240] Bordia R. K., Zuo R., Guillon O., Salamone S. M., and Rodel J., "Anisotropic Constitutive Laws for Sintering Bodies", *Acta Mater.*, 54, 111-8, 2006
- [241] Raj R. and Bordia R. K., "Sintering Behavior of Bi-modal Powder Compacts", *Acta Metall.*, 32[7], 1003-19, 1984
- [242] Anne G., Vanmeensel K., Vleugels J. and Van der Biest O. O., "A Mathematical Description of the Kinetics of the Electrophoretic Deposition Process for  $\text{Al}_2\text{O}_3$ -Based Suspensions", *J. Am. Ceram. Soc.*, 88[8], 2036-39, 2005
- [243] De D. and Nicholson P. S., "Role of Ionic Depletion in Deposition during Electrophoretic Deposition", *J. Am. Ceram. Soc.*, 82[11], 3031-36, 1999
- [244] Zhang J. and Lee B. I., "Electrophoretic Deposition and Characterization of Micrometer-scale  $\text{BaTiO}_3$  Based X7R Dielectric Thick Films", *J. Am. Ceram. Soc.*, 83[10], 2417-22, 2000
- [245] Ishihara T., Shimose K., Kudo T., Nishiguchi H., Akbay T., and Takita Y., "Preparation of Yttria-Stabilized Zirconia Thin Films on Strontium-Doped  $\text{LaMnO}_3$  Cathode Substrates via Electrophoretic Deposition for Solid Oxide Fuel Cells", *J. Am. Ceram. Soc.*, 83[8], 1921-27, 2000
- [246] Chen F. L. and Liu M. L., "Preparation of Yttria-Stabilized Zirconia (YSZ) Films on  $\text{La}_{0.85}\text{Sr}_{0.15}\text{MnO}_3$  (LSM) and LSM-YSZ Substrates Using an Electrophoretic Deposition (EPD) Process", *J. Euro. Ceram. Soc.*, 21, 127-34, 2001
- [247] Yuan Y., Wang X. and Xiao P., "Attrition Milling of Metallic-Ceramic Particles in Acetyl-acetone", *J. Euro. Ceram. Soc.*, 24, 2233-40, 2004
- [248] Alvarez R. H., "On the Conversion of Experimental Electrokinetic Data into Double Layer Characteristics in Solid-Liquid Interfaces", *Ad. Colloid and Interface Sci.*, 34, 217-341, 1991

## References

---

- [249] Chen C. Y., Chen S. Y. and Liu D. M., "Electrophoretic Deposition Forming of Porous Alumina Membranes", *Acta Mater.*, 47[9], 2717-26, 1999
- [250] Besendorfer G. and Roosen A., "Particle Shape and Size Effects on Anisotropic Shrinkage in Tape-Cast Ceramic Layers", *J. Am. Ceram. Soc.*, 91[8], 2514-20, 2008
- [251] Suslick, K. S., ed. *Ultrasound: Its Chemical, Physical and Biological Effects*. VCH: Weinheim, 1988
- [252] Kuang X., Carotenuto G. and Nicolais L., "A Review of Ceramic Sintering and Suggestions on Reducing Sintering Temperatures", *Advanced Performance Materials*, 4, 257-74, 1997
- [253] Koura N., Tsukamoto T., Shoji H., and Hotta T., "Preparation of Various of Oxide Films by an Electrophoretic Deposition Method: A Study of the Mechanism", *Jpn. J. Appl. Phys.*, 34, 1643-47, 1995
- [254] Cheng T. and Raj R., "Flaw Generation During Constrained Sintering of Metal-Ceramic and Metal-Glass Multilayer Films", *J. Am. Ceram. Soc.*, 72[9], 1645-55, 1989
- [255] Kunz S. C. and Loehman R. E., "Thermal Expansion Mismatch Produced by Interfacial Reactions in Glass-Ceramic to Metal Seals", *Adv. Ceram. Mater.* 2[1], 69-73, 1987
- [256] Cheng T. and Raj R., "Measurement of the Sintering Pressure in Ceramic Films", *J. Am. Ceram. Soc.*, 71[4], 276-80, 1988
- [257] Wang X. and Xiao P., "Residual Stresses and Constrained Sintering of YSZ/ $\text{Al}_2\text{O}_3$  Composite Coatings", *Acta Materialia*, 52, 2591-603, 2004
- [258] Guillon O., Aulbach E. and Rodel J., "Constrained Sintering of Alumina Thin Films: Comparison Between Experiment and Modeling", *J. Am. Ceram. Soc.*, 90[6], 1733-37, 2007
- [259] Lu X. J. and Xiao P., "Constrained Sintering of YSZ/ $\text{Al}_2\text{O}_3$  Composite Coatings on Metal Substrates Produced from Electrophoretic Deposition", *J. Euro. Ceram. Soc.*, 27, 2617-21, 2007
- [260] Mukhopadhyay N. K. and Paufler P., "Micro- and Nanoindentation Techniques for Mechanical Characterisation of Materials", *International Materials Reviews*, 51[4], 209-45, 2006
- [261] Coble R. L. "Initial Sintering of Alumina and Hematite", *J. Am. Ceram. Soc.*, 41[2], 55-62, 1958
- [262] Seltzer M. S., Talty P. K., "High-Temperature Creep of  $\text{Y}_2\text{O}_3$ -Stabilized  $\text{ZrO}_2$ ", *J. Am. Ceram. Soc.*, 58[3-4], 124-30, 1975

## References

---

- [263] Matsui K., Yamakawa T., and Uehara M., "Mechanism of Alumina-Enhanced Sintering of Fine Zirconia Powder: Influence of Alumina Concentration on the Initial Stage Sintering", J. Am. Ceram. Soc., 91[6], 1888-97, 2008
- [264] Wang J. and Raj R., "Estimate of the Activation Energies for Boundary Diffusion from Rate-Controlled Sintering of Pure Alumina, and Alumina Doped with Zirconia or Titania", J. Am. Ceram. Soc., 73[5] 1172-5, 1990
- [265] Young W. S. and Cutler I. B., "Initial Sintering with Constant Rates of Heating", J. Am. Ceram. Soc., 53[12], 659-63, 1970

